eXPRESS Polymer Letters Vol.9, No.12 (2015) 1052
Available online at www.expresspolymlett.com
DOI: 10.3144/expresspolymlett.2015.94

Editorial corner – a personal view

How green are green polymer composites? (Any chance to define the level of 'greenness'?)

Z. A. Mohd Ishak[*]

Polymer Engineering Division, School of Materials and Mineral Resources Engineering, Universiti Sains Malaysia, Engineering Campus, 14300 Nibong Tebal, Pulau Pinang, Malaysia
Cluster for Polymer Composites, Science and Engineering Research Centre, Universiti Sains Malaysia, Engineering Campus, 14300 Nibong Tebal, Pulau Pinang, Malaysia

Growing environmental awareness of mankind is becoming a key factor which influences the selection of goods and products of their consumers. Obviously, this has a strong influence on the whole value chain of manufacturing from feedstock to waste disposal.

Based on marketing strategies environmental friendly products are labelled by green, eco, renewable, sustainable, pollution-free, carbon-neutral, ecologically friendly, clean attributes, and the like. Different definitions are introduced also for green polymer composites. Composites containing only reinforcements from renewable resources (e.g. natural fibres) are referred to as green as those comprising both bio-based resins and fibres. Is there any possibility to define, or to estimate the level of 'greenness'? The most promising way to answer this question is to adapt the life cycle analysis (LCA), commonly termed as to 'cradle-to-grave' analysis. LCA is foreseen to evaluate every eventual impact caused by the manufacturing, processing, use and disposal of a given product. In the meantime, LCA is well established to evaluate composite parts, especially when traditional materials are replaced by polymer composite ones. Results of the analysis, however, may vary whether the outcome is optimized for different targets, such as global warming potential, solid waste amount management, etc.

Interestingly, LCA studies are seldom performed on natural fibre reinforced composites. Accordingly, limited information is available on how plant cultivation, transformation of the plant to fibres (transportation, retting, fibrillization, follow-up treatment…) affect the greenness of the related product. This is, however, a critical issue due to the expected growth of green polymer composites in the automotive sector. The end-of-life directives on vehicles, introduced in the European Union and Japan, force the involved parties to make their homework. In this respect, LCA should cover effects of biobased polymer matrices, as well. LCAs sometimes are performed from cradle-to-gate , i.e. to the gate of the composite part manufacturing site. Nonetheless, even such shortened analyses would help to pinpoint how the corresponding polymer composites can be made 'greener'. And what is about to extend it for a cradle-to-cradle process when possible? Is it not a challenging task worth of working on?

Prof. Dr. Zainal Arifin Mohd Ishak
Member of International Advisory Board

[*]Corresponding author, e-mail: zarifin.ishak@googlemail.com

eXPRESS Polymer Letters Vol.9, No.12 (2015) 1053–1067
Available online at www.expresspolymlett.com
DOI: 10.3144/expresspolymlett.2015.95

Hydroquinone based sulfonated poly (arylene ether sulfone) copolymer as proton exchange membrane for fuel cell applications

*V. Kiran, S. Awasthi, B. Gaur**

Department of Chemistry, National Institute of Technology Hamirpur, 177005 Hamirpur, India

Received 16 April 2015; accepted in revised form 8 July 2015

Abstract. Synthesis of sulfonated poly (arylene ether sulfone) copolymer by direct copolymerization of 4,4′-bis(4-hydroxyphenyl)valeric acid, benzene 1,4-diol and synthesized sulfonated 4,4′-difluorodiphenylsulfone and its characterization by using FTIR (Fourier Transform Infrared) and NMR (Nuclear Magnetic Resonance) spectroscopic techniques have been performed. The copolymer was subsequently cross-linked with 4, 4′(hexafluoroisopropylidene)diphenol epoxy resin by thermal curing reaction to synthesize crosslinked membranes. The evaluation of properties showed reduction in water and methanol uptake, ion exchange capacity, proton conductivity with simultaneous enhancement in oxidative stability of the crosslinked membranes as compared to pristine membrane. The performance of the membranes has also been evaluated in terms of thermal stability, morphology, mechanical strength and methanol permeability by using Thermo gravimetric analyzer, Differential scanning calorimetery, Atomic force microscopy, XPERT-PRO diffractometer, universal testing machine and diffusion cell, respectively. The results demonstrated that the crosslinked membranes exhibited high thermal stability with phase separation, restrained crystallinity, acceptable mechanical properties and methanol permeability. Therefore, these can serve as promising proton exchange membranes for fuel cell applications.

Keywords: *polymer membranes, copolymer, crosslinking, proton exchange membrane*

1. Introduction

There is an ever-growing demand for the alternative energy resources that can generate energy and could be environmental friendly. The petrol crisis and the emission problems resulting from it have impelled the mankind to develop new energy conversion technologies. Fuel cells achieved an important place in the application of alternative energy due to low greenhouse gas emission and high energy conversion efficiency. In the past decade, the polymer electrolyte membrane fuel cells (PEMFCs) have attracted considerable attention as one of the most promising clean energy sources for transportation, stationary and portable power applications. The proton exchange membranes (PEMs) are the cardinal components of PEMFCs, as these membranes play dual duty of transferring protons from anode to cathode as well as act as barrier to the fuel gas cross leaks between two electrodes. The perfluorinated membrane such as Nafion is the well-known commercially used PEM due to high proton conductivity. But some specific limitations associated with these perfluorinated ionomers including high cost, high fuel cross over and loss of preferable properties at elevated temperature (>80°C) demand a search for alternative PEMs [1–5]. In the recent years a varied class of aromatic hydrocarbon polymers have been synthesized and evaluated as backbone, in terms of their applicability as proton exchange membranes. These include poly(arylene ether ketone)s, poly(arylene

*Corresponding author, e-mail: bhartigaur@gmail.com

ether sulfone)s [6–12], poly(arylene ether nitrile)s [13, 14], polyimides [15, 16], poly(phthalalazinone ether)s [17]. Extensive work has also been carried out by the researchers on polybenzimidazole based membranes which represents the class of PEMs having acid-base interactions and are suitable for high temperature operating fuel cell applications. Therefore, these membranes can enhance the CO tolerance of the catalyst. Polybenzimidazole (PBI) based PEMs have been extensively studied, in the form of their complexes with phosphoric acid [18, 19]. But the leaching out of the phosphoric acid from the membranes is one of the major problems of phosphoric acid doped PBI membranes which consequently reduce their proton conductivity. Several modified PBI based membranes are reported in the literature. Pyridine based PBI membranes with improved proton conductivity and oxidative stability; membranes of PBI segmented block copolymers and random block copolymers of PBI by using tetra-amine and dicarboxylic acid combinations have also been synthesized and examined as their applicability in PEMFCs [20–22].

However, among the promising candidates, sulfonated poly (arylene ether sulfone)s (SPAES)s are well-known engineering thermoplastics and these are reasonably good choice for high temperature operating PEMFCs. Apart from possessing adequate mechanical properties with high thermal and chemical resistance these are also more economical as compared to Nafion.

The hydroquinone based copolymers can provide many advantages over the biphenyl systems such as low cost, high IEC and better nanophase separation between hydrophillic and hydrophobic domains [17, 23, 24]. To the best of our knowledge the sulfonated poly arylene ether sulfone (SPAES) membranes using hydroquinone along with 4,4′-bis (4-hydroxyphenyl)valeric acid (DPA) as co-monomers have not yet been reported.

In the present work we have endeavoured to synthesize the SPAES crosslinked membranes based on benzene 1,4-diol (HQ) and DPA as PEMs for fuel cell applications. With the purpose to enhance proton conductivity of the membranes, a monomer DPA containing carboxylic acid group on the flexible aliphatic side chain of aromatic backbone has been taken. It is assumed that it can provide protons and help in nanophase separation of hydrophilic and hydrophobic domains. Further keeping in view mechanical integrity, the crosslinking of the synthesized (sulfonated poly arylene ether sulfone) copolymer (SPAES-H-0) with the synthesized 4,4′(hexafluoroisopropylidene)diphenol epoxy resin (EFN) has been done, where carboxylic acid groups of DPA react with oxirane rings of EFN and form crosslinked membranes. The crosslinked membranes have been characterized to evaluate their properties such as ion exchange capacity, water/methanol uptake, proton conductivity, oxidative stability, morphology, mechanical strength and thermal stability as PEMs for fuel cell applications.

2. Experimental

2.1. Materials and synthesis

2.1.1. Materials

4,4′-(hexafluoroisopropylidene)diphenol (6F-bisphenol-A/6F-BPA, 97% Sigma Aldrich Chemie Gmbh, Germany), formaldehyde (37–41%, Merck Specialities Private Limited, Mumbai India), Isopropanol (99.0%, Merck Specialities Private Limited, Mumbai India), para-toluene sulfonic acid (PTSA, 98%, Merck Specialities Pvt. Limited, Mumbai India), Methyl isobutyl ketone (MIBK, 99.5%, Merck Specialities Pvt. Limited, Mumbai India), epichlorohydrin (ECH, 98.0%, Loba Chemie Pvt. Ltd. Mumbai India), and sodium hydroxide (98%, Loba Chemie Pvt. Ltd. Mumbai, India) were used for the synthesis of novolac based epoxy resin (EFN). 4,4′- bis(4-hydroxyphenyl) valeric acid (DPA, 97%, Alfa Aesar chemicals, Johnson Mathey Company, Heysham, England), benzene 1,4-diol (hydroquinone/HQ, 99% Sigma Aldrich Chemie Gmbh, Germany), 4,4′-difluorodiphenylsulfone (DFDPS, 99%, Sigma Aldrich Chemie Gmbh, Germany), dimethyl sulfoxide (DMSO, 99.9%, Sigma Aldrich Chemie Gmbh, Germany), potassium carbonate (K_2CO_3, 99.9%, Loba Chemie, Pvt. Ltd. Mumbai, India), toluene (99%, Thermo Fisher Scientific India Pvt. Ltd. Mumbai, India) and hydrochloric acid (35–38%, Thermo Fisher Scientific India Pvt. Ltd. Mumbai, India) were used for synthesizing sulfonated poly arylene ether sulfone copolymer. Fuming sulfuric acid (20%, Alfa Aesar chemicals, Johnson Mathey Company, Heysham, England) was used for the sulfonation of DFDPS.

2.1.2. Synthesis of 4,4′-(hexafluoroisopropylidene) diphenol (6F-BPA) based novolac epoxy resin (EFN)

A 40 mL methyl isobutyl ketone (MIBK) solution containing 6F-BPA (0.05 mol) and PTSA (0.0014 mol) was added to a 250 mL three-necked round bottom flask equipped with a mechanical stirrer and dean and stark trap with a reflux condenser. Nitrogen gas was purged for 30 minutes and the reaction solution was heated to 100°C with stirring. 0.08 moles of formaldehyde solution (37–41%) was added to the reaction mixture drop wise. Then, the reaction mixture was heated to 120°C with constant stirring and maintained at this temperature for five hours. The condensation of novolac resin is a reversible process; therefore (0.13 mol) of water generated during the reaction was removed as an azeotropic mixture with MIBK. The reaction mixture was cooled to room temperature and washed with deionised water several times until it became neutral. The solution was then distilled at 120°C in order to remove the MIBK solvent. The product was washed with a mixture of water/methanol (7/3 v/v) several times to remove the unreacted 6F-BPA. A red brown solid product was obtained after vacuum drying at 60°C for 48 h.

To the above dried product of 6F-BPA novolac, 8 moles of epichlorohydrin for every phenolic group of novolac resin, isopropyl alcohol (0.83 mol) was added to 250 mL three necked round bottom flask equipped with a mechanical stirrer and a condenser. After increasing the reaction temperature to 70°C with constant stirring, 0.078 mol of 20 wt% aqueous solution of sodium hydroxide was added drop wise into the reaction solution within one hour. The system was maintained at 70°C for another four hours with constant stirring. The reaction product in the flask was washed several times with deionized water to remove sodium chloride. The product was dissolved in toluene and filtered in order to remove the residual salt. Toluene and excess of ECH were distilled off under reduced pressure. Finally the product obtained was dried at 60–70°C under vacuum for 48 hours (Figure 1).

2.1.3. Synthesis of sulfonated 4,4′-difluorodiphenylsulfone (SDFDPS)

The DFDPS (0.01 mol) and 15 mL of 20% fuming sulfuric (15 mL) acid were added to a 100 mL three-necked round bottom flask equipped with overhead mechanical stirrer and a condenser. The mixture was heated to 110°C with constant stirring for six hours. After cooling the reaction mixture was poured into 200 mL ice water stirred with magnetic stirrer, and neutralized with 2M NaOH solution to a final pH 8. To this solution excess of NaCl was added and allowed to stand overnight. Finally the precipitates (ppts) were filtered and recyrstallized from a mixture of methanol and water (9/1 v/v) (Figure 2).

2.1.4. Synthesis of sulfonated poly (arylene ether sulfone) (SPAES) copolymer

Sulfonated poly (arylene ether sulfone) copolymer (SPAES-H) was synthesized in a 250 mL three necked round bottom flask equipped with a mechanical stirrer and dean and stark trap. DPA (0.012 mol,), HQ (0.012 mol) and 35 mL of DMSO were charged into the reaction flask. To this reaction mixture potas-

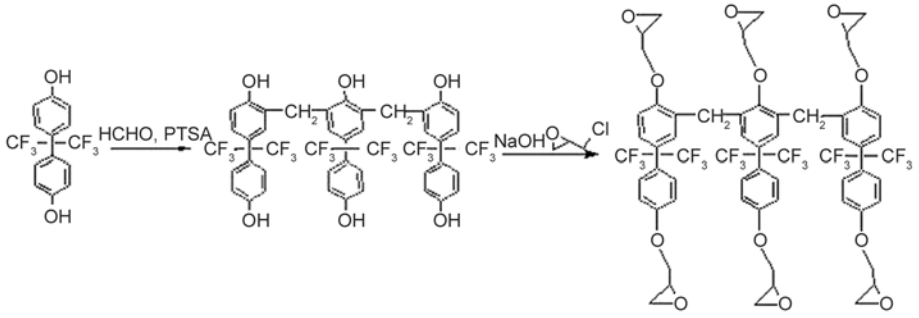

Figure 1. Synthesis of EFN epoxy resin

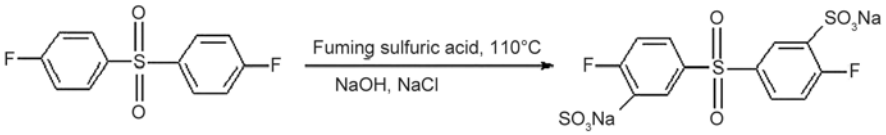

Figure 2. Synthesis of SDFDPS

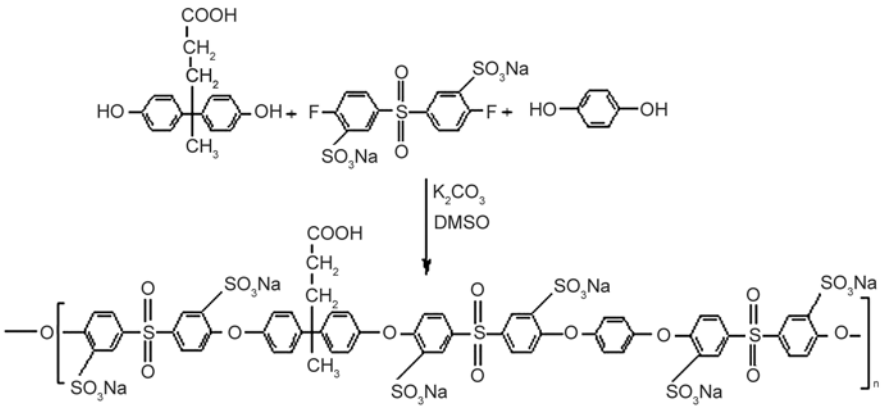

Figure 3. Synthesis of SPAES-H-0 copolymer

sium carbonate (0.06 mol) was added and stirred at 80°C for 8 hours for producing reactive phenolate ions. Then SDFDPS (0.025 mol), 17 mL of toluene and 15 mL of DMSO were then added and the temperature was increased to 150°C the reaction mixture was stirred for 4 hours in order to dehydrate the system. After this, the temperature was increased to 180°C with constant stirring; reaction was carried out at this temperature for another 26 hours until the reaction mixture became very viscous. After cooling, the solution was dissolved in DMSO and then filtered. Precipitation of the copolymer was carried out by adding isopropyl alcohol to the filtrate. The precipitates were filtered and dried at 70°C (Figure 3).

2.1.5. Preparation of membrane and its cross-linking

The crosslinking of the SPAES-H-0 copolymer was done by dissolving 1 g in 10 mL DMSO at 30°C in a 50 mL round bottom flask and further adding EFN resin to this. The weight ratio of EFN to SPAES-H-0 copolymer was varied in the range 50–70%. The crosslinking reaction between SPAES-H-0and EFN was carried out at 70–80°C for 24 hours with constant stirring. The solution was then filtered and cast onto the glass plates and dried at 70-80°C for 24 hours; the temperature was then subsequently raised to 150°C for another 5 hours. The membranes thus obtained were dipped in 1M HCl solution for 48 hours at room temperature for their proton exchange (Figure 4).

2.2. Characterization

2.2.1. Structural characterization

FTIR spectra of the samples were recorded by using Perkin Elmer 1600 FTIR spectrophotometer in the range of 4000–400 cm^{-1} on the KBR pellets. ^{1}H NMR and ^{13}C NMR spectra were recorded on a BRUKER AVANCE II 400 NMR spectrometer using deuterated dimethyl sulfoxide as solvent, and tetramethyl silane as the internal standard.

2.2.2. Ion exchange capacity (IEC)

IEC was determined by titration method, which was used quantitatively to determine sulfonic acid concentration in the membranes. 0.2 g of the membrane samples in acid form were immersed in 50 mL of 1M NaCl solution at room temperature for 48 hours to allow the exchange process between H^{+} ions with

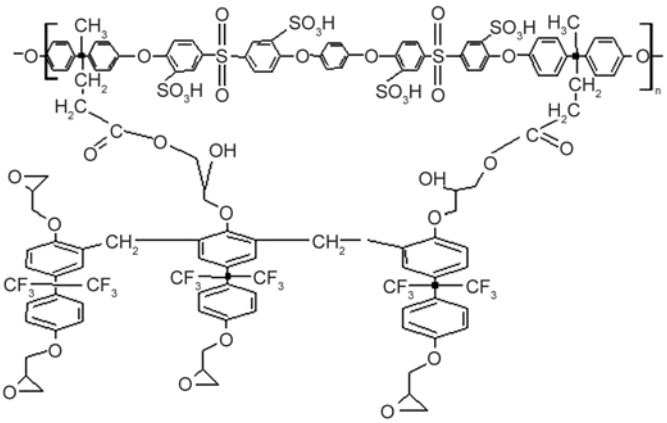

Figure 4. Crosslinking of SPAES-H-0 copolymer with EFN epoxy resin

Na^+ ions. The liberated H^+ ions were titrated against 0.01M NaOH solution using phenolphthalein as an indicator [25, 26]. The IEC was calculated by using Equation (1):

$$\text{IEC}=\frac{\text{Consumed NaOH[mL]}\cdot\text{molarity NaOH}}{\text{Weight of dry membrane}}\left[\frac{\text{meq}}{\text{g}}\right] \quad (1)$$

2.2.3. Swelling property

The water and methanol absorption of the membranes were determined by measuring the change in the weight of dry and swollen membranes. After measuring the weights and lengths of the dry membranes, the sample membranes were immersed in water and methanol for 24 h. The excess water and methanol from the sample films were removed by wiping with filter paper. The percentage of water and methanol absorption was calculated by using Equation (2):

$$\text{Water/Methanol uptake [\%]} = \frac{W_w - W_d}{W_d}\cdot 100 \quad (2)$$

where W_w and W_d were the weights of the wet and corresponding dry membranes, respectively.

Swelling ratio of the membranes in water was determined by using the Equation (3):

$$\text{Swelling ratio [\%]} = \frac{L_w - L_d}{L_d}\cdot 100 \quad (3)$$

where L_w and L_d were the lengths of the wet and corresponding dry membranes, respectively [27–29].

2.2.4. Gel fraction [%]

The gel fraction of the crosslinked membranes was determined according to ASTM D2765 method using Soxhlet extractor. The membrane samples were refluxed in DMAc for at least 48 h, until the sample attained a constant weight [17]. The gel fraction of the crosslinked membranes were calculated by using Equation (4):

$$\text{Gel fraction [\%]} = \frac{W_2}{W_1}\cdot 100 \quad (4)$$

where W_2 was the weight of the dried membranes after extraction and W_1 was the weight of the membranes before extraction, respectively.

2.2.5. Proton conductivity

The conductivity of the membranes was checked at room temperature by four point probe technique. The four point probe arrangement was attached with Keithley 6221 sourcemeter and Keithley 2182A nanovoltmeter. The membranes were cut into 2×2 cm^2 and immersed in deionised water for 12 h before the measurement. The excess water from the membrane surface was wiped off with the help of filter paper. These membranes were further mounted onto the cell and an alternating current (I) ranging from 0.1–1.0 mA was applied to the cell, while the corresponding voltage (V) was obtained from the nanovoltmeter [30]. The resistance (V/I) was determined from the slope of the linear plot of V vs I, based on the Equations (5) and (6):

$$\text{Resistivity } (\rho) = \frac{V}{I}\cdot \text{thickness of the membrane}\cdot\frac{\pi}{\ln 2} \quad (5)$$

$$\text{Conductivity } (\sigma) = \frac{1}{\rho}\left[\frac{\text{S}}{\text{cm}^2}\right] \quad (6)$$

2.2.6. Methanol permeability

Methanol permeability was determined by using diffusion cell consisting of two compartments A and B which were partitioned by a membrane sample. 1M solution of methanol was placed in compartment A and water was placed in compartment B of the diffusion cell. The membrane sample was clamped in the middle of the two compartments. The solution in each compartment was continuously stirred with the help of magnetic beads to maintain uniform concentration. The concentration of the methanol in compartment B was measured using T80 UV-VIS spectrometer. The methanol concentration in compartment B as a function of time (t) is given by the Equation (7):

$$C_{B(t)} = \frac{A(D_K)C_A(t - t_0)}{V_B L} \quad (7)$$

where C_A is the concentration of the methanol in compartment A, V_B [cm^3] is the volume of compartment B, A [cm^2] and L [cm] are the area and thickness of the membranes. t and t_0 are the initial and final diffusion time, D_K is the methanol permeability of the membrane, respectively [26, 31].

2.2.7. Oxidative stability

Square pieces (0.2 g) of membrane samples were immersed in Fenton's reagent (4 ppm $FeSO_4$ in 6% H_2O_2) at 30°C. The oxidative stability was evaluated by recording the retained weights of the membranes after treatment in Fenton's reagent and observing the expended time when membranes started to break and the time when the membranes disappeared completely [9, 31].

2.2.8. Atomic force microscopy

The surface morphology of the membranes was observed with an AFM system (Agilent 5500 SPM) at room temperature and room humidity. It was operated in tapping mode using nanosensor silicon probe with spring constant of 10–130 N/m and a resonance frequency of 204–497 kHz. The membranes were soaked in distilled water for 12 hours and average three tests were taken for each sample.

2.2.9. X-ray diffraction study

The XRD diffraction patterns of the membranes before and after crosslinking were obtained with a rotating anode XPERT-PRO diffractometer using Cu-Kα radiation source with a wavelength of 1.54060 Å.

2.2.10. Mechanical properties

The mechanical properties of the membranes were measured by using Hounsfield Universal Testing Machine at the deformation rate of 2 mm·min^{-1}. The films were cut into a size of 5×50 mm as reported by [17, 32]. Thicknesses of the membranes were 0.3 mm and for each testing at least three measurements were made and the average value was considered.

2.2.11. Thermal properties

Thermal degradation of the membranes was examined with EXSTAR TG/DTA 6300 thermal gravimetric analyzer under nitrogen atmosphere (200 mL·min^{-1}) at heating rate of 10°C·min^{-1} with sample size of 10±1 mg from 25 to 900°C. The glass transition temperature of the prepared membranes was measured on Mettler Differential Scanning Calorimetery equipment. The samples were preheated under 200 mL·min^{-1} nitrogen from room temperature to 150°C at a scanning rate of 10°C/min to remove moisture then cooled to 50°C and reheated from 50 to 350°C at a heating rate of 10°C/min.

3. Results and discussion

3.1. EFN resin

Figure 5a shows the FTIR spectrum of EFN novolac epoxy resin, characteristic absorptions at 3057 and 2929 cm^{-1} were due to stretching vibrations of aromatic rings and bridging methylene groups, respectively. A characteristic absorption band at 1299 cm^{-1} depicted the ring breathing frequency of epoxy ring, the appearance of the band at 916 cm^{-1} proved the asymmetric ring deformation and the band at 762 cm^{-1} showed the symmetric ring deformation of epoxy ring. The peaks in between 932–999 cm^{-1} were due to the presence of C–F bonds.

Figure 5b shows the ^{1}H NMR spectrum of novolac epoxy resin EFN. The spectrum showed proton resonance signals at 3.6–3.8 and 6.7–7.3 ppm due to –CH_2 bridging and aromatic protons respectively. Characteristic proton resonance signals at 2.7–2.9, 3.3 and 3.9–4.2 ppm due to –O–CH_2, –CH and –CH_2 protons of the epoxy ring, respectively, were also observed.

3.2. SDFDPS

Figure 6 represents ^{1}H NMR spectrum of the SDFDPS in which the proton (H_1) adjacent to the sodium sulfonate group gets deshielded and appear at 8.3 ppm due to electron withdrawing nature of sulfone group and H_2 and H_3 protons appeared at 7.7 and 7.3 ppm, respectively.

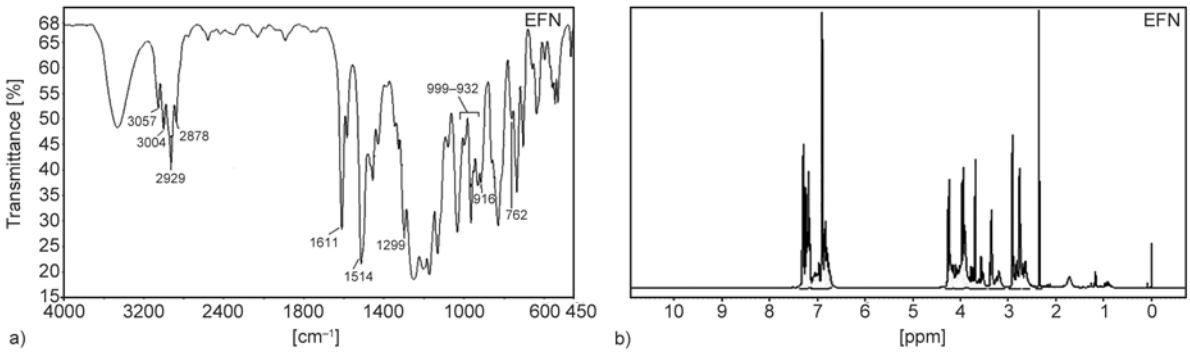

Figure 5. (a) FTIR and (b) ^{1}H NMR of EFN epoxy resin

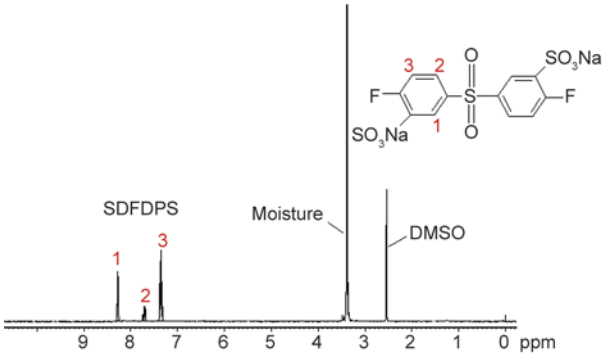

Figure 6. [1]H NMR spectrum of SDFDPS

3.3. SPAES-H-0 copolymer

Figure 7 showed the FTIR spectra of SPAES-H-0 and its crosslinked membranes. A characteristic absorption band at 1254 cm^{-1} suggested the C–O stretching vibrations of carboxylic acid group. Appearance of a doublet at 1330 and 1300 cm^{-1}, band at 1178 cm^{-1} were due to O=S=O asymmetric, symmetric and peak at 621 cm^{-1} was due to S–O stretching vibrations of pendant sodium sulfonate groups, respectively. A characteristic absorption band at 1040 cm^{-1} was due to C–O symmetric stretching vibrations of ether linkages.

In cross linked cr-SPAES-H-50, cr-SPAES-H-60 and cr-SPAES-H-70 membranes a characteristic new absorption band was observed at 1774 cm^{-1} due to C=O stretching vibrations of ester linkages formed after crosslinking of the SPAES-H-0 copolymer with EFN epoxy resin. The appearance of peaks at 948–969 cm^{-1} indicated the stretching vibrations of C–F bonds due to the presence of CF_3 groups in the EFN resin.

Figure 8a represents the [1]H NMR spectrum of the SPAES-H-0 copolymer. The protons (H_1, H_2 and H_3) present at ortho positions to the electron withdrawing groups (sulfone and sodium sulfonate) get deshielded and show signals at 8.2, 7.9 and 7.8 ppm, respectively. The aromatic protons (H_4) of the hydroquinone aromatic ring appeared at 7.4 ppm. The

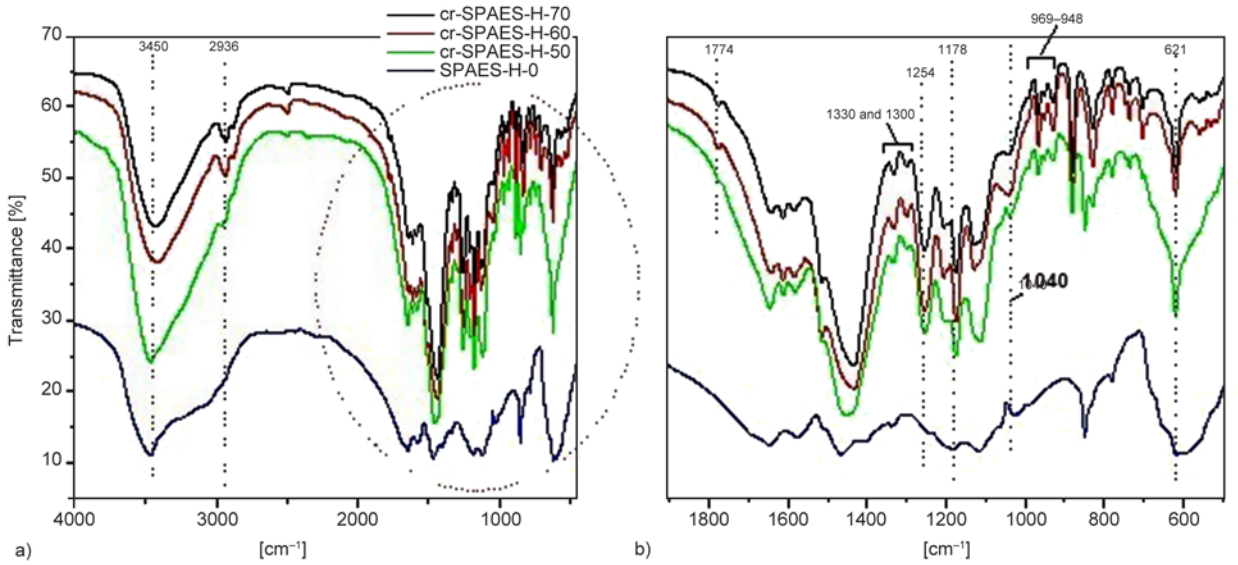

Figure 7. FTIR spectra of the SPAES-H-0 and its cr-SPAES-H membranes in the region (a) 4000–450 cm^{-1} and (b) 1900–450 cm^{-1}

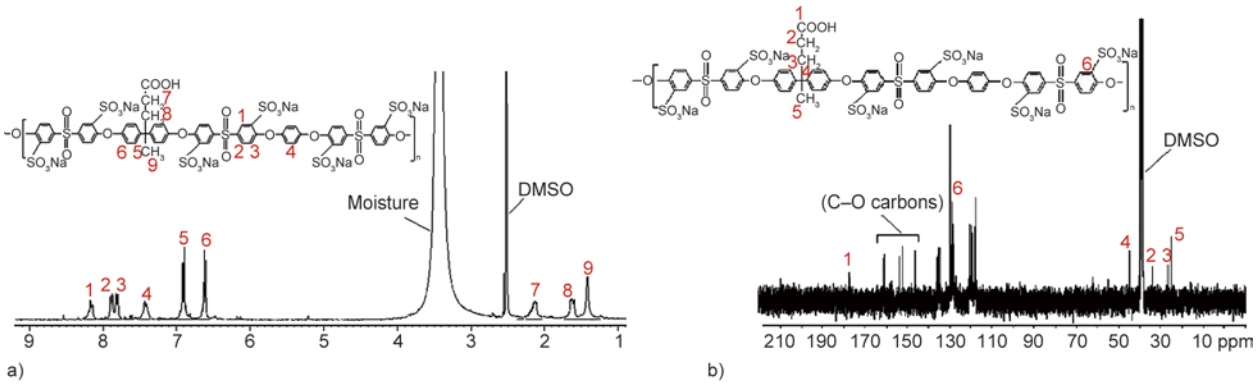

Figure 8. (a) [1]H NMR and (b) [13]C NMR sprectra of SPAES-H-0 copolymer

methylene protons (H_7, H_8) and methyl (H_9) protons of the pentanoic group of DPA showed resonating signals at 2.1, 1.6 and 1.4 ppm, respectively.
Figure 8b shows the ^{13}C NMR spectrum of the SPAES-H-0 copolymer. A characteristic signal for the carboxylic acid group carbon (C_1) appeared at 177 ppm. The peaks for the aromatic carbons were observed in the range of 117–135 ppm. The 147–161 ppm region showed peaks for the C–O carbons. The peaks corresponding to other carbons have also been identified.

4. Ion exchange capacity, water uptake and Swelling ratio

The IEC is determined by titration method at room temperature and the values are summarized in Table 1. The water uptake of the membranes at room temperature is shown in Figure 9. IEC tells about the exchangeable ions in the polymer backbone and is closely related to the water uptake of the membranes. Water acts as a medium for the transportation of the protons according to Ionic cluster network model and Grothuss and Vehicle mechanism [33–36], where protons are believed to be transported along with hydrogen bonded ionic channels and cationic mixtures such as H_3O^+, $H_5O_2^+$, $H_9O_4^+$ in water medium. Therefore, level of hydration of the membranes is dependent on the presence of hydrophilic groups such as carboxylic and sulfonic acid groups. It was observed that IEC capacity and water uptake of the pristine SPAES-H-0 membrane was found to be higher than its counterpart crosslinked membranes. This was because of the more propensities of the pristine membrane to absorb water and form ionic channels by pendant sulfonic acid and carboxylic acid groups for the transport of the protons. The crosslinked membranes showed reduction in water uptake, which might be due to the unavailability of the protons of carboxylic acid groups. These carboxylic groups might have participated in proton transportation in the pristine SPAES-H-0 membrane.
Swelling ratio is also very important property in PEMFC applications because it is related to the dimensional stability, which determines the mechanical stability of the membranes. It can be seen from the Table 2 that for the higher crosslinked membranes swelling ratio was found to decrease due to the formation of tight molecular structure. The presence of hydrophobic CF_3 groups of unreacted epoxy resin also play role in reducing the water uptake and swelling ratio of the crosslinked membranes with the increase in the amount of epoxy resin.

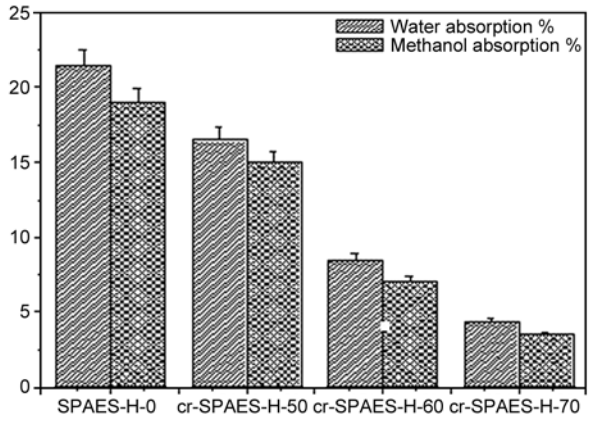

Figure 9. Water and methanol uptake of the SPAES-H-0 and its cr-SPAES-H membranes

Table 1. Properties IEC, proton conductivity and methanol permeability of the membranes at 30°C

Membranes	IEC [meq/g]	Proton conductivity]S/cm]	Methanol permeability [cm^2/s]
SPAES-H-0	$7.4 \cdot 10^{-1}$	$6.8 \cdot 10^{-3}$	–
cr-SPAES-H-50	$6.7 \cdot 10^{-1}$	$5.7 \cdot 10^{-3}$	$4.9 \cdot 10^{-6}$
cr-SPAES-H-60	$5.5 \cdot 10^{-1}$	$4.1 \cdot 10^{-3}$	$3.7 \cdot 10^{-6}$
cr-SPAES-H-70	$3.8 \cdot 10^{-1}$	$3.0 \cdot 10^{-3}$	$2.6 \cdot 10^{-6}$

5. Proton conductivity

Adequate proton conductivity is the prime requirement for PEMs for their applicability in PEMFCs. The water uptake and IEC is directly related to the proton conductivity of the membranes. For the high proton conductivity the polar groups such as sulfonic and carboxylic acid groups play important role. In fully hydrated state the sulfonated polymers

Table 2. Properties water/ methanol uptake, and swelling ratio of the membranes

Membranes	WU [%]			Methanol uptake [%]			Swelling ratio [%]		
	30°C	60°C	80°C	30°C	60°C	80°C	30°C	60°C	80°C
SPAES-H-0	21.5	44	69	19	37	58	–	–	–
cr-SPAES-H-50	16.5	36	54	15	28	39	8	14	36
cr-SPAES-H-60	8.5	17	42	7	13.5	27	5.5	10	23
cr-SPAES-H-70	4.4	8	19	3.5	8	12	4	7.5	15

may slack immobile polar sulfonic acid groups and mobile protons into the solution and form ionic channels for the transport of the protons. The protons get transported from one acid group to another in the form of hydronium ions. From the results tabulated in Table 1 it was observed that proton conductivity of the pristine SPAES-H-0 membrane was $6.8 \cdot 10^3$ S/cm and found to be higher than that of its corresponding crosslinked membranes i.e. 5.7, 4.1 and $3.0 \cdot 10^3$ S/cm for cr-SPAES-H-50, cr-SPAES-H-60 and cr-SPAES-H-70, respectively. This was owing to either reduction or disconnectivity of ionic channels due to bonding of the carboxylic acid groups of the SPAES-H-0 membrane with oxirane rings of the EFN epoxy resin, which leads to decrease in water uptake, IEC and hence proton conductivity of the crosslinked membranes.

5.1. Methanol permeability and selectivity ratio

It was observed that methanol permeability of the pristine membrane could not be found, because the membrane of SPAES-H-0 copolymer was difficult to cast into a definite shape and size due to brittleness of the copolymer. However, it was interesting to note that on crosslinking the copolymer with EFN resin in 50–70% weight ratio of EFN to SPAES-H-0 using a set procedure; well defined cr-SPAES-H membranes were obtained. From the results summarized in Table 1 it was observed that the methanol permeability of the crosslinked membranes decreased as the content of epoxy resin has increased. This was owing to the close packing in case of cr-SPAES-H membranes, which may have contributed towards a decrease in the methanol crossover (Table 3).

In general for the better performance of the PEMs in PEMFCs it should possess high proton conductivity and low methanol permeability. Selectivity ratio is the ratio of the proton conductivity (σ) to methanol permeability (D_K). Higher the value of σ/D_K better will be the performance of the membrane. Figure 10 shows the selectivity ratio of crosslinked membranes cr-SPAES-H-50, cr-SPAES-H-60, cr-SPAES-H-70, respectively. Results revealed that selectivity ratio decreases with the increase in the content of epoxy resin in case of crosslinked membranes. This was due to fall in their proton conductivity, which was due to the absence or reduction in the number of carboxylic acid groups in the crosslinked membranes, which might have participated in proton transportation.

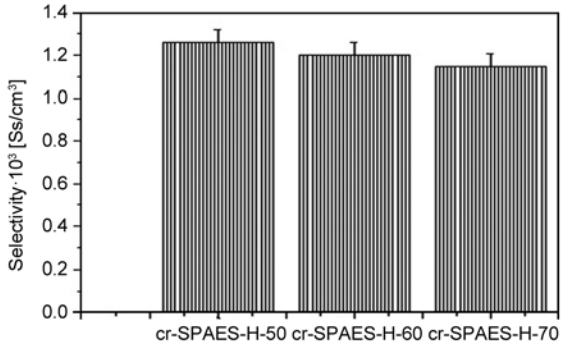

Figure 10. Selectivity ratio of the crosslinked cr-SPAES-H membranes

6. Oxidative stability

Figure 11 shows the weight residue of the membranes as a function of time in Fenton's reagent at 30°C. This method has been used to stimulate the oxidation reaction of the membranes by the attack of free radical species (HO· and HOO·) of Fenton's reagent. The presence of highly electron withdrawing sulfone groups and pendant sulfonic acid groups in the backbone of the polymeric chain might be responsible for the reduction of electron density of the nearby aromatic rings and thus enabling the membranes to exhibit better tolerance for electrophilic attack by these hydroxyl radicals. From the results it was also observed that crosslinked membranes were found to be more stable against the oxidative attack as compared to pristine SPAES-H-0 membrane. This was due to the formation of three dimensional infusible network structure via the reaction between pendant carboxylic acid groups of the main polymeric chain and oxirane ring of EFN epoxy resin.

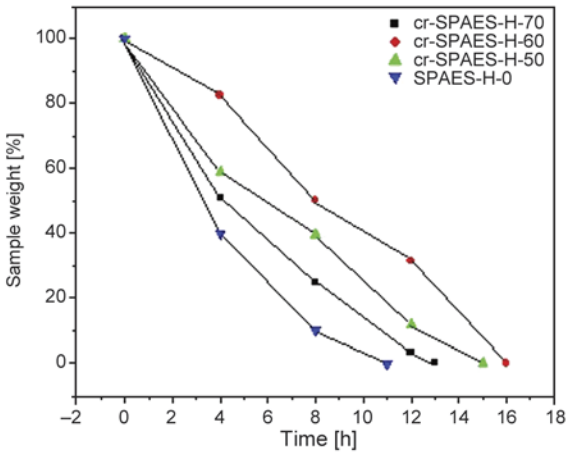

Figure 11. Oxidative stability of the SPAES-H-0 and its cr-SPAES-H membranes

Table 3. Solubility of the membranes in various organic solvents at 30 and 80°C

Membranes	Methanol		CH_2Cl_2		THF		DMAc		NMP		DMSO		Gel fraction[a] [%]
	30°C	80°C	30°C	80°C	30°C	80°C	30°C	80°C	30°C	80°C	30°C	80°C	
SPAES-H-0	–	–	–	–	–	–	+	+	+	+	+	+	–
cr-SPAES-H-50	–	–	–	–	–	–	–	±	–	±	–	±	90
cr-SPAES-H-60	–	–	–	–	–	–	–	±	–	±	–	±	94
cr-SPAES-H-70	–	–	–	–	–	–	–	±	–	±	–	±	97

–: insoluble, +: soluble, ±: swollen

[a][17]

Moreover the enhancement in the oxidative stability of the crosslinked membranes may have led to less water absorption, and since lower the water content, lower will be the attack via the oxidizing species present in water. The carboxylic acid groups present in the pristine membrane a site prone towards oxidation get consumed due to the crosslinking with the epoxy and thus enhance its oxidative stability.

It was observed that cr-SPAES-H-60 membrane was found to possess better oxidative stability as compared to cr-SPAES-H-70 membrane. This was probably due to the presence of excess of epoxy resin in case of cr-SPAES-H-70. Since off-stoichiometric mixture contain latent sites [37], which could remain on the macromolecular structure and can become susceptible for the free radical attack.

7. Morphology of the membranes

Microscopic observation of the surface of the prepared membranes was investigated via tapping mode atomic force microscopy (AFM) and the images of the SPAES-H-0 and its corresponding cr-SPAES-H membranes are shown in Figure 12 and 13, respectively. Examination of the AFM images revealed the presence of light and dark colored domains. The light colored region depicted the hydrophilic domains containing polar groups and dark areas represent the hydrophobic backbone. It can be seen that the light colored domains appeared wide and more distinct in the pristine SPAES-H-0 membrane Figures 12a, 12b. This was due to the fact that polar pendant sulfonic acid and carboxylic acid groups contain small amounts of water which aggregate to form ionic clusters or channels for the transport of the protons. Therefore, the uncrosslinked SPAES-H-0 membranes showed higher proton conductivity. After crosslinking it has been observed the size of these clusters, intensity of the peaks and connectivity among them decreased in case of the crosslinked membranes and can be clearly seen in case of cr-SPAES-50 membrane Figure 13a, 13b. This might be due to the bonding between carboxylic acid groups of the pristine membrane with the oxirane ring of the EFN epoxy resin that cause in the reduction of the ionic channels. In case of cr-SPAES-60 and cr-SPAES-H-70 Figure 13c, 13d membranes the distinction between hydrophillic and hydrophobic domains become difficult due to the formation of highly crosslinked

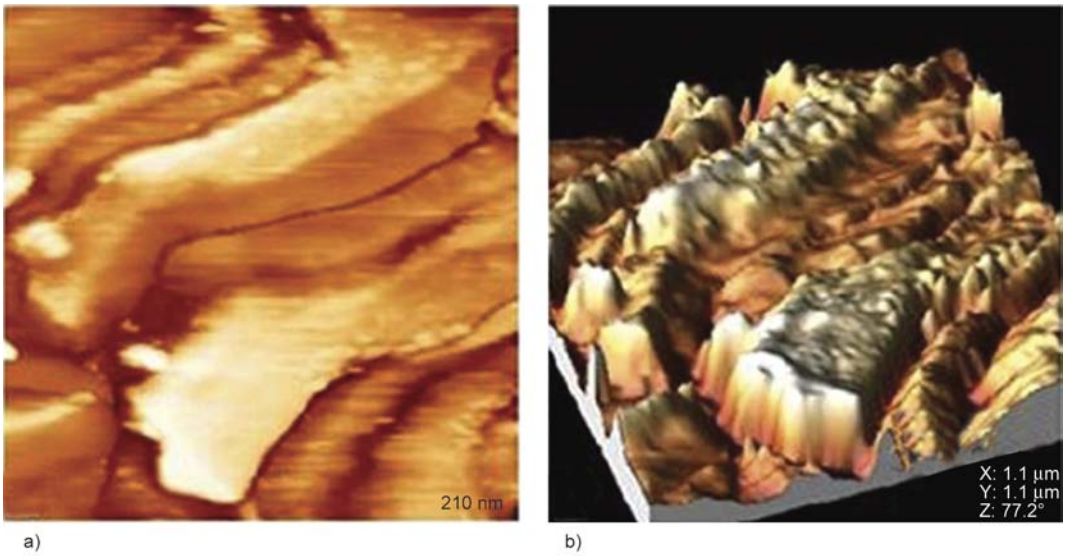

Figure 12. Tapping mode images of membrane (a) SPAES-H-0 in 2D mode and (b) SPAES-H-0 in 3D mode

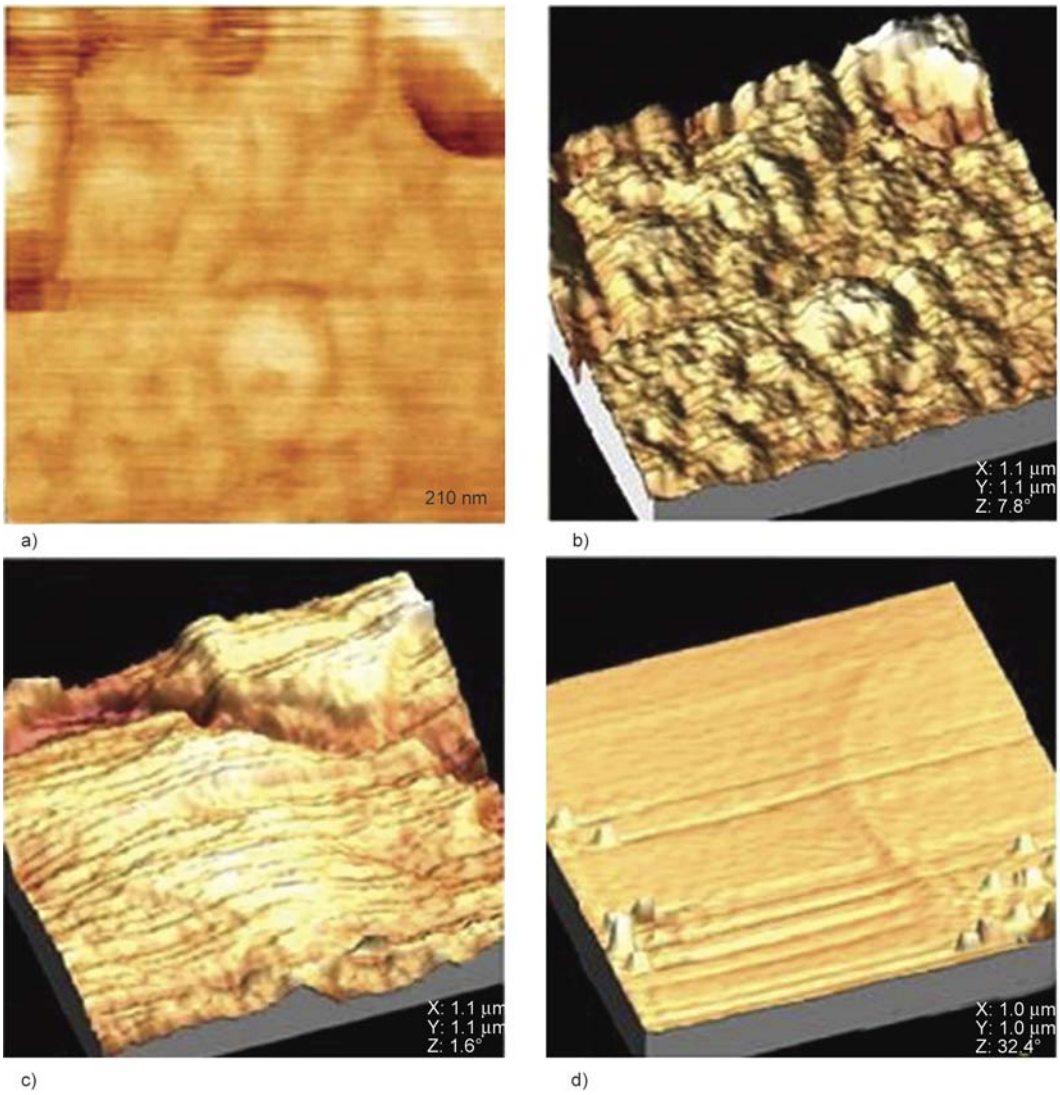

Figure 13. Tapping mode images (a, b) of SPAES-H-50 and (c, d) of cr-SPAES-H-60, cr-SPAES-H-70 membranes, respectively

network structures and decrease in hydrophillic carboxylic acid groups. The increment in hydrophobic CF_3 groups of EFN resin was also another dilemma for no clear distinction between hydrophillic and hydrophobic domains in case of cr-SPAES-60 and cr-SPAES-H-70 membranes. These results concurred well with the water uptake, swelling ratio, ion exchange capacity and proton conductivity values which were found to be lesser in case of the crosslinked membranes.

8. X-ray diffraction study

Figure 14 shows the X-Ray diffractograms of the uncrosslinked SPAES-H-0 and its crosslinked cr-SPAES-H-50, cr-SPAES-H-60 and cr-SPAES-H-70 membranes, respectively. It can be seen from the Figure 14 that after crosslinking the width of the peaks at $2\theta = 28, 31, 32, 44°$, respectively was found to increase in case of cr-SPAES-H-50 membrane as compared to pure SPAES-H-0 membrane. It can also be seen from the figure that the peaks at $2\theta = 18, 19, 27°$ and in the region of 31–33, 35–39, 41–49, 51–57°, respectively have disappeared in the case of cr-SPAES-H-60 membrane. The intensity of peak at $2\theta = 34°$, has been reduced in case of cr-SPAES-H-60 and cr-SPAES-H-70 membranes. The increase in the width of the peaks, decrease in the intensity and disappearance of the peaks indicated the reduction of crystalline nature of the crosslinked membranes. Hence, it can be concluded that crosslinking of the SPAES-H-0 membrane with EFN epoxy resin reduced the crystalline behaviour of the crosslinked membranes.

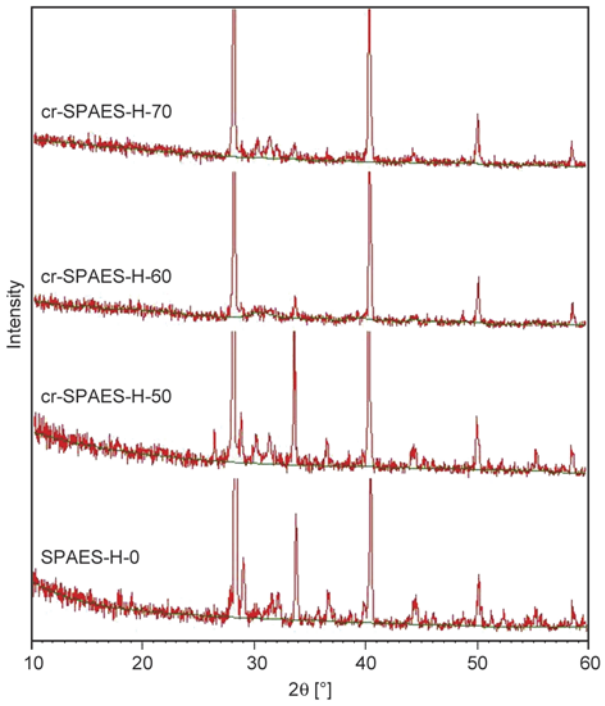

Figure 14. XRD graphs of SPAES-H-0 and its corresponding crosslinked membranes

9. Mechanical properties

The mechanical stability of the membranes is one of the decisive parameters in determining the performance of the membranes because toughness and elasticity are also important factors of the membranes in addition to high proton conductivity for fuel cell applications. The stress strain behaviour of the membranes has been depicted in Figure 15 and results are summarized in Table 4. From the results it can be observed that cr-SPAES-H-60 membrane exhibit superior tensile strength, young's modulus and elongation at break as compared to its corresponding cr-SPAES-H-50 and cr-SPAES-H-70 membranes. The increase in the elongation at break values with the crosslinking could be related to the decrease in crystallinity of the polymeric chains, which is found in good agreement with the obtained X- ray analysis results.

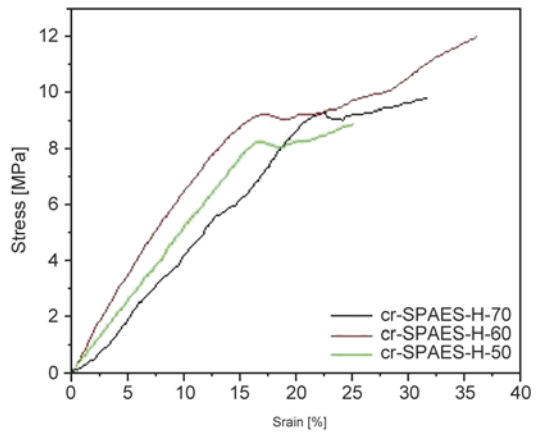

Figure 15. Stress vs strain behavior of the SPAES-H-0 and its cr-SPAES-H membranes

Table 4. Mechanical properties of the membranes

Membranes	Tensile strength [MPa]	Young's Modulus [MPa]	Elongation at break [%]
SPAES-H-0	–	–	–
cr-SPAES-H-50	8.9	49.93	24.63
cr-SPAES-H-60	12.03	55.65	36.31
cr-SPAES-H-70	9.79	41.31	32.13

10. Thermal properties

Thermal stability of the PEMs is significant for their durability during fuel cell operation at elevated temperature, it was evaluated using TGA technique and the results are presented in the Figure 16 and Table 5. The weight loss observed below 200°C was due to evaporation of absorbed water. Above 200°C the two step degradation profile was observed for all the membranes. The weight loss from 200–500°C region was attributed to the loss of sulfonic acid groups, whereas the weight loss above 700°C was assigned to the decomposition of the main chain

Table 5. Thermal behaviour description by differential scanning calorimetery and thermo gravimetric analysis

Membranes	T_g [°C]	T_g [°C]	Char residue at 700°C [%]	LOI
SPAES-H-0	161	230	73.62	46.94
cr-SPAES-H-50	188	245	30.09	29.53
cr-SPAES-H-60	–	258	50.57	37.72
cr-SPAES-H-70	148	262	55.36	39.64

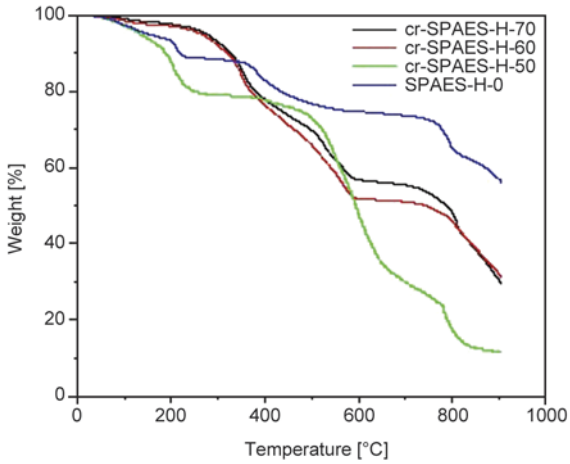

Figure 16. TGA thermograms for the SPAES-H-0 and its corresponding crosslinked membranes

of the polymer. It has been observed that the decomposition temperature for the loss of sulfonic acid groups (T_s) in case of pristine SPAES-H-0 membrane was at 370°C and for crosslinked membranes was at 500°C. The higher T_s for the crosslinked membranes was due to the increased interactions between carboxylic acid groups of the polymeric membranes and the epoxy groups of the EFN resin. Thus the results of thermogravimetric analysis confirmed that crosslinking enhances the thermal stability of the membranes and makes the membranes more suitable for high temperature operating fuel cell applications.

The limiting oxygen index (LOI) value has been calculated by using Krevelen's equation [38] in order to confirm the flame retardancy of the synthesized membranes. All the membranes have LOI values greater than 27 which indicate the better flame resistance behaviour of the synthesized membranes.

10.1. Differential Scanning Calorimetery

Differential Scanning Calorimetery measurement of the membranes was carried out by using heating-cooling- heating procedure. The purpose of the first heating cycle was to remove any thermal history of the synthesized copolymer. Figure 17 shows the DSC scans for the pristine SPAES-H-0 and its crosslinked membranes, the results are summarized in Table 5. The glass transition temperature (T_g) of a polymer is the temperature at which polymeric chain segments in the amorphous regions of the polymer attain sufficient heat energy to move in a coordinated manner. From the results it was observed that the T_g for the crosslinked membranes is higher than their corresponding pristine SPAES-H-0 membrane. This might be due to the increased intermolecular interactions between polymer chain segments and crosslinker (EFN). It can be seen that the SPAES-H membranes showed two glass transition temperatures. The lower and upper T_g's for the SPAES-H-0 and cr-SPAES-50 membranes were attributed to the hydrophobic backbone and hydrophillic ionic clusters, respectively. The appearance of single T_g in case of cr-SPAES-60 indicated that all the carboxylic acid groups of the polymer backbone have been consumed during the crosslinking reaction with the oxirane rings of the epoxy resin. This resulted into the formation of a three dimensional infusible network structure. However, cr-SPAES-H-70 which has an off stoichiometric mixture shows two glass transition temperatures, since it contains unreacted epoxy resin. Therefore, it can be concluded that crosslinked membranes synthesized in the present work showed improved thermal properties which are good enough to use them as PEMs in fuel cell applications.

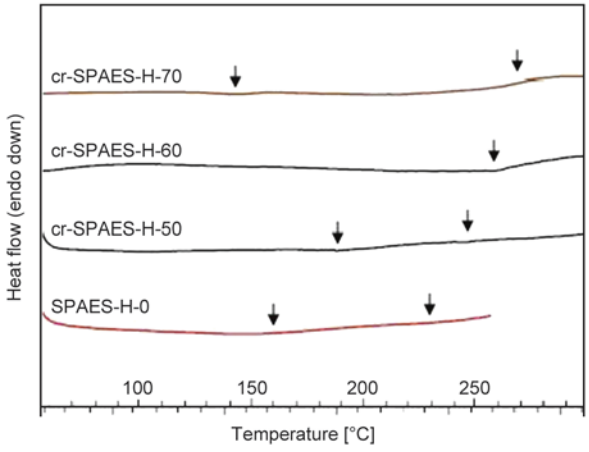

Figure 17. DSC scans for the SPAES-H-0 and its corresponding crosslinked membranes

11. Conclusions

The sulfonated poly (arylene ether sulfone) copolymer (SPAES-H-0) has been synthesized and subsequently crosslinked with EFN epoxy resin. The properties and performance of the membranes before and after crosslinking were characterized by various ways. It has been observed that the crosslinked membranes showed reduction in the IEC, water and methanol uptake, proton conductivity and selectivity ratio with improvement in the oxidative stability and mechanical properties. Crosslinking also reduces the crystalline character of the membranes. As the ratio of the EFN resin has been increased the intensity of the peaks, size of the ionic channels and connectivity among them decreased as confirmed by AFM microscopy. The crosslinked membranes also showed high thermal stability in the temperature range of the PEMFC applications. Hence crosslinking of the SPAES-H-0 copolymer with EFN resin is found to be a suitable method for balancing high proton conductivity due to excessive water uptake and mechanical strength of the membranes for their usage in fuel cell applications.

References

[1] Aili D., Cleemann L. N., Li Q., Jensen J. O., Christensen E., Bjerrum N. J.: Thermal curing of PBI membranes for high temperature PEM fuel cells. Journal of Materials Chemistry, **22**, 5444–5453 (2012). DOI: 10.1039/C2JM14774B

[2] Yoon Y. J., Kim T-H., Yu D. M., Hong Y. T.: Sulfonated poly(arylene ether sulfone)/disulfonated silsesquioxane hybrid proton conductors for proton exchange membrane fuel cell application. International Journal of Hydrogen Energy, **37**, 18981–18988 (2012). DOI: 10.1016/j.ijhydene.2012.09.078

[3] Li G., Xie J., Cai H., Qiao J.: New highly proton-conducting membrane based on sulfonated poly(arylene ether sulfone)s containing fluorophenyl pendant groups, for low-temperature polymer electrolyte membrane fuel cells. International Journal of Hydrogen Energy, **39**, 2639–2648 (2014). DOI: 10.1016/j.ijhydene.2013.11.049

[4] Lee K. S., Jeong M. H., Lee J. P., Kim Y. J., Lee J. S.: Synthesis and characterization of highly fluorinated cross-linked aromatic polyethers for polymer electrolytes. Chemistry of Materials, **22**, 5500–5511 (2010). DOI: 10.1021/cm101405h

[5] Thankamony R. L., Baek G., Kim H-J., Nam S-W., Kim T-H.: Terminally-crosslinked sulfonated poly(fluorenyl ether sulfone) as a polymer electrolyte membrane for both PEMFC and DMFC application. Bulletin of the Korean Chemical Society, **31**, 2141–2142 (2010). DOI: 10.5012/bkcs.2010.31.8.2141

[6] Swier S., Chun Y. S., Gasa J., Shaw M. T., Weiss R. A.: Sulfonated poly(ether ketone ketone) ionomers as proton exchange membranes. Polymer Engineering and Science, **45**, 1081–1090 (2005). DOI: 10.1002/pen.20361

[7] Chen Y., Meng Y., Wang S., Tian S., Chen Y., Hay A. S.: Sulfonated poly(fluorenyl ether ketone) membrane prepared via direct polymerization for PEM fuel cell application. Journal of Membrane Science, **280**, 433–441 (2006). DOI: 10.1016/j.memsci.2006.01.052

[8] Wang F., Hickner M., Kim Y. S., Zawodzinski T. A., McGrath J. E.: Direct polymerization of sulfonated poly (arylene ether sulfone) random (statistical) copolymers: Candidates for new proton exchange membranes. Journal of Membrane Science, **197**, 231–242 (2002). DOI: 10.1016/S0376-7388(01)00620-2

[9] Matsumoto K., Higashihara T., Ueda M.: Locally sulfonated poly(ether sulfone)s with highly sulfonated units as proton exchange membrane. Journal of Polymer Science Part A: Polymer Chemistry, **47**, 3444–3453 (2009). DOI: 10.1002/pola.23403

[10] Wu H-L., Ma C-C. M., Liu F-Y., Chen C-Y., Lee S-J., Chiang C-L.: Preparation and characterization of poly (ether sulfone)/sulfonated poly(ether ether ketone) blend membranes. European Polymer Journal, **42**, 1688–1695 (2006). DOI: 10.1016/j.eurpolymj.2006.01.018

[11] Li D., Li Z., Hu F., Long S., Zhang G., Yang J.: Pendant crosslinked poly(aryl ether sulfone) copolymers sulfonated on backbone for proton exchange membranes. Polymer Engineering and Science, **54**, 2013–2022 (2014). DOI: 10.1002/pen.23754

[12] Mabrouk W., Ogier L., Vidal S., Sollogoub C., Matoussi F., Fauvarque J. F.: Ion exchange membranes based upon crosslinked sulfonated polyethersulfone for electrochemical applications. Journal of Membrane Science, **452**, 263–270 (2014). DOI: 10.1016/j.memsci.2013.10.006

[13] Guo M., Liu B., Guan S., Li L., Liu C., Zhang Y., Jiang Z.: Novel sulfonated poly(ether ether ketone)s containing nitrile groups and their composite membranes for fuel cells. Journal of Power Sources, **195**, 4613–4621 (2010). DOI: 10.1016/j.jpowsour.2010.02.036

[14] Gao Y., Robertson G. P., Kim D-S., Guiver M. D., Mikhailenko S. D., Li X., Kaliaguine S.: Comparison of PEM properties of copoly(aryl ether ether nitrile)s containing sulfonic acid bonded to naphthalene in structurally different ways. Macromolecules, **40**, 1512–1520 (2007). DOI: 10.1021/ma0623542

[15] Endo N., Matsuda K., Yaguchi K., Hu Z., Chen K., Higa M., Okamoto K.: Cross-linked sulfonated polyimide membranes for polymer electrolyte fuel cells. Journal of the Electrochemical Society, **156**, 8628–8633 (2009). DOI: 10.1149/1.3097180

[16] Gong C., Luo Q., Li Y., Giotto M., Cipollini N. E., Yang Z., Weiss R. A., Scola D. A.: Dual crosslinked phenylethynyl end-capped sulfonated polyimides *via* the ethynyl and sulfonate groups promoted by PEG. Journal of Polymer Science Part A: Polymer Chemistry, **49**, 4476–4491 (2011). DOI: 10.1002/pola.24889

[17] Ding F. C., Wang S. J., Xiao M., Meng Y. Z.: Cross-linked sulfonated poly(phathalazinone ether ketone)s for PEM fuel cell application as proton-exchange membrane. Journal of Power Sources, **164**, 488–495 (2007). DOI: 10.1016/j.jpowsour.2006.11.028

[18] Mader J., Xiao L., Thomas J., Schmidt T. J., Benicewicz B. C.: Polybenzimidazole/acid complexes as high-temperature membranes. Advances in Polymer Science, **216**, 63–124 (2008). DOI: 10.1007/12_2007_129

[19] Qi Y., Gao Y., Tian S., Hill A. R., Gaudet J., Guay D., Hay A. S.: Synthesis and properties of novel benzimidazole-containing sulfonated polyethersulfones for fuel cell applications. Journal of Polymer Science Part A: Polymer Chemistry, **47**, 1920–1929 (2009).
DOI: 10.1002/pola.23298

[20] Maity S., Jana T.: Soluble polybenzimidazoles for PEM: Synthesized from efficient, inexpensive, readily accessible alternative tetraamine monomer. Macromolecules, **46**, 6814–6823 (2013).
DOI: 10.1021/ma401404c

[21] Maity S., Jana T.: Polybenzimidazole block copolymers for fuel cell: Synthesis and studies of block length effects on nanophase separation, mechanical properties, and proton conductivity of PEM. Applied Materials and Interfaces, **6**, 6851–6864 (2014).
DOI: 10.1021/am500668c

[22] Maity S., Jana T.: Polycondensation of structurally divergent tetraamine monomers with dicarboxylic acids to synthesize polybenzimidazole copolymers for polymer electrolyte membranes. Polymer International, **64**, 530–540 (2015).
DOI: 10.1002/pi.4830

[23] Duangkaew P., Wootthikanokkhan J.: Methanol permeability and proton conductivity of direct methanol fuel cell membranes based on sulfonated poly(vinyl alcohol)–layered silicate nanocomposites. Journal of Applied Polymer Science, **109**, 452–458 (2008).
DOI: 10.1002/app.28072

[24] Krishnan N. N., Kim H-J., Prasanna M., Cho E., Shin E-M., Lee S-Y., Oh I-H., Hong S-A., Lim T-M.: Synthesis and characterization of sulfonated poly(ether sulfone) copolymer membranes for fuel cell applications. Journal of Power Sources, **158**, 1246–1250 (2006).
DOI: 10.1016/j.jpowsour.2005.09.064

[25] Lee K. H., Chu J. Y., Kim A. R., Nahm K. S., Yoo D. J.: Highly sulfonated poly(arylene biphenylsulfone ketone) block copolymers prepared *via* post-sulfonation for proton conducting electrolyte membranes. Bulletin of the Korean Chemical Society, **34**, 1763–1770 (2013).
DOI: 10.5012/bkcs.2013.34.6.1763

[26] Han S., Zhang M-S., Shin J., Lee Y-S.: A convenient crosslinking method for sulfonated poly(ether ether ketone) membranes *via* friedel–crafts reaction using 1,6-dibromohexane and aluminum trichloride. Journal of Applied Polymer Science, **131**, 40695/1–40695/7 (2014).
DOI: 10.1002/app.40695

[27] Tong J. Y. Guo Q., Wang X. X.: Properties and structure of SPEEK proton exchange membrane doped with nanometer CeO_2 and treated with high magnetic field. Express Polymer Letters, **3**, 821–831 (2009).
DOI: 10.3144/expresspolymlett.2009.101

[28] Boroglu M. S., Cavus S., Boz I., Ata A.: Synthesis and characterization of poly(vinyl alcohol) proton exchange membranes modified with 4,4-diaminodiphenylether-2,2-disulfonic acid. Express Polymer Letters, **5**, 470–478 (2011).
DOI: 10.3144/expresspolymlett.2011.45

[29] Zhao Y., Yin J.: Synthesis and evaluation of all-block-sulfonated copolymers as proton exchange membranes for fuel cell application. Journal of Membrane Science, **351**, 28–35 (2010).
DOI: 10.1016/j.memsci.2010.01.024

[30] Kiran V., Gaur B.: Sulfonated poly (arylene ether sulfone) proton exchange membranes for fuel cell applications. Green Processing and Synthesis, **4**, 2191–9542 (2015).
DOI: 10.1515/gps-2015-0024

[31] Han M., Zhang G., Li M., Wang S., Liu Z., Li H., Zhang Y., Xu D., Wang J., Ni J., Na H.: Sulfonated poly(ether ether ketone)/polybenzimidazole oligomer/epoxy resin composite membranes *in situ* polymerization for direct methanol fuel cell usages. Journal of Power Sources, **196**, 9916–9923 (2011).
DOI: 10.1016/j.jpowsour.2011.08.049

[32] Guhan S., Sangeetha D.: Evaluation of sulfonated poly (ether ether ketone) silicotungstic acid composite membranes for fuel cell applications. International Journal of Polymeric Materials and Polymeric Biomaterials, **58**, 87–98 (2008).
DOI: 10.1080/00914030802565442

[33] Hsu W. Y., Gierke T. D.: Ion transport and clustering in Nafion perfluorinated membranes. Journal of Membrane Science, **13**, 307–326 (1983).
DOI: 10.1016/S0376-7388(00)81563-X

[34] Smitha B., Sridhar S., Khan A. A.: Solid polymer electrolyte membranes for fuel cell applications – A review. Journal of Membrane Science, **259**, 10–26 (2005).
DOI: 10.1016/j.memsci.2005.01.035

[35] Agmon N.: The Grotthuss mechanism. Chemical Physics Letters, **244**, 456–462 (1995).
DOI: 10.1016/0009-2614(95)00905-J

[36] Moilanen D. E., Spry D. B., Fayer M. D.: Water dynamics and proton transfer in Nafion fuel cell membranes. Langmuir, **24**, 3690–3698 (2008).
DOI: 10.1021/la703358a

[37] d'Almeida J. R. M., de Menezes G. W., Monteiro S. N.: Ageing of the DGEBA/TETA epoxy system with off-stoichiometric compositions. Materials Research, **6**, 415–420 (2003).
DOI: 10.1590/S1516-14392003000300017

[38] van Krevelen D. W.: Some basic aspects of flame resistance of polymeric materials. Polymer, **16**, 615–620 (1975).
DOI: 10.1016/0032-3861(75)90157-3

eXPRESS Polymer Letters Vol.9, No.12 (2015) 1068–1075
Available online at www.expresspolymlett.com
DOI: 10.3144/expresspolymlett.2015.96

Facile and simple preparation of pH-sensitive chitosan-mesoporous silica nanoparticles for future breast cancer treatment

W. T. Liu[1*], *Y. Yang*[1], *P. H. Shen*[2], *X. J. Gao*[1], *S. Q. He*[1], *H. Liu*[1], *C.S. Zhu*[1]

[1]School of Material Science and Engineering, Zhengzhou University, 450052 Zhengzhou, Henan province, China
[2]The Fifth Affiliated Hospital of Zhengzhou University, 450052 Zhengzhou, Henan province, China

Received 26 April 2015; accepted in revised form 8 July 2015

Abstract. The nanocarrier is linked to the core and shell by hydrogen bond. This drug delivery system represents a smart, biodegradable, and pH-sensitive nanocarrier for breast cancer therapy. These drug nanocarriers were linked by hydrogen bond from $–NH_2$ on chitosan and –OH on mesoporous silica nanoparticle (MSN). And MSN was prepared by the cetyltrimethyl ammonium bromide (CTAB)-templated method *via* sol-gel and the loading of ibuprofen (IBU) into the pores of MSN was visualized by coprecipitation which was assessed by Fourier Transform Infrared Spectroscopy (FTIR) and nitrogen adsorption-desorption techniques. The wrapping of chitosan (CS) onto the surface of MSN was demonstrated by FTIR too. When the nanocarriers entered an acidic environment where large quantity cancer cells existed, the chitosan shell swell into loose random coil, exposing the drug and making them easy to be released. The results showed that the IBU could be successfully and effectively loaded into MSN and CS/MSN. The system was pH responsive. Drug release was much higher at pH 6.8 than at 7.4. This drug delivery system will represent a smart and biodegradable pH-responsive nanocarrier for breast cancer.

Keywords: *smart polymers, chitosan, MSN, pH-sensitive nanoparticles, drug delivery system*

1. Introduction

For cancer therapy, people have found that drug controlled delivery system [1] could control the release of drugs and significantly reduce the side effects in recent years [2–6]. Moreover, pH-responsive drug controlled delivery system [7–13] can release drug at certain part of body, because pH value is different at each part of the human body. The normal body fluid pH is about 7.4, while the pH value at cancer cell is approximately 6.8. Several biodegradable materials, such as chitosan [14], polylactic acid [15], gelatin [16], polycaprolactone [17] and poly-alkyl-cyanoacrylates [18] have been used as intelligent drug delivery systems. In the meanwhile, some inorganic nanoparticles like mesoporous silica (MSN), Fe_3O_4, carbon nanotubes, quantum dots [19–22] are also used as drug delivery systems.

MSN has been widely used in biomedical due to its good biocompatibility, non-toxic, tunable pore size, large surface areas and pore volume, modifiable surface, biodegradation, good chemical and thermal stabilities and other advantages [19, 23–26]. But unmodified MSN is not intelligent and has potential toxicity at high dose because of the interactions of surface silanols with cellular membranes [27, 28]. So it is necessary to wrap MSN with biomolecules, so that the system is intelligent and low toxicity [28, 29]. Chitosan has been widely used in intelligent drug delivery system because it has unique properties

*Corresponding author, e-mail: wtliu@zzu.edu.cn

such as non-toxicity, biocompatibility, biodegradability, and so on [30]. The ionization of large quantities of amino groups on chains of chitosan provides it as a pH-sensitive 'gatekeeper'.

Many polymer-coated and pH-sensitive MSN nanocarriers have been designed, while most of the system add poisonous solvent and the preparation process is complex. In the present work, we have developed a simple and facile approach to prepare an intelligent drug controlled delivery system by hydrogen bonding biopolymer as pH-responsive 'gatekeeper' and inorganic nanoparticles as drug carriers. Meanwhile, the system is sensitive to a narrow pH range. We described a pH-responsive drug nanocarrier based on MSNs, which was wrapped by chitosan. And drug controlled release was studied at pH 7.4 and 6.8 which used IBU as a model drug.

2. Experimental section

2.1. Materials

Cetyltrimethylammonium bromide (Tianjin Jinbei Fine Chemical Co., Ltd, China), tetraethyl orthosilicate (TEOS, analytical reagent, Tianjin Fuchen chemical reagent factory, China), mesitylene (Aladdin Industrial Corportion, China), chitosan (CS, M_W = 110 000–150 000, Amresco, USA), sodium hydroxide (NaOH, Tianjin DeEn Chemical Co., Ltd, China), n-hexane (C_6H_{14}, Tianjin Fengchuan Chemical Co., Ltd, China), ethanol (CH_3CH_2OH, Tianjin Fengchuan Chemical Co., Ltd,China), ammonium nitrate (NH_4NO_3, Tianjin Jinbei Fine Chemical Co., Ltd, China).

2.2. Characterization

Fourier transform infrared spectroscopy analysis was performed by using KBr in the region of 4000–400 cm^{-1} by Nicolet PROTE/GE/460. Surface analysis of the nanoparticles was performed by N_2 adsorption-desorption isotherm curves. Brunauer-Emmett-Teller (BET) surface areas were calculated by the BET method and the pore size distribution was calculated by the Barrett-Joyner-Halenda (BJH) method deduced from desorption data (Quadrasorb-evo, Quantachrome Instrument, USA). Transmission electron microscopy (TEM) images were measured with field-emission transmission electron microscopy (JEM-2100, Japan). Ultraviolet-visible (UV-vis) absorption spectra were analyzed by a SHIMADZU (UV-2401PC, Japan). The pH value was measured with a pH meter (PHS-3C, Shanghai INESA Scientific Instrument Co. Ltd., China).

2.3. Preparation of mesoporous silica nanoparticles (MSNs)

Mesoporous silica nanoparticles were prepared by sol-gel method [31]. Briefly, a certain amount of CTAB and 0.28 g NaOH was dissolved in 480 mL deionized water. Then pore-expanding agent 7.0 mL mesitylene was added to the solution. The mixture was stirred vigorously and heated to 80°C. Afterwards, 5.0 mL TEOS was added dropwise at a proper rate to the solution. The reaction mixture was stirred vigorously at 80°C for another 2 h. The resulting white precipitate was isolated by filtration, washed with abundant ethanol and dried under vacuum at 100°C for 12 h.

The structure-templating CTAB and mesitylene molecules were removed from the composite material *via* solvent extraction. A suspension of 1.0 g of the as synthesized material was stirred for 5 h at 60°C in a 150 mL ethanol solution with 0.4 g NH_4NO_3 adding in. The template-removed nanoparticles were then isolated *via* filtration and dried under vacuum at room temperature.

2.4. Loading IBU into MSNs (MSN/IBU)

0.5 g MSNs were added to 30 mL IBU n-hexane solution (40 mg/mL). Then the mixture was stirred at room temperature for two days. After that, MSN/IBU was centrifuged and the resulting supernatant was analyzed by using UV-vis spectrophotometry at a λ_{max} of 264 nm to evaluate the absorbed IBU into MSNs.

2.5. Chitosan wrapping MSN/IBU (CS/MSN/IBU)

0.2, 0.4, 0.6 W/V CS/acetic acid (10% V/V) aqueous solution was prepared and the pH was adjusted to 6.0 with 1M NaOH. Then 0.2 g MSN/IBU were added to 40 mL CS/acetic acid aqueous solution and stirred for 36 h at room temperature. The mixture was centrifuged, washed with deionized water twice and dried under vacuum at room temperature.

2.6. *In vitro* release of IBU

The *in vitro* release of IBU was measured by preparing equal weight MSN/IBU and CS/MSN/IBU in pH 6.8 and pH 7.4 PBS buffer solutions at concen-

tration of 4 mg/mL. The mixture was keeping stirred at rate of 30 r/min and releasing temperature was kept at 37°C. Then release was determined by taking 3 mL of the IBU release medium for UV-vis analysis at 1 h intervals and replaced with the same volume of fresh PBS buffer solutions, which were preheated to 37°C.

3. Results and discussion

3.1. Morphologies and structures of MSNs and CS/MSN/IBU

In this study, four kinds of MSNs were prepared *via* different concentrations of CTAB (Figures 1–4, Table 1). When concentration of CTAB was 5.7 mM, the prepared MSN had the larger pore volume and

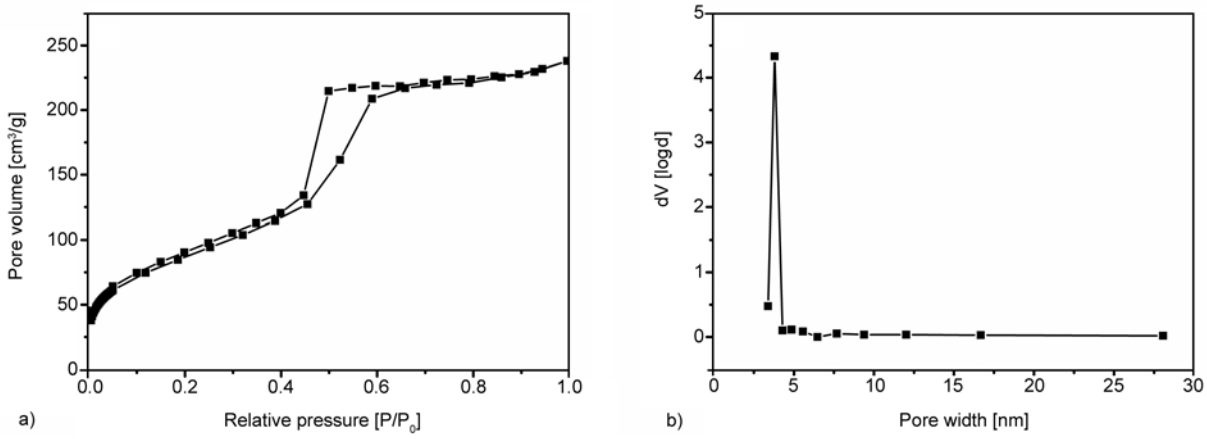

Figure 1. N_2 adsorption-desorption isotherms of mesoporous silica (a) and pore size distribution (b), (Concentration of CTAB is 1.9 mM)

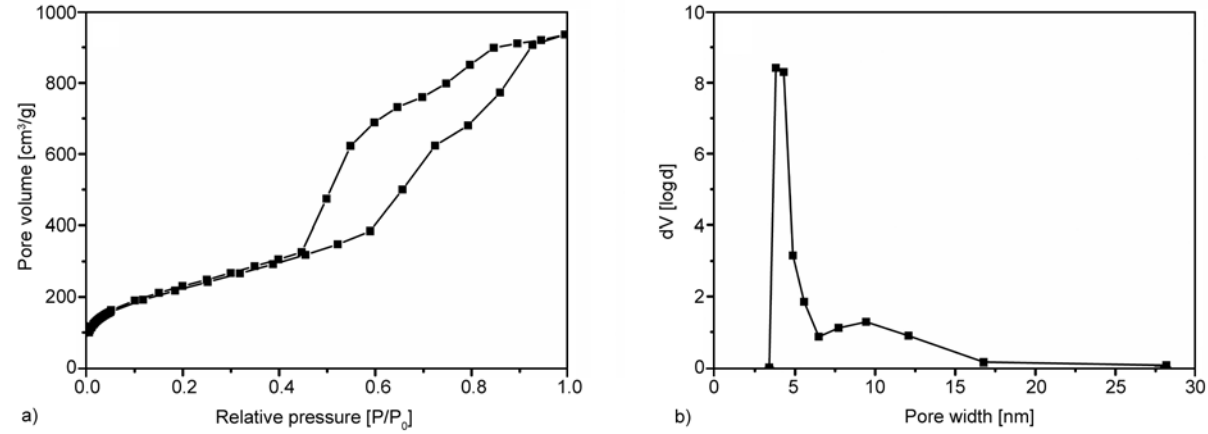

Figure 2. N_2 adsorption-desorption isotherms of mesoporous silica (a) and pore size distribution (b), (Concentration of CTAB is 3.8 mM)

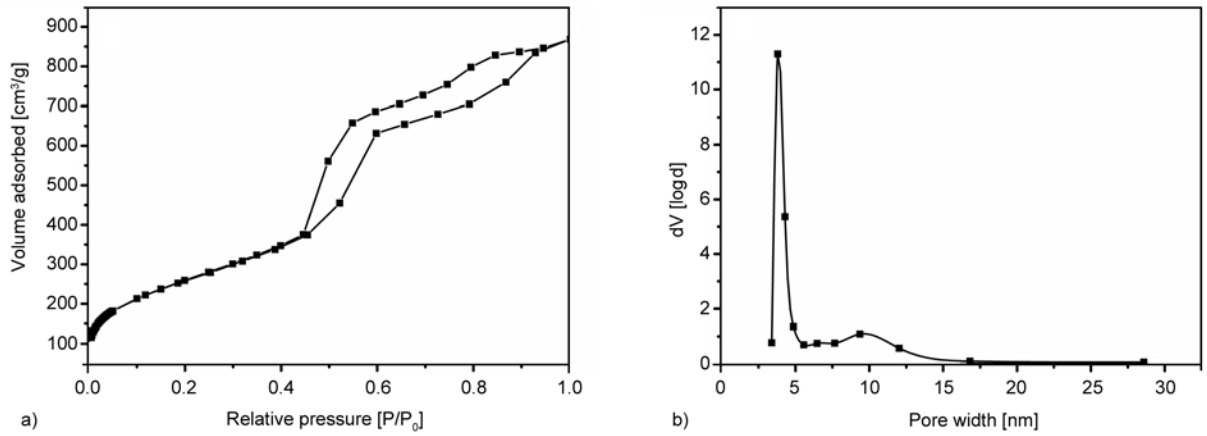

Figure 3. N_2 adsorption-desorption isotherms of mesoporous silica (a) and pore size distribution (b), (Concentration of CTAB is 5.7 mM)

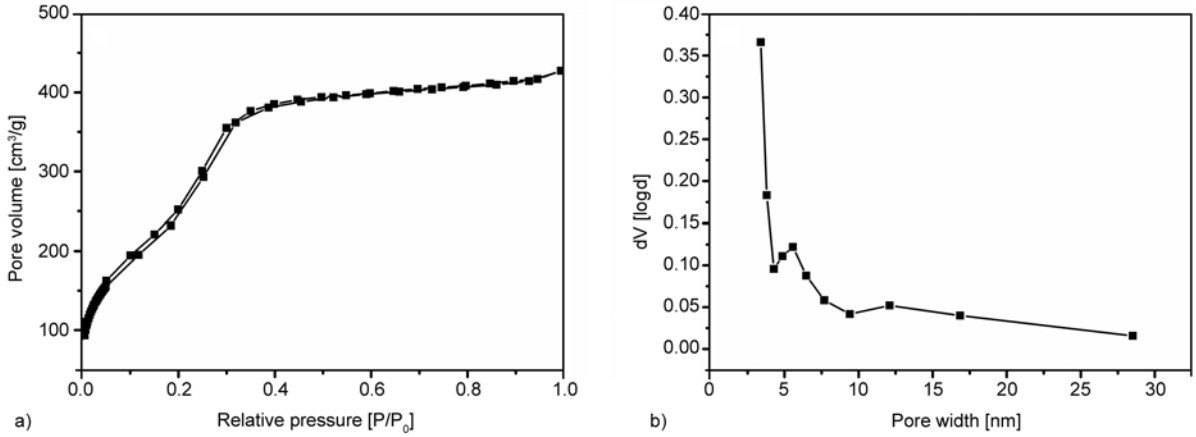

Figure 4. N_2 adsorption-desorption isotherms of mesoporous silica (a) and pore size distribution (b), (Concentration of CTAB is 7.6 mM)

Table 1. Structure parameters of MSN and MSN/IBU

Samples	Concentration of CTAB [mM]	BET surface area [m^2/g]	Pore volume [cm^3/g]	Small mean pore [nm]	Large mean pore [nm]
MSN1	1.9	267.1	0.29	3.8	9.3
MSN2	3.8	818.2	1.61	3.8	9.3
MSN3	5.7	948.1	1.34	3.8	9.8
MSN4	7.6	991.1	0.09	3.4	9.8
MSN/IBU	5.7	282.1	0.34	3.8	9.5

BET surface area. So in this study we chose MSN3 as drug nanocarrier. Figure 5 showed the average diameter of the prepared MSN was 200 nm. The MSN had regular array of mesoporous channels and large enough pores to load IBU inside. The TEM image of the chitosan wrapped MSN confirmed that chitosan successfully wrapped on the surface of MSN and CS/MSN/IBU still showed regular spherical structure.

As the concentration of CTAB increases, the size of the micelles formed in the solution became larger. CTAB might have been partially adsorbed inside the silica channel, with the result that template was not removed completely in the final and the BET surface area and pore volume decreased sharply.

The N_2 adsorption-desorption isotherm curve of MSN showed a typical IV isotherm curve. The BET surface area is 948.1 m^2/g and pore volume is

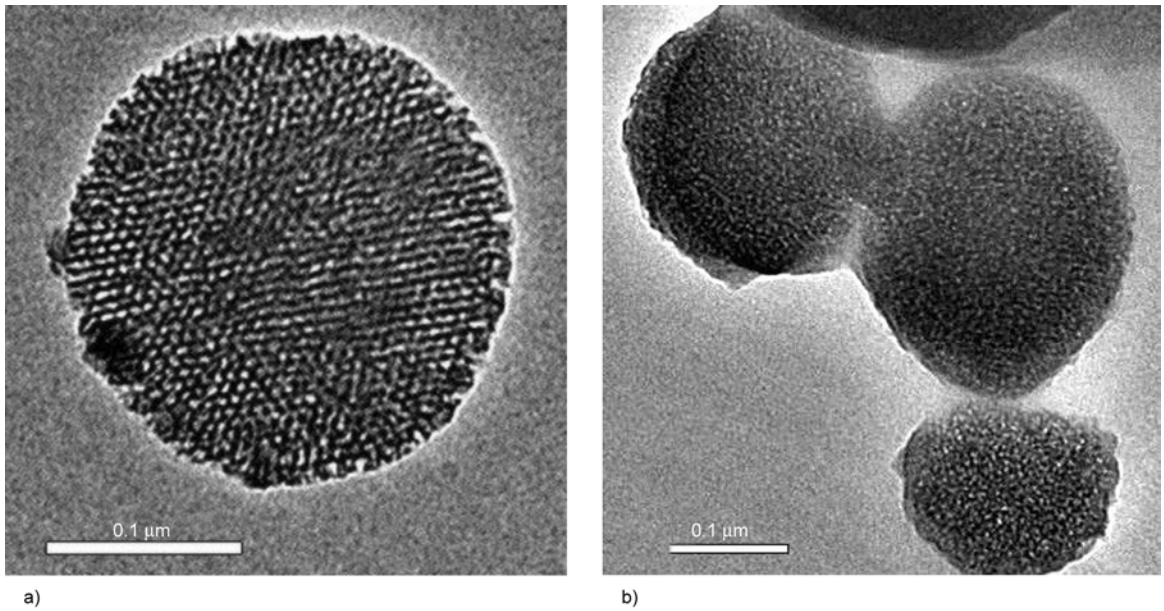

Figure 5. TEM images of MSN (a) and CS/MSN/IBU (b)

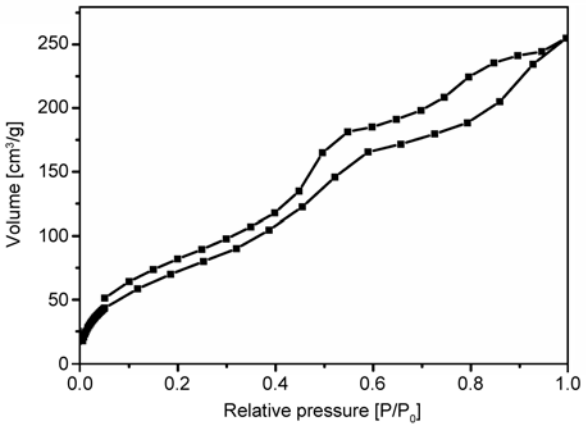

Figure 6. N_2 adsorption-desorption isotherm curve of MSN/IBU

1.34 cm^3/g for MSN3 (Figure 3a, Table 1). The BJH method showed two pore size distributions centered on 3.8 nm (major) and 9.8 nm (minor) (Figure 3b, Table 1).

The structures of the nanoparticles were characterized by FTIR. As shown in Figure 7, the FTIR spectrums of MSN, MSN/IBU and CS/MSN/IBU show a hydroxyl absorption peak at 1636 cm^{-1}. And the typical absorption peaks at 1088 and 797 cm^{-1} were the stretching vibration of Si–O–Si and Si–O [28]. While the adsorption spectrums of IBU, MSN/IBU, CS/MSN/IBU all showed the typical absorption peaks of IBU, which were the stretching vibration of C=O at 1710 cm^{-1}, C=C vibration and C–H of phenyl ring at 1510 and 1420 cm^{-1}, respectively. In addition, both the adsorption spectrums of CS and CS/MSN/IBU had the absorption peaks of amide I at 1652 cm^{-1} and amide II at 1560 cm^{-1}. Carboxyl groups in IBU molecular and amino groups in CS molecular interacted together during the preparation process of CS/MSN/IBU, so the characteristic peak (1710 cm^{-1}) did not appear any more. All these results proved that the IBU loaded in MSN and the CS wrapped MSN/IBU successfully. Furthermore, the loading of IBU into the pores of MSN could be demonstrated through N_2 adsorption-desorption analysis, which the BET surface area reduced from 948.1 to 282.1 m^2/g and the pore volume reduced from 1.4 to 0.34 cm^3/g after IBU loading into MSN (Figure 6, Table 1).

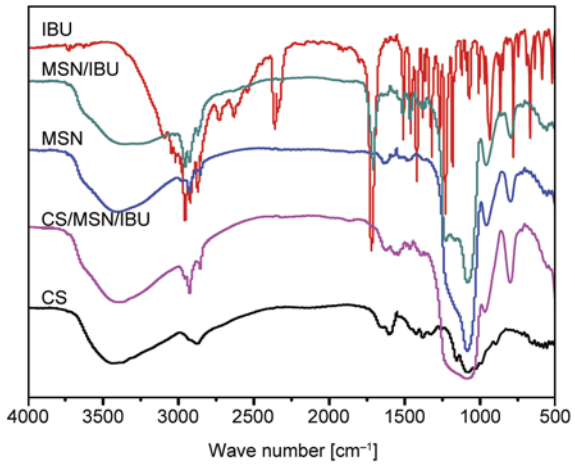

Figure 7. FTIR spectra of CS, IBU, MSN, MSN/IBU, CS/MSN/IBU

The loading efficiency of IBU into CS/MSN/IBU was dependent on the mass fraction of CS. In the meantime, the loading efficiency could be calculated by weighing method and ultra-violet photometer. The loading efficiency of MSN/IBU (LE_{MSN}) was deduced from Equation (1). The result was about 52.8%:

$$LE_{MSN} = \frac{m_1 - m_0}{m_1} \quad (1)$$

where m_0 and m_1 mean the weight of MSN before and after loading IBU into MSN, respectively.

In the process of CS wrapping MSN/IBU, there was IBU leaking out from the channels of MSN. The leaked IBU was measured by ultra-violet photometer (Figure 8). Equation (2) was used to calculate the loading efficiency of CS/MSN/IBU ($LE_{CS/MSN/IBU}$).

$$LE_{CS/MSN/IBU} = \frac{LE_{MSN} \cdot m_{MSN/IBU} - m_{lIBU}}{m_{CS/NSN/IBU}} \quad (2)$$

where $m_{MSN/IBU}$ and m_{lIBU} mean the weight of MSN/IBU and the weight of IBU leaked from the channels of MSN during the wrapping process.

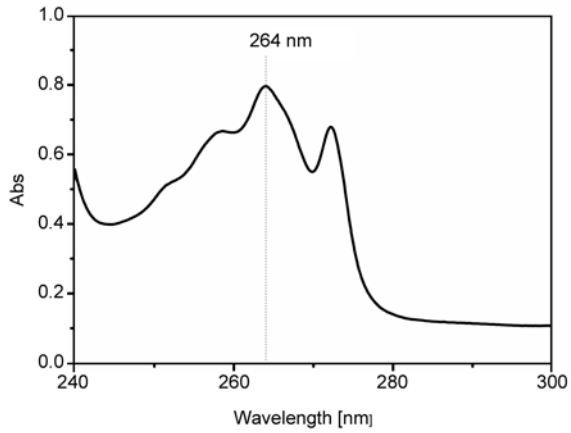

Figure 8. Ultraviolet-visible spectrum of the released IBU during the CS wrapping process

The loading efficiency of IBU into CS/MSN/IBU was 22.2, 28.9, 38.3% respectively when the mass fraction of CS was 0.2, 0.4, 0.6%.

3.2. Release behavior of IBU

The absorption peak at 264 nm (*Abs*) of IBU was used as signal to study the release of IBU from MSN/IBU and CS/MSN/IBU at 37°C. The experiments were carried out in PBS buffer solutions at two different pH values (7.4 and 6.8), which were chosen to mimic the normal body fluid and cancer cell. As shown in Figure 9, the total amount of IBU released from MSN/IBU was about 85 and 93% at pH 7.4 and 6.8, respectively. The amount of IBU released from CS/MSN/IBU at pH 7.4 was about 9.8% for 1 h and 13% for 12 h, but the release amount had little increase during the whole release process. It indicated that chitosan wrapped MSN/ IBU was stable for a long time and had lower side effect at physiological pH. While at pH 6.8, the release amount increased obviously (30% for 1 h and 53% for 12 h) and changed dramatically with the pH comparing with MSN/IBU. This phenomenon was caused by the change of molecular chain conformation of chitosan. Conformation of chitosan in solution is generally divided into spherical, random coil and rigid rod. One of the main factors influencing conformation is just the pH [32]. In acidic solution, the amino groups ($–NH_2$) on chitosan are protonated into $–NH^{3+}$, electrostatic repulsion becomes strong between chitosan molecules and the hydrogen bonding becomes less effective. In this case, the molecular chain of chitosan turns into a swollen polymeric matrix which is like loose random coil,

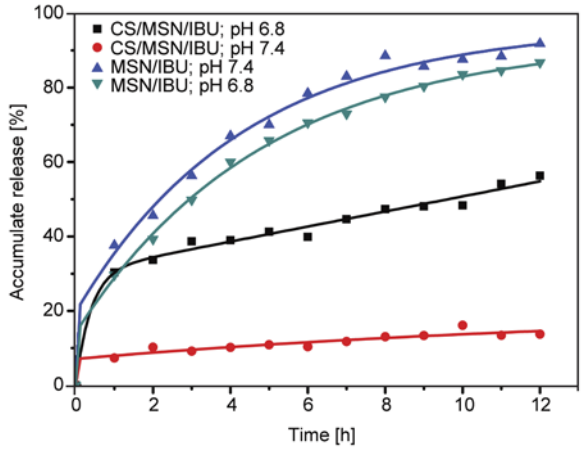

Figure 9. Release profiles of IBU from MSN/IBU and CS/MSN/IBU drug delivery systems

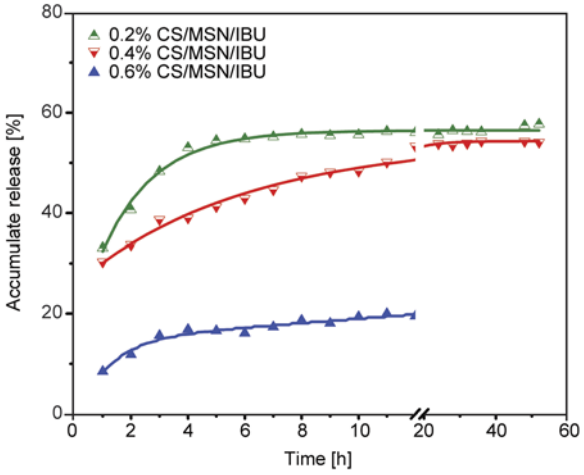

Figure 10. Release profiles of IBU from CS/MSN/IBU with different chitosan mass ratio (pH 6.8)

which has less influence on the release of IBU. While at pH 7.4, the amino groups don't carry charge and weaker electrostatic repulsion exists, so the molecular chain gets together as a shrinking mode [10]. This structure blocks the release of IBU to some extent. So the release amount at pH 6.8 was higher than at pH 7.4.

As shown in Figure 10, with the increase of mass fraction of chitosan, the accumulated release amount of CS/MSN/IBU decreased greatly from 56 to 19%. With the increase of mass fraction of CS, solution viscosity increased, which resulted in the structure of CS/MSN/IBU becoming more closely, crosslinking degree increasing and the swelling capacity reducing. Eventually the drug release rate decreased with the increase of mass fraction of CS.

As shown in Figure 11, MSNs were wrapped by chitosan and chitosan presented different states under different pH conditions because of protonation [10]. In this system, chitosan acted as a pH-responsive 'gatekeeper' ensuring more drug release at pH 6.8, which was probably due to the formation of hydrogen bond between the –OH on the MSN and the $–NH_2$ on the chitosan molecule.

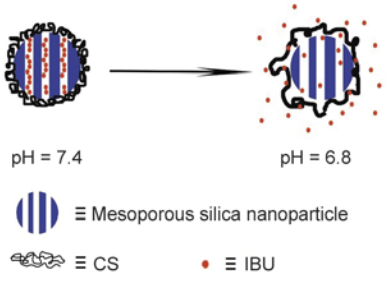

Figure 11. The pH-responsive drug delivery system

4. Conclusions

In summary, we have developed a simple approach to prepare an intelligent drug controlled delivery system by hydrogen bonding biopolymer as pH-responsive 'gatekeeper' and inorganic nanoparticles as drug carriers. The 'gatekeeper' is biodegradable and nontoxic, which could be directly applied to medical environment. MSNs with largest BET surface area and pore width were chosen as drug carriers which could load more drugs. Drug loading demonstrated that IBU loading increased with the increase of mass fraction of chitosan. *In vitro* release tests demonstrated that IBU release from MSNs was not pH-responsive, yet drug release from CS/MSN was pH-responsive with much higher release amount at pH 6.8 than pH 7.4.

Acknowledgements

The authors gratefully acknowledge the financial support of the Scientific Research key project of the Education Department Henan Province (14A430041, 14B430035 and 15A430043) and the Scientific and Technological Projects of Henan Province (142102210488).

References

[1] Deshpande A., Rhodes C., Shah N., Malick A.: Controlled-release drug delivery systems for prolonged gastric residence: An overview. Drug Development and Industrial Pharmacy, **22**, 531–539 (1996).
DOI: 10.3109/03639049609108355

[2] Gupta P., Vermani K., Garg S.: Hydrogels: From controlled release to pH-responsive drug delivery. Drug Discovery Today, **7**, 569–579 (2002).
DOI: 10.1016/S1359-6446(02)02255-9

[3] Freiberg S., Zhu X. X.: Polymer microspheres for controlled drug release. International Journal of Pharmaceutics, **282**, 1–18 (2004).
DOI: 10.1016/j.ijpharm.2004.04.013

[4] He Q., Shi J.: Mesoporous silica nanoparticle based nano drug delivery systems: Synthesis, controlled drug release and delivery, pharmacokinetics and biocompatibility. Journal of Materials Chemistry, **21**, 5845–5855 (2011).
DOI: 10.1039/C0JM03851B

[5] Mitra S., Gaur U., Ghosh P. C., Maitra A. N.: Tumour targeted delivery of encapsulated dextran–doxorubicin conjugate using chitosan nanoparticles as carrier. Journal of Controlled Release, **74**, 317–323 (2001).
DOI: 10.1016/S0168-3659(01)00342-X

[6] Chou J., Ito T., Bishop D., Otsuka M., Ben-Nissan B., Milthorpe B.: Controlled release of simvastatin from biomimetic β-TCP drug delivery system. PloS One, **8**, e54676/1–e54676/6 (2013).
DOI: 10.1371/journal.pone.0054676

[7] Cui L., Wang R., Ji X., Hu M., Wang B., Liu J.: Template-assisted synthesis of biodegradable and pH-responsive polymer capsules *via* RAFT polymerization for controlled drug release. Materials Chemistry and Physics, **148**, 87–95 (2014).
DOI: 10.1016/j.matchemphys.2014.07.016

[8] Cui L., Lin H., Guo W., Xiang D., Zhou D., Zhang T., Qu F.: A novel pH-responsive controlled release system based on mesoporous silica coated with hydroxyapatite. Journal of Sol-Gel Science and Technology, **72**, 106–113 (2014).
DOI: 10.1007/s10971-014-3419-0

[9] Wang H., Xu F., Li D., Liu X., Jin Q., Ji J.: Bioinspired phospholipid polymer prodrug as a pH-responsive drug delivery system for cancer therapy. Polymer Chemistry, **4**, 2004–2010 (2013).
DOI: 10.1039/C2PY20981K

[10] Popat A., Liu J., Lu G. Q. (M.), Qiao S. Z.: A pH-responsive drug delivery system based on chitosan coated mesoporous silica nanoparticles. Journal of Materials Chemistry, **22**, 11173–11178 (2012).
DOI: 10.1039/C2JM30501A

[11] Zhao Y., Vivero-Escoto J. L., Slowing I. I., Trewyn B. G., Lin V. S-Y.: Capped mesoporous silica nanoparticles as stimuli-responsive controlled release systems for intracellular drug/gene delivery. Expert Opinion on Drug Delivery, **7**, 1013–1029 (2010).
DOI: 10.1517/17425247.2010.498816

[12] Yuan L., Tang Q., Yang D., Zhang J. Z., Zhang F., Hu J.: Preparation of pH-responsive mesoporous silica nanoparticles and their application in controlled drug delivery. The Journal of Physical Chemistry C, **115**, 9926–9932 (2011).
DOI: 10.1021/jp201053d

[13] Du J-Z., Du X-J., Mao C-Q., Wang J.: Tailor-made dual pH-sensitive polymer–doxorubicin nanoparticles for efficient anticancer drug delivery. Journal of the American Chemical Society, **133**, 17560–17563 (2011).
DOI: 10.1021/ja207150n

[14] Agnihotri S. A., Mallikarjuna N. N., Aminabhavi T. M.: Recent advances on chitosan-based micro- and nanoparticles in drug delivery. Journal of Controlled Release, **100**, 5–28 (2004).
DOI: 10.1016/j.jconrel.2004.08.010

[15] Soppimath K. S., Aminabhavi T. M., Kulkarni A. R., Rudzinski W. E.: Biodegradable polymeric nanoparticles as drug delivery devices. Journal of Controlled Release, **70**, 1–20 (2001).
DOI: 10.1016/S0168-3659(00)00339-4

[16] Vandelli M., Rivasi F., Guerra P., Forni F., Arletti R.: Gelatin microspheres crosslinked with D,L-glyceraldehyde as a potential drug delivery system: Preparation, characterisation, *in vitro* and *in vivo* studies. International Journal of Pharmaceutics, **215**, 175–184 (2001).
DOI: 10.1016/S0378-5173(00)00681-5

[17] Coombes A. G. A., Rizzi S. C., Williamson M., Barralet J. E., Downes S., Wallace W. A.: Precipitation casting of polycaprolactone for applications in tissue engineering and drug delivery. Biomaterials, **25**, 315–325 (2004).
DOI: 10.1016/S0142-9612(03)00535-0

[18] Kumari A., Yadav S. K., Yadav S. C.: Biodegradable polymeric nanoparticles based drug delivery systems. Colloids and Surfaces B: Biointerfaces, **75**, 1–18 (2010).
DOI: 10.1016/j.colsurfb.2009.09.001

[19] Slowing I. I., Trewyn B. G., Giri S., Lin V. S-Y.: Mesoporous silica nanoparticles for drug delivery and biosensing applications. Advanced Functional Materials, **17**, 1225–1236 (2007).
DOI: 10.1002/adfm.200601191

[20] Chen F-H., Zhang L-M., Chen Q-T., Zhang Y., Zhang Z-J.: Synthesis of a novel magnetic drug delivery system composed of doxorubicin-conjugated Fe_3O_4 nanoparticle cores and a PEG-functionalized porous silica shell. Chemical Communications, **46**, 8633–8635 (2010).
DOI: 10.1039/c0cc02577a

[21] Liu Z., Tabakman S., Welsher K., Dai H.: Carbon nanotubes in biology and medicine: *In vitro* and *in vivo* detection, imaging and drug delivery. Nano Research, **2**, 85–120 (2009).
DOI: 10.1007/s12274-009-9009-8

[22] Gao X., Cui Y., Levenson R. M., Chung L. W. K., Nie S.: *In vivo* cancer targeting and imaging with semiconductor quantum dots. Nature Biotechnology, **22**, 969–976 (2004).
DOI: 10.1038/nbt994

[23] Singh N., Karambelkar A., Gu L., Lin K., Miller J. S., Chen C. S., Sailor M. J., Bhatia S. N.: Bioresponsive mesoporous silica nanoparticles for triggered drug release. Journal of the American Chemical Society, **133**, 19582–19585 (2011).
DOI: 10.1021/ja206998x

[24] Slowing I. I., Vivero-Escoto J. L., Trewyn B. G., Lin V. S-Y.: Mesoporous silica nanoparticles: Structural design and applications. Journal of Materials Chemistry, **20**, 7924–7937 (2010).
DOI: 10.1039/c0jm00554a

[25] Mitoraj D., Kisch H.: The nature of nitrogen–modified titanium dioxide photocatalysts active in visible light. Angewandte Chemie International Edition, **47**, 9975–9978 (2008).
DOI: 10.1002/anie.200800304

[26] Croissant J., Cattoën X., Man M. W. C., Gallud A., Raehm L., Trens P., Maynadier M., Durand J-O.: Biodegradable ethylene-bis(propyl)disulfide-based periodic mesoporous organosilica nanorods and nanospheres for efficient in-vitro drug delivery. Advanced Materials, **26**, 6174–6180 (2014).
DOI: 10.1002/adma.201401931

[27] Chang J-S., Chang K. L. B., Hwang D-F., Kong Z-L.: *In vitro* cytotoxicitiy of silica nanoparticles at high concentrations strongly depends on the metabolic activity type of the cell line. Environmental Science and Technology, **41**, 2064–2068 (2007).
DOI: 10.1021/es062347t

[28] Pourjavadi A., Tehrani Z. M.: Mesoporous silica nanoparticles (MCM-41) coated PEGylated chitosan as a pH-responsive nanocarrier for triggered release of erythromycin. International Journal of Polymeric Materials and Polymeric Biomaterials, **63**, 692–697 (2014).
DOI: 10.1080/00914037.2013.862534

[29] Li L-L., Zhang R., Yin L., Zheng K., Qin W., Selvin P. R., Lu Y.: Biomimetic surface engineering of lanthanide-doped upconversion nanoparticles as versatile bioprobes. Angewandte Chemie, **124**, 6225–6229 (2012).
DOI: 10.1002/ange.201109156

[30] Liu Z., Jiao Y., Wang Y., Zhou C., Zhang Z.: Polysaccharides-based nanoparticles as drug delivery systems. Advanced Drug Delivery Reviews, **60**, 1650–1662 (2008).
DOI: 10.1016/j.addr.2008.09.001

[31] Slowing I. I., Trewyn B. G., Lin V. S-Y.: Mesoporous silica nanoparticles for intracellular delivery of membrane-impermeable proteins. Journal of the American Chemical Society, **129**, 8845–8849 (2007).
DOI: 10.1021/ja0719780

[32] Sorlier P., Viton C., Domard A.: Relation between solution properties and degree of acetylation of chitosan: Role of aging. Biomacromolecules, **3**, 1336–1342 (2002).
DOI: 10.1021/bm0256146

eXPRESS Polymer Letters Vol.9, No.12 (2015) 1076–1086
Available online at www.expresspolymlett.com
DOI: 10.3144/expresspolymlett.2015.97

Devulcanization of styrene butadiene rubber by microwave energy: Effect of the presence of ionic liquid

S. Seghar[1,4], N. Aït Hocine[2], V. Mittal[3], S. Azem[4], F. Al-Zohbi[5], B. Schmaltz[5], N. Poirot[6]*

[1]LMR, CERMEL, Université François-Rabelais de Tours, 37300 Joué-Lès-Tours, France
[2]LMR, INSA Centre Val de Loire, 3 rue de la Chocolaterie, BP 3410, 41034 Blois, France
[3]Department of Chemical Engineering, The Petroleum Institute, Abu Dhabi, UAE
[4]LEC2M, Université Mouloud Mammeri, BP 17, Tizi-Ouzou 15000, Algérie
[5]PCM2E (E.A. 6299), Université François-Rabelais de Tours, Bâtiment J-Parc de Grandmont, 37200 Tours, France
[6]GREMAN, IUT de Blois, 15 rue de la Chocolaterie, 41000 Blois, France

Received 25 April 2015; accepted in revised form 15 July 2015

Abstract. In this study, styrene butadiene rubber (SBR) was devulcanized using microwave irradiation. In particular, effect of ionic liquid (IL), pyrrolidinium hydrogen sulfate [Pyrr][HSO_4], on the devulcanization performance was studied. It was observed that the evolution of the temperature reached by rubber powder exposed to microwave irradiation for different energy values was favored by the presence of ionic liquid [Pyrr][HSO_4] significantly over the whole range of the microwave energy values. Beyond the threshold point of 220 Wh/kg, the soluble fraction after devulcanization sharply increased with increasing devulcanization microwave energy. For the powder mixed with [Pyrr][HSO_4], the increase was more significant. Furthermore, the crosslink density was observed to decrease slowly with the microwave energy up to 220 Wh/kg, beyond which the crosslink density decreased significantly for the rubber impregnated with IL. For the rubber with IL, significant and continuous increase in T_g with microwave energy values was observed in comparison with the SBR where no change in transition temperature was observed. Mechanical shearing of rubber gums in the two-roll mill favored the devulcanization process, which indicated that the combination of mechanical loading with microwave energy and IL is an efficient procedure allowing an optimal devulcanization of rubbers.

Keywords: *rubber, recycling, devulcanization, microwaves, ionic liquid*

1. Introduction

Increase in the demand of rubber in recent years, particularly in tire industry, has resulted in not only increased prices of raw materials, but also accumulation of harmful wastes. Garbage dumps of used tires represent flammable sites and generate proliferation of various insects and rodents carrying diseases. Moreover, slow degradation of rubber residues results in severe environmental pollution. Recycling such waste safely is therefore a big challenge for industrialists and academic researchers. Devulcanization of waste rubber products is one of such process which leads to recycling the waste tires as polymeric materials, thus, also decreasing the extent of environmental risks.

Passenger car tire material is a blend of different polymers with the main component being styrene-butadiene rubber (SBR). Each polymer contributing to the tire formulation has its own specific degradation and devulcanization characteristics. As a result, a number of physical and chemical methods have been developed to break the crosslink bonds or induce active groups on the surface of ground rubber. These methods are based on mechanical energy [1], ultra-

*Corresponding author, e-mail: nourredine.aithocine@insa-cvl.fr

sound [2, 3], microwave irradiation [4, 5], chemical desulfurization reagents [6, 7] or biotechnological methods [8]. Depending on their efficacy, they lead to the devulcanization or the reclaiming process. Devulcanization targets the sulfuric crosslinks in the vulcanized rubber and thus carbon-sulfur (C–S) and sulfur-sulfur (S–S) bonds are selectively cleaved, while reclaiming is usually accompanied with considerable scission along the polymeric chains resulting in lower molecular mass fractions [9].

Microwave devulcanization process was proposed by Goodyear in 1978 and successfully implemented by Novotny *et al*. [4]. It consists of exposing the waste rubber, for a short time, to controlled microwave irradiation. However, only sulfur-vulcanized rubber containing polar groups or components can be heated and thus be devulcanized with this technique.

Microwave heating is based on the interaction of the oscillating electrical field of microwaves with the molecular dipoles and/or charged ions present in the sample. Microwave irradiation triggers heating by three main mechanisms: dipolar polarization, ionic conduction and interfacial polarization. While the dipolar polarization mechanism (dielectric heating) explains the heating phenomena of dipoles, the ionic conduction mechanism explains the heating in samples with free ions or ionic species. The interfacial polarization (also called the Maxwell-Wagner effect) mechanism describes the heating in non-homogeneous systems created by the suspension of conducting particles in a non-conducting medium. Fix [10] extensively studied the efficiency of the microwave devulcanization process and such operation was concluded to be feasible.

Other studies by Goodyear society on the devulcanization of EPDM rubber by microwaves showed that properties of the treated material were not considerably altered [4, 10]. EPDM being a non-polar rubber, microwave energy was transferred in the whole volume of the material via carbon black filler initially introduced as reinforcing particles.

Bani *et al*. [11] also performed similar studies and observed that the microwave devulcanization process was effective only beyond the heating temperature of 300°C.

Landini *et al*. [12] used a microwave technique to devulcanize bromobutyle (BIIR), and optimal power and time of treatment were identified as factors leading to the highest devulcanization proportion. Similarly, Scagliusi *et al*. [13] devulcanized chloroprene rubber, followed by re-vulcanization. The authors observed that properties of the recycled material changed with microwave irradiation time, as compared to the original material. Hardness and fracture resistance were observed to decrease, whereas rupture strain increased. Vega *et al*. [5] also combined microwave irradiation with the effect of diphenyl sulfide (DPDS), chemical agent supposed to improve devulcanization process. The authors highlighted the beneficial effects of DPDS on the efficiency of microwave devulcanization process. In another study, Hong *et al*. [14] also compared devulcanization performance of microwave and ultrasonic procedures and concluded that microwave technique is better than ultrasonic method.

To improve devulcanization efficiency and reduce treatment energy, promising new approach consists of impregnation of the waste rubber with solvent and then heat treating the impregnated material with microwave radiation. In fact, impregnation of the waste rubber could promote the heat rise when exposed to microwave radiation.

Ionic liquids (ILs), considered as an alternative to conventional organic solvents, are of interest in a variety of technological processes. For instance, they were recently used to improve the degree of dispersion of a nanosized ZnO and Silica in NBR matrix [15]. The desire for green solvents for industrial processes is partially responsible of this keen interest. ILs are (molten) salts composed of large variety of organic cations and organic/inorganic anions [16]. They present several interesting properties: excellent solvent for various organic/inorganic materials, negligible vapor pressure, high thermal and chemical stability, non-flammability, high ionic conductivity, low viscosity and large electrochemical capacitance [16, 17]. The ionic conduction mechanism is the most important effect in the heating of ILs by microwave; it increases their dielectric loss factor.

In this study, styrene butadiene rubber (SBR) was devulcanized using microwave irradiation and the performance of the devulcanization treatment was analyzed in term of crosslink scission. Effect of [Pyrr][HSO_4], on the devulcanization performance was studied, which represents one of the originalities of this study.

2. Experimental

2.1. Materials

The analyzed material in this study was a styrene-butadiene rubber (SBR) obtained by mixing virgin SBR and additive components in an open two roll mill, at room temperature. Parts per hundred rubber [phr] of the whole formulation are reported in Table 1.

The material studied in this work is a mixture of two grades of SBR: 50 phr of SBR1500 with a styrene content of 23.5% and 50 phr of SBR1900 with a styrene content of 75%. We deliberately chose such a mixture in order to limit the amount of butadiene, which reduces the number of carbon-carbon double bonds (C=C) leading to a loosely cross-linked network. Reduction of C=C bonds also limits the influence of the external environment (oxygen, ozone …) on the rubber structure during processing and storage. A loosely cross-linked network facilitates the penetration of solvent through the rubber and therefore improves the sensitivity of methods which allow evaluation of cross-link density and soluble fraction.

Differential scanning calorimetry (DSC) tests were conducted in a nitrogen environment on un-vulcanized and vulcanized SBR, using Netzsch equipment (Netzsch maia 200F, Selb, Germany). Samples weighing about 10 mg were heated from –100°C up to 280°C at a rate of 10°C/min.

After mixing operation, the rubber was vulcanized at 170°C for 7 min, under compression in a hydraulic molding press (Agila, Kortrijk-Bissegem, Belgium). Before the devulcanization treatment, the rubber was grounded, at ambient temperature, with a disc mill PQ500 (Phenix Machinery, Sancheville 28800, France) containing a 4 mm screen. The obtained ground SBR was passed in a succession of different mesh sieve, which allowed evaluating the particle size distribution of the ground rubber. It appeared that ~96% of the SBR powder has a size ranging from 1 to 4 mm and ~4% has a size lower than 1 mm. The SBR powder of size ranging from 1 to 4 mm has used in this study.

Table 1. Components used for the rubber formulation

Components	Quantity [phr]
Styrene butadiene rubber (SBR 1502)	50
Styrene butadiene rubber (SS260)	50
Carbon black (HAF N330)	60
Naphtenic oil	25
Paraffinic oil	1.2
Rubber antioxidant: N-Isopropyl-N′-phenyl-p-phenylene-diamine (IPPD)	1.25
Rubber antioxidant: N-(1,3-Dimethylbutyl)-N′-phenyl-p-phenylenediamine (6PPD)	1.25
Rubber antioxidant: 2,2,4-trimethyl-1,2-dihydro-quinoline (TMQ)	1
Antiozonant agents (Paraffinic wax)	2
Activator: zinc oxide (ZnO)	5
Dispersing agent and accelerator activator: Stearic acid	2
Vulcanization agent: sulfur (S)	1.5
Accelerator: N-cyclohexyl-2-benzothiazole sulphenamide (CBS)	1.5

2.2. Microwave devulcanization procedure

A commercial microwave oven (Galanz, Foshan, China) was adapted to be used for devulcanization treatment of SBR ground rubber in laboratory. Stirring system and infrared temperature sensor (SparkFun IR Thermometer Evaluation Board-MLX90614, Lextronic, France) were additionally installed in the oven and the process was controlled by a computer. A mass M of ~50 g of ground SBR placed in a 250 mL beaker was exposed to microwave irradiations under magnetron power P of 656 watts, at different time values t. The stirring speed was 40 rpm. The corresponding microwave specific energy E was evaluated from Equation (1):

$$E = \frac{P \cdot t}{M} \tag{1}$$

In order to improve the efficiency of the rubber microwave processing, the same procedure was repeated, but by mixing priory the SBR powder in 10 wt% of ionic liquid pyrrolidinium hydrogen sulfate [Pyrr][HSO_4], in a crystallizer during 10 minutes. The mixture was left to stand for 1 hour at least, prior to microwave treatment. No specific other treatment was applied for IL and SBR powder before microwave treatment. Properties of this IL are summarized in [18]. It was used because it is a good heat vector and it readily absorbs microwave energy, which could quickly increase the temperature of the mixture during the devulcanization treatment. Moreover, it does not evaporate and does not degrade below 200°C. Furthermore, this IL is a green solvent with low vapor pressure, high chemical and thermal stability and it is a non-flammable liquid. Thus, the goal of using such IL was to favor the transfer of the microwave energy until the core of the material granulates and to obtain uniform distribution of the temperature through the volume of these particles.

Table 2. Coding and devulcanization conditions

SBR without [Pyrr][HSO_4]	SBR with 10 wt% [Pyrr][HSO_4]	Magnetron power [W]	Treatment time [s]	Energy [Wh/kg]
SBR	SBR-P	0	0	0
SBR-110	SBR-P-110	656	30	110
SBR-220	SBR-P-220	656	60	220
SBR-330	SBR-P-330	656	90	330
SBR-440	SBR-P-440	656	120	440

It was observed that the ground rubber ignited when it was exposed for microwave energy inducing temperature higher than 210°C. This is probably due to the inflammation of the naphtenic oil (CIRCOSOL 4240) and paraffinic process oil (FLEXON 876) used as plasticizers in the rubber mixture. In fact, the flash points of these oils are 221 and 246°C, respectively. Thus, the magnetron power value of 656 watts and the maximal time of treatment of 120 s were selected such as the induced maximal temperature was lower than ~210°C. The treatment conditions are summarized in Table 2. The SBR soaked in [Pyrr][HSO_4] is denoted SBR-P in this paper.

The heat capacity C_p of the [Pyrr][HSO_4] was determined by the DSC approach. It was achieved by heating a small quantity of IL from ambient temperature to 200°C and the heat flow was recorded during the test. Thermo-gravimetric analyses (TGA) were also performed on [Pyrr][HSO_4] using a Perkin-Elmer Diamond TG/DTA (Waltham, Massachusetts, U.S.A). A small quantity of the liquid was heated from room temperature up to 550°C, at a rate of 10°C/min and under a nitrogen atmosphere. The mass variation of the liquid was measured as a function of temperature.

2.3. Evaluation of the devulcanization

Right after devulcanization treatment, the SBR was washed with distilled water then dried in a vacuum oven (Heraeus Vacuum oven VT6025, Hanau, Germany) at 30°C for 24 h. Soluble fraction of ground SBR and devulcanized ground SBR were then determined by extraction in a Soxhlet extractor for 24 h in acetone (Sigma-Aldrich, Steinheim, Germany) to remove low-molecular weight polar substances like remains of accelerators and curatives. This operation was immediately followed by an extraction for 72 h in toluene (Sigma-Aldrich, Steinheim, Germany) to remove the non-polar components such as oil and non-crosslinked polymer residues or soluble polymer chains released from the network by the devulcanization process. The soluble fraction S of the material was evaluated using Equation (2):

$$S\,[\,\%\,] = \frac{M_i - M_f}{M_i} \cdot 100 \tag{2}$$

where M_i and M_f are the SBR rubber weight before and after extraction operation respectively.

After swelling in cyclohexane (Sigma-Aldrich, Steinheim, Germany) at room temperature for 72 h, the soluble fraction was weighed and then dried in a vacuum oven at 50°C for 24 h. The apparent crosslink density ν_c was determined according to Equation (3) [19]:

$$\nu_c = \frac{\nu_r + \chi\nu_r^2 + \ln(1 - \nu_r)}{\nu_s(0.5\nu_r - \nu_r^{1/3})} \tag{3}$$

with:

$$\nu_r = \frac{m_r}{m_r + m_s\left(\frac{\rho_r}{\rho_s}\right)} \tag{4}$$

In Equations (3) and (4), ν_r is the volume fraction of the polymer in the swollen specimen, ν_s is the molar volume of the solvent, χ is the Flory-Huggins polymer solvent interaction parameter (equal to 0.489 for SBR-Cyclohexane (ASTM-D6814-02)), m_r is the mass of the dry rubber, m_s is the mass of the solvent absorbed by the rubber, ρ_r and ρ_s are the densities of the dry rubber and solvent respectively.

The percent devulcanization was calculated according to the standard ASTM test method D6814-02, using Equation (5):

$$Devulcanization\,[\,\%\,] = \left(1 - \frac{\nu_f}{\nu_i}\right) \cdot 100 \tag{5}$$

where ν_i and ν_f are the crosslink densities of the samples before and after devulcanization, respectively.

The devulcanization process theoretically results in crosslink scission. However, actual route also causes breaking of principal polymer chains. When this phenomenon is considerable, it induces the loss of the recyclate properties. To further understand the devulcanization mechanism, theoretical relationship developed by Horikx [20] was used, which correlates the rubber soluble fraction of the devulcanizates and the relative decrease in crosslink density. When only main-chain scission takes place, the relative decrease in the apparent crosslink density is given by Equation (6):

$$1 - \frac{\nu_f}{\nu_i} = 1 - \left[\frac{(1 - \sqrt{S_f})^2}{(1 - \sqrt{S_i})^2}\right] \quad (6)$$

where S_i and S_f are the soluble fraction of the untreated vulcanizate and reclaimed vulcanizate respectively, ν_i is the crosslink density of the untreated vulcanizate and ν_f is the crosslink density of the reclaimed vulcanizate.

For pure crosslink scission, the soluble fraction is related to the relative decrease in crosslink density by Equation (7):

$$1 - \frac{\nu_f}{\nu_i} = 1 - \left[\frac{\gamma_f(1 - \sqrt{S_f})^2}{\gamma_i(1 - \sqrt{S_i})^2}\right] \quad (7)$$

where γ_i and γ_f are the average numbers of crosslinked units per chain before and after treatment respectively. These parameters were determined from the relation between soluble fraction S and the number of crosslinked units per chain γ, given by Charlesby [21, 22] under the following form Equation (8):

$$S = \frac{1}{(1 + \gamma - \gamma s)} \quad (8)$$

After applying microwave devulcanization process on SBR soaked in [Pyrr][HSO_4] and no-soaked SBR, glass transition temperature T_g of these materials was determined following the same experimental protocol described above. T_g could be a pertinent indicator of microstructure change which may be caused by, among others, the vulcanization or devulcanization process.

Finally, the Mooney viscosity ML (1+4)·100°C was measured using a Mooney viscometer from Gibitre Instruments (Bergamo, Italy).

All specimens were continuously stored under controlled temperature of 4°C.

3. Results and discussion

Figure 1 shows the heat flow recorded during heating, as a function of temperature, for un-vulcanized and vulcanized SBR. It exhibited an endothermic transition characteristic of glass transition temperature, T_g, estimated at –48°C for the raw SBR and at -43°C for the vulcanized SBR. The increase of T_g from –48 to –43°C confirmed the successful vulcanization of the studied material. In fact, the vulcanization treatment led to the formation of 3D network, thereby reducing macromolecular mobility resulting in augmentation of T_g. Moreover, an exothermic peak beginning at ~160°C and reaching its maximum at ~210°C, was observed. This peak corresponds to the temperature of the SBR vulcanization reaction. Such a transition was not present in the vulcanized rubber thermogram, thus, further proving that the vulcanization of the material was entirely accomplished.

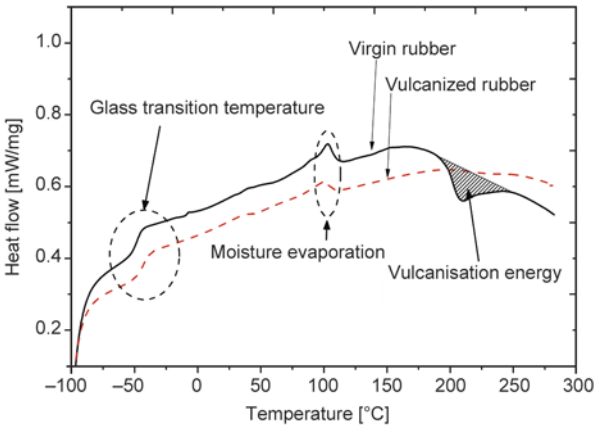

Figure 1. DSC curves of the SBR before and after vulcanization

The heat capacity C_{pe} of [Pyrr][HSO_4] is reported in Figure 2 as a function of temperature. This heat capacity is evaluated from Equation (9):

$$C_{pe} = \frac{m_r}{m_e} \cdot \frac{\varphi_e - \varphi_0}{\varphi_r - \varphi_0} \cdot C_{pr} \quad (9)$$

where m_r and m_e are masses of aluminum oxide and ionic liquid [Pyrr][HSO_4] respectively ; φ_0, φ_r and φ_e are heat flows measured for empty crucible, aluminum oxide and IL respectively; C_{pr} represent mass calorific capacities of aluminum oxide. The heat capacity of distilled water was also measured and showed in Figure 2. It can be seen that C_p of [Pyrr][HSO_4] was constant up to 120°C and was

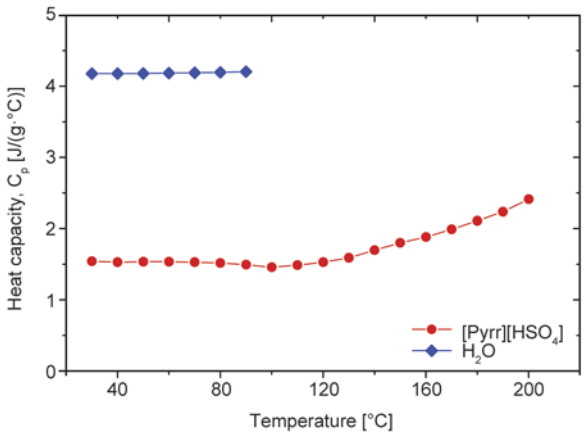

Figure 2. Heat capacity of [Pyrr][HSO_4] and water as a function of temperature

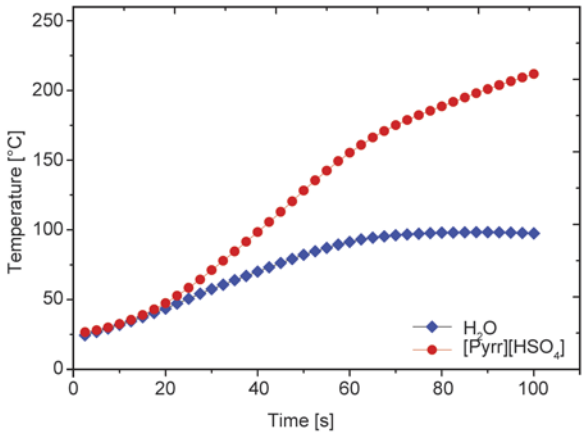

Figure 3. Temperatures of water and [Pyrr][HSO_4] as a function of microwave irradiation time

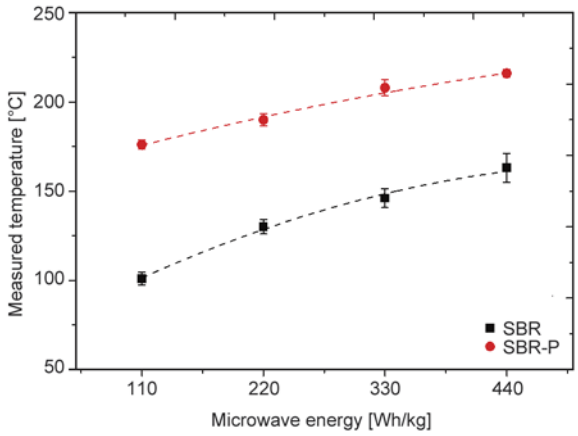

Figure 5. Temperature of ground rubber with and without ionic liquid as a function of microwave energy

three times smaller than that of distilled water, thus, proving a good heat transfer capacity of this IL.

Figure 3 presents temperature evolutions of [Pyrr][HSO_4] and distilled water as a function of the time, recorded under microwave irradiation at magnetron power of 656 W. It was evident that the temperature of the IL increased more quickly than water to become two times greater after 100 s of exposition. Moreover, contrary to the temperature of the water that stabilized at 100°C beyond 80 s, the temperature of the IL increased continuously over the range of analysis time. These results further confirmed the relative high ability of [Pyrr][HSO_4] to convert microwave energy in heat, compared to water.

Figure 4 shows the weight loss of [Pyrr][HSO_4] as a function of temperature, obtained by TGA measurements. The curve exhibited a first plateau followed by a sudden decrease corresponding to its thermal degradation. The onset degradation temperature, T_{onset}, was evaluated by the method of tangent and

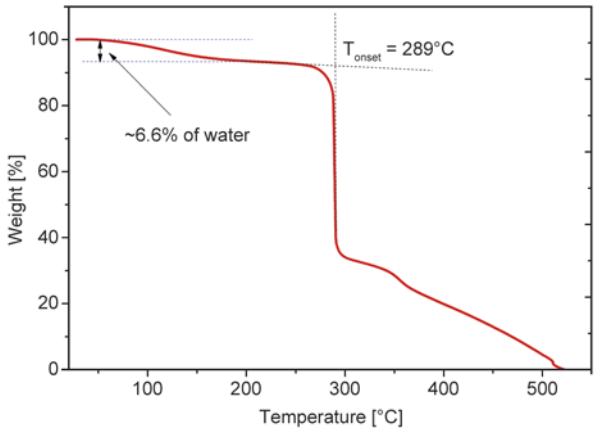

Figure 4. TGA curve of [Pyrr][HSO_4]

was found to be ~289°C, as shown in Figure 4. To avoid the degradation of [Pyrr][HSO_4] during the devulcanization treatment, this temperature value should not be exceeded when the SBR rubber combined with [Pyrr][HSO_4] is treated by microwave irradiation as described above.

Figure 5 shows the evolution of the temperature reached by rubber powder exposed to microwave irradiation, for different energy values. The presence of ionic liquid [Pyrr][HSO_4] significantly favored the material heating over the whole range of the considered microwave energy values. In fact, the temperature reached by the SBR soaked in [Pyrr][HSO_4] was 1.70 times greater than the dry SBR. This result suggested that [Pyrr][HSO_4] could play energy vector role during the microwave devulcanization process.

Figure 6 shows evolutions of the soluble fractions (Equation (2)) of treated rubber as a function of microwave energy. The soluble fraction indicates the extent to which the rubber network is broken. From the Figure 6, it was evident that microwave treatment of sulfur-cured SBR exhibited a soluble fraction similar up to 220 Wh/kg, irrespective of IL soaking. This indicated that up to this treatment energy value, rubber network was still intact. Beyond this threshold point, the soluble fraction sharply increased with increasing devulcanization microwave energy i.e. by increasing the treatment temperature. The increase was more significant for the powder mixed with [Pyrr][HSO_4], further proving the positive role played by the IL in the microwave devulcanization process of rubbers.

Figure 7 depicts crosslink densities (Equation (3)) of SBR and SBR-P samples, as a function of micro-

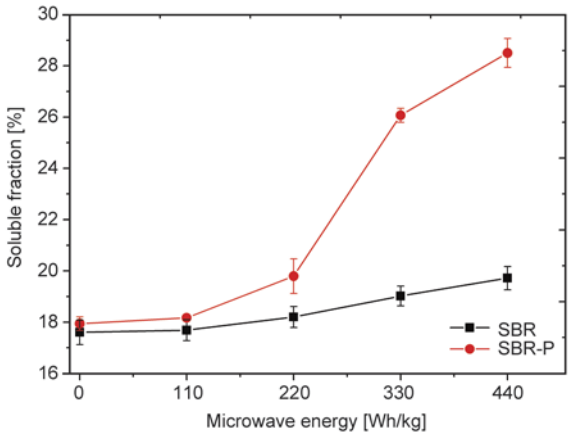

Figure 6. Soluble fraction of ground rubber with and without ionic liquid as a function of microwave energy

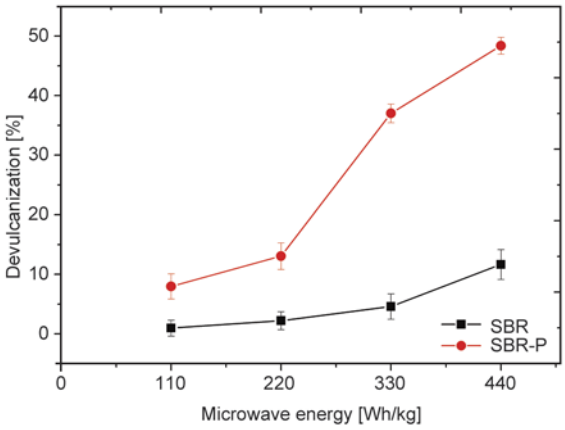

Figure 8. Devulcanization of ground rubber with and without ionic liquid as a function of microwave energy

wave energy. The crosslink density decreased slightly and slowly with the microwave energy up to 220 Wh/kg, critical value beyond which the crosslink density decreased significantly for the SBR-P rubber. These results agreed well with the findings shown in Figure 6 and confirmed that the liquid ionic [Pyrr][HSO_4] favored the microwave devulcanization process. Figure 8 also shows the devulcanization proportions (Equation (5)) of the SBR and SBR-P, as a function of microwave energy. Curves showed the same trends as soluble fractions (Figure 6), confirming existence of a relationship between the two quantities (Equations (2) and (5)). Devulcanization fractions are also represented in Figure 9 as a function of average temperature generated in rubber powder, measured with infrared sensor during microwave irradiation. It should be noticed that rubber powder was mixed with an agitator during the devulcanization treatment. The experimental data of both SBR and SBR-P were fitted by power laws. It was evident that for a given microwave energy value, average temperature reached by SBR-P was much higher than the one reached by dry SBR. Also, the devulcanization process seemed to be efficient above a temperature threshold of ~200°C, in agreement with the results found by Saiwari *et al.* [23] in the devulcanization of SBR in an internal mixer with addition of treated distillate aromatic extract (TDAE) oil and diphenyldisulfide (DPDS). To further analyze the devulcanization of rubbers by microwave process, the distribution of the treatment temperature was recorded with an infrared camera FLIR JADE-MWIR, in both SBR and SBR-P, after subjecting them to microwave energy. The obtained micrographs are shown in Figure 10, as an example for treatment energy of 40 Wh/kg. The temperature was observed to be more homogeneous and better diffused in the SBR-P powder than in the dry SBR powder. This result proved that microwave irradiation produced efficient internal heating by direct coupling of microwave energy with the IL, resulting in higher average temperature and homo-

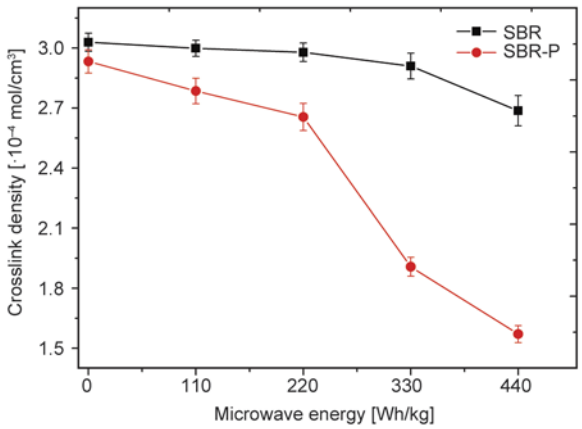

Figure 7. Crosslink density of ground rubber with and without ionic liquid as a function of microwave energy

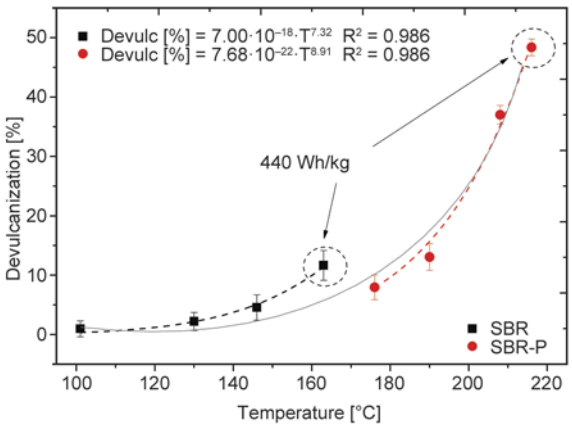

Figure 9. Devulcanization of ground rubber with and without ionic liquid as a function of temperature reached during microwave treatment

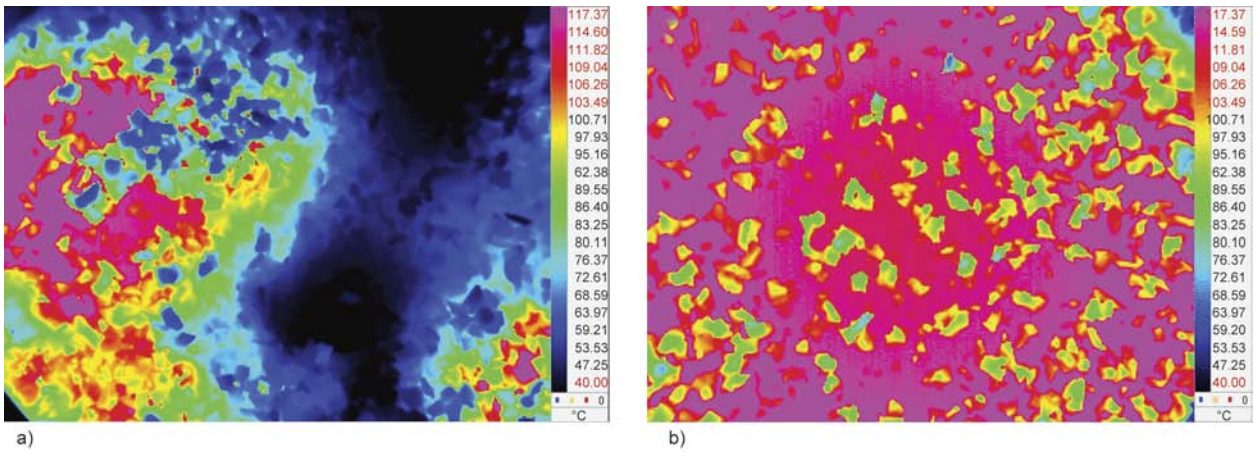

Figure 10. Temperature of the ground rubber (a) without ionic liquid and (b) with ionic liquid, measured with a thermal camera

geneous heating throughout the treated material, which can partially explain the lower crosslinking density of the SBR-P shown in Figure 7.

Figure 11a and 11b show the experimentally determined soluble fractions of SBR and SBR-P respectively, as a function of devulcanization fractions evaluated using Equation (5), for different microwave energy values. Theoretical curves of Horikx given by Equations (6) and (7) are also plotted in Figure 11. The experimental data fitted well with the Horikx's curve corresponding to the crosslink scission (Equation (7)), suggesting that devulcanization process occurred in all microwave treated materials by rather selective breakage of crosslinks.

However, magnitude of this devulcanization was higher as the microwave energy was increased and when the SBR was imbibed in IL. An increase in the microwave energy resulted in a shift of the data point to the right hand region of the graph which indicated decrease of crosslink density. The shift phenomenon was even more pronounced for the ground rubber mixed with IL. For instance, for the same microwave energy of 440 Wh/kg, apparent devulcanization in SBR-P reached ~50%, which was four times greater than dry SBR.

Figure 12 shows the evolution of T_g for the SBR and SBR-P, as a function of microwave energy. The T_g of the SBR remained almost constant in the whole range of the applied microwave energy values, suggesting that there was no significant change in the material microstructure in this range. However, a significant and continuous increase in T_g with microwave energy values was observed for SBR-P, indicating that the structure changed as the microwave energy was enhanced. The increase of the T_g has also been reported by others authors for devulcanization of sulfur vulcanized rubber by ultrasound [24]. This change in T_g was attributed to the formation of cyclic sulfur structures in the polymer chains. Such a structure limits the mobility of the chains, increasing the T_g of the elastomer. For microwave devulcanization of ground tire rubber [25], this dif-

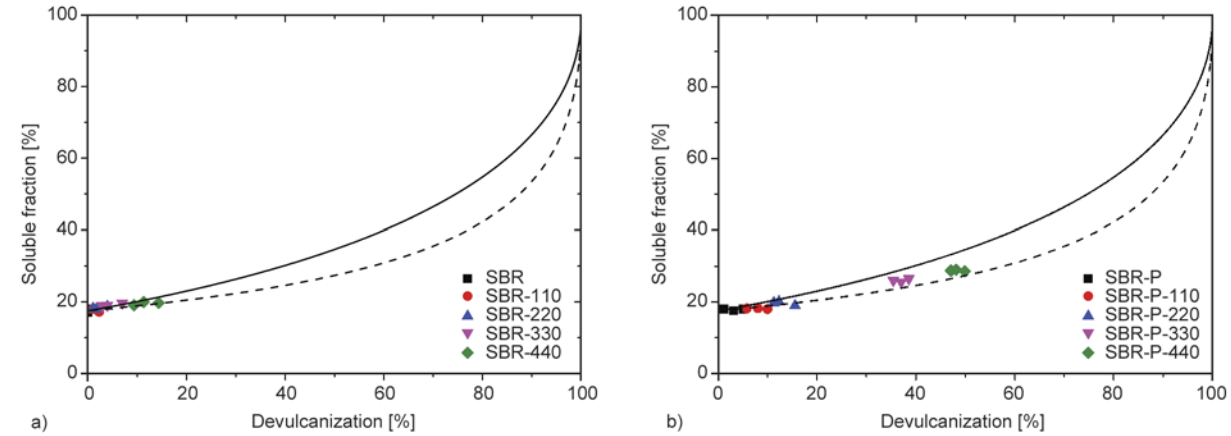

Figure 11. Horikx diagram for ground rubber (a) without ionic liquid and (b) with ionic liquid

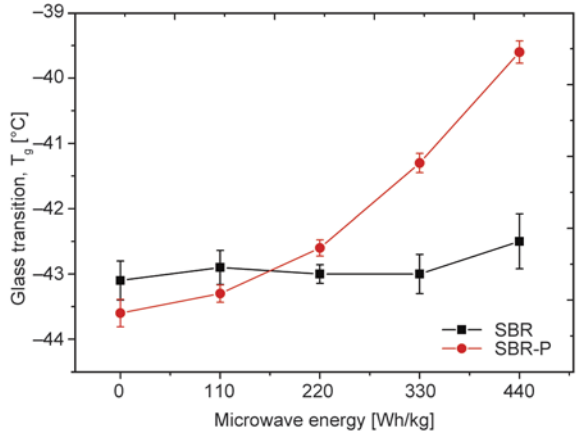

Figure 12. Glass transition temperatures of ground rubber with and without ionic liquid as a function of microwave energy

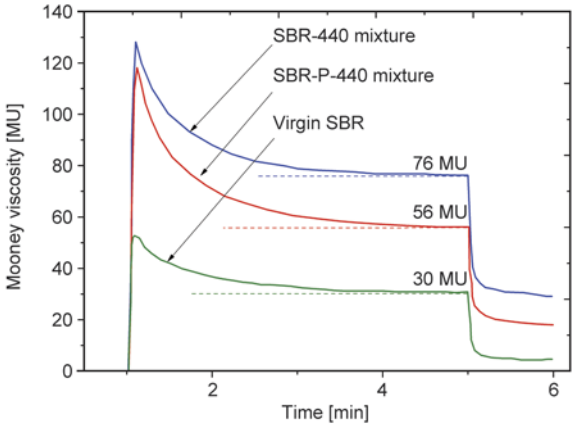

Figure 14. Mooney viscosity ML (1+4) 100°C for unvulcanized raw rubber and different recycled rubbers (MU is Mooney unit of viscosity: 1 MU = 0.083 N·m)

ference in the T_g values was also attributed to the higher carbon black content of the devulcanized samples. On the other hand, the volatilization at high temperature (above 200°C) of the extender oil which works as a plasticizer for the rubber molecules also tends to diminish the molecular mobility of the rubber, increasing its T_g.

Gums were generated from the devulcanized SBR and SBR-P materials, treated with microwave energy of 440 Wh/kg. To do this, a laboratory two-roll mill was used with the friction ratio of 1.3, at temperature of 50°C and mixing time of 10 min for each blend.

The soluble fractions and the devulcanization proportions of the obtained mixtures are reported in Horikx diagram in Figure 13. Data of microwave treated SBR powder are also plotted in this figure. It can be observed that experimental points of mixtures shifted significantly to the right region of the Figure 13, while remaining well fitted by theoretical curve corresponding to the main-chain scission (Equation (7)). These points moved from 13 to 38% and from 50 to 65% for SBR and SBR-P respectively. This result indicated that the mechanical shearing of rubber, involved herein into the two-roll mill, favored the devulcanization process, suggesting that combining mechanical loading with microwave energy and IL could be a most profitable procedure allowing an optimal devulcanization of rubbers.

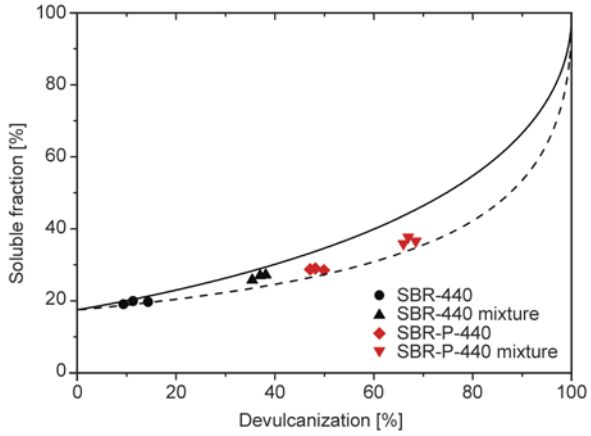

Figure 13. Horikx diagram for SBR powder and SBR mixture

Figure 14 shows the Mooney viscosity and Mooney relaxation of virgin unvulcanized rubber and reclaimed rubber obtained after ground rubber mixing. The Mooney viscosity of the rubber gives an indication of the relative devulcanization degree. Indeed, more is the degree of devulcanization, lower is the Mooney viscosity [26]. Thus, curves in Figure 14 confirmed the earlier results. The specimen generated from the ground rubber previously treated by microwave in the presence of IL exhibited Mooney viscosity close to that of the virgin rubber, proving high devulcanization of this specimen.

4. Conclusions

Devulcanization styrene butadiene rubber (SBR) by microwave irradiations has been studied. The effect of IL (pyrrolidinium hydrogen sulfate [Pyrr][HSO_4]) on this devulcanization was particularly analyzed. High ability of this IL to convert microwave energy in heat has been proved. The increase in the soluble fraction with increasing microwave energy was also more significant for the powder mixed with [Pyrr][HSO_4], further confirming the positive role of the IL in the microwave devulcanization process of rubbers. The measured crosslink density decreased

with the microwave energy, more significantly for the SBR-P, testifying that the IL favored the microwave devulcanization mechanism. Results highlighted a relationship between the soluble fraction and the devulcanization quantities. In fact, the devulcanization evaluated from Equation (5) was also higher as the microwave energy was increased and when the SBR was impregnated in IL, confirming again the positive role of this IL in the devulcanization treatment. Analysis of the temperature distribution through the ground rubber proved that microwave irradiation produced efficient heating when microwave energy was coupled with the IL. This could explain the better devulcanization of the rubber in presence of the IL. Finally, the experimental data fitted well with the Horikx's curve corresponding to the crosslink scission, suggesting that devulcanization process occurred in all microwave treated materials by rather selective breakage of crosslinks. The magnitude of this devulcanization was higher as the microwave energy was increased and when the rubber was imbibed in IL.

As a main conclusion, the use of IL exhibits strong potential towards successful and efficient devulcanization of rubbers and reduce the energy required for devulcanization treatment.

Acknowledgements

The authors thank the society Phenix Industries from Sancheville (28800), France, for its technical help.

References

[1] Fukumori K., Matsushita M., Mouri M., Okamoto H., Sato N., Takeuchi K., Suzuki Y.: Dynamic devulcanization and dynamic vulcanization for recycling of crosslinked rubber. Kautschuk Gummi Kunststoffe, **59**, 405–411 (2006).

[2] Sun X., Isayev A. I.: Ultrasound devulcanization: Comparison of synthetic isoprene and natural rubbers. Journal of Materials Science, **42**, 7520–7529 (2007). DOI: 10.1007/s10853-007-1623-9

[3] Sun X., Isayev A. I.: Continuous ultrasonic devulcanization: Comparison of carbon black filled synthetic isoprene and natural rubbers. Rubber Chemistry and Technology, **81**, 19–46 (2008). DOI: 10.5254/1.3548195

[4] Novotny D. S., Marsh R. L., Masters F. C., Tally D. N.: Microwave devulcanization of rubber. U.S. Patent 4104205 A, USA (1978).

[5] Vega B., Montero L., Lincoln S., Agulló N., Borrós S.: Control of vulcanizing/devulcanizing behavior of diphenyl disulfide with microwaves as the heating source. Journal of Applied Polymer Science, **108**, 1969–1975 (2008). DOI: 10.1002/app.27578

[6] De D., De D., Singharoy G. M.: Reclaiming of ground rubber tire by a novel reclaiming agent. I. Virgin natural rubber/reclaimed GRT vulcanizates. Polymer Engineering and Science, **47**, 1091–1100 (2007). DOI: 10.1002/pen.20790

[7] Rajan V. V., Dierkes W. K., Joseph R., Noordermeer J. W. M.: Recycling of NR based cured latex material reclaimed with 2,2′-dibenzamidodiphenyldisulphide in a truck tire tread compound. Journal of Applied Polymer Science, **102**, 4194–4206 (2006). DOI: 10.1002/app.24563

[8] Tsuchii A., Takeda K.: Rubber-degrading enzyme from a bacterial culture. Applied and Environmental Microbiology, **56**, 269–274 (1990)

[9] Karger-Kocsis J., Mészáros L., Bárány T.: Ground tyre rubber (GTR) in thermoplastics, thermosets, and rubbers. Journal of Materials Science, **48**, 1–38 (2013). DOI: 10.1007/s10853-012-6564-2

[10] Fix S. R.: Microwave devulcanization of rubber. Elastomerics, **112**, 38–40 (1980).

[11] Bani A., Polacco G., Gallone G.: Microwave-induced devulcanization for poly(ethylene–propylene–diene) recycling. Journal of Applied Polymer Science, **120**, 2904–2911 (2011). DOI: 10.1002/app.33359

[12] Landini L., de Araújo S. G., Lugão A. B., Wiebeck H.: Preliminary analysis to BIIR recovery using the microwave process. European Polymer Journal, **43**, 2725–2731 (2007). DOI: 10.1016/j.eurpolymj.2007.03.017

[13] Scagliusi S. R., Araújo S. G., Landini L., Lugão A. B.: Study of properties of chloroprene rubber devulcanizate by radiation in microwave. in 'International Nuclear Atlantic Conference 2009. Rio de Janeiro, Brazil – INAC' p.8 (2009).

[14] Hong Y. J., Jeong K. M., Saha P., Suh J., Kim J. K.: Processing and characterization of microwave and ultrasonically treated waste-EPDM/LDPE polymer composites. Polymer Engineering and Science, **55**, 533–540 (2014). DOI: 10.1002/pen.23916

[15] Maciejewska M., Zaborski M.: Effect of ionic liquids on the dispersion of zinc oxide and silica nanoparticles, vulcanisation behaviour and properties of NBR composites. Express Polymer Letters, **8**, 932–940 (2014). DOI: 10.3144/expresspolymlett.2014.94

[16] Armand M., Endres F., MacFarlane D. R., Ohno H., Scrosati B.: Ionic-liquid materials for the electrochemical challenges of the future. Nature Materials, **8**, 621–629 (2009). DOI: 10.1038/nmat2448

[17] Silvester D. S., Rogers E. L., Compton R. C., Mckenzie K. J., Ryder K. S., Endres F., Macfarlane D., Abbott A. P.: Technical aspects. in 'Electrodeposition from ionic liquids' (eds.: Enders F., MacFarlane D. R., Abbot A. P.) Wiley-VCH, Weinheim, 287–351 (2008).

[18] Anouti M., Jacquemin J., Porion P.: Transport properties investigation of aqueous protic ionic liquid solutions through conductivity, viscosity, and NMR self-diffusion measurements. Journal of Physical Chemistry B, **116**, 4228–4238 (2012).
DOI: 10.1021/jp3010844

[19] Flory P. J.: Molecular size distribution in three dimensional polymers. III. Tetrafunctional branching units. Journal of the American Chemical Society, **63**, 3096–3100 (1941).
DOI: 10.1021/ja01856a063

[20] Horikx M. M.: Chain scissions in a polymer network. Journal of Polymer Science, **19**, 445–454 (1956).
DOI: 10.1002/pol.1956.120199305

[21] Charlesby A.: Solubility and molecular size distribution of crosslinked polystyrene. Journal of Polymer Science, **11**, 513–520 (1953).
DOI: 10.1002/pol.1953.120110601

[22] Charlesby A.: Gel formation and molecular weight distribution in long-chain polymers. Proceedings of the Royal Society of London A, **222**, 542–557 (1954).
DOI: 10.1098/rspa.1954.0094

[23] Saiwari S., Dierkes W. K., Noordermeer J. W. M.: Comparative investigation of the devulcanization parameters of tire rubbers. Rubber Chemistry and Technology, **87**, 31–42 (2013).
DOI: 10.5254/rct.13.87933

[24] Levin V. Y., Kim S. H., Isayev A. I.: Effect of crosslink type on the ultrasound devulcanization of SBR vulcanizates. Rubber Chemistry and Technology, **70**, 641–649 (1997).
DOI: 10.5254/1.3538450

[25] Scuracchio C. H., Waki D. A., da Silva M. L. C. P.: Thermal analysis of ground tire rubber devulcanized by microwaves. Journal of Thermal Analysis and Calorimetry, **87**, 893–897 (2007).
DOI: 10.1007/s10973-005-7419-8

[26] Sutanto P.: Development of a continuous process for EPDM devulcanization in an extruder. PhD Thesis, University Library Groningen, Netherlands (2006).

eXPRESS Polymer Letters Vol.9, No.12 (2015) 1087–1103
Available online at www.expresspolymlett.com
DOI: 10.3144/expresspolymlett.2015.98

Industrial vegetable oil by-products increase the ductility of polylactide

A. Ruellan[1,2], A. Guinault[1], C. Sollogoub[1], G. Chollet[3], A. Ait-Mada[4], V. Ducruet[2,4], S. Domenek[2,4]*

[1]PIMM, Arts et Métiers ParisTech/CNRS/CNAM, 151 Bd de l'Hôpital, F-75013 Paris Cedex, France
[2]AgroParisTech, UMR1145 Ingénierie Procédés Aliments, 1 rue des Olympiades, F-91300 Massy, France
[3]ITERG, Lipochimie Hall Industriel, 11 rue Monge, F-33600 Pessac, France
[4]INRA, UMR1145 Ingénierie Procédés Aliments, 1 rue des Olympiades, F-91300 Massy, France

Received 15 June 2015; accepted in revised form 26 July 2015

Abstract. The use of industrial by-products of the vegetable oil industry as ductility increasing additives of polylactide (PLA) was investigated. Vegetable oil deodorization condensates were melt-blended by twin-screw extrusion up to a maximum inclusion quantity of 20 wt% without preliminary purification. Sample films were obtained by single screw cast extrusion. Compounded PLA films featured largely improved ductility in tensile testing with an elongation at break up to 180%. The glass transition temperature remained higher than room temperature. The native mixture of molecules, which composed the deodorization condensates, had superior performance compared to a synthetic mixture of main compounds. The investigation of the correlation between composition of the additives and the ductility of the PLA blends by Principal Component Analysis showed synergy in property improvement between fatty acids having a melting point below and beyond the room temperature. Furthermore, a compatibilizing effect of molecules present in the native mixture was evidenced. Oil deodorization condensates, which are a price competitive by-product of the vegetable oil industry, are therefore a very promising biobased and biodegradable additive for improving the ductility of PLA.

Keywords: *biodegradable polymers, poly(lactic acid), ductility, vegetable oil by-products, crazing*

1. Introduction

Biodegradable and/or biobased polymers are widely studied to replace petroleum-based materials with the aim of contributing to higher sustainability of plastics. However, in many cases these new products still do not meet economical or functional requirements to be competitive in commodity applications. Polylactide (PLA) is one of the polymers which can potentially enter high volume markets, mostly in the food packaging [1–3] or textile [4] sector. Polylactide is a biobased and compostable polymer [5–7] issued from polymerization of lactic acid produced by fermentation of starch, potatoes or beets [7, 8]. Although it has been known before [9], production cost reduction in the 1990s and 2000s thanks to breakthroughs in the polymerization technology [10, 11], made it economically competitive with petroleum-based materials. PLA offers many interests such as a glass transition higher than room temperature, ease of processing, high transparency, printability, glossy aspect [1, 12, 13]. However, its mechanical properties still remain an obstacle for many applications. In fact, PLA features high tensile strength and modulus but also high brittleness [14]. In order to enhance the PLA ductility, melt-blending with rubbery materials as poly(ether)urethane [15,

*Corresponding author, e-mail: sandra.domenek@agroparistech.fr

16], polyamide elastomer [17], acrylonitrile-butadiene-styrene copolymer, or various impact modifiers [18–26] is effective. Furthermore, plasticizers such as citrate esters [27–37], polyethylene glycols [27, 33, 38–44] or manifold other molecules [29, 43, 45–48] can be used. Unfortunately, impact modifiers are often not biodegradable nor biobased and plasticizers are generally derived from fossil resources, degrading one important environmental advantage of employing PLA. Therefore biobased and biodegradable additives have been and are investigated for toughening PLA. Chemically modified vegetable oils have received important research interest, because ester or epoxy groups can be degraded by microorganisms [49], maintaining the biodegradability of blends with PLA. Polymerized soybean oil derivatives prepared by crosslinking double bonds of alkyl chains afforded ductility increase after melt-blending with PLA and using a compatibilizer [50]. Improvements were also obtained with conjugated soybean oil which was reactively compatibilized with PLA by unsaturated triglycerides [51]. Epoxidized soybean oil [52–55] and epoxidized palm oil [56–58] also showed some positive effects on PLA toughness. Another approach consists in using rigid particles, which usually increased stiffness but is ineffective, or even detrimental for the ductility. Nonetheless, NatureWorks [59] reported the use of EMforce®, a mineral additive, able to change the polymer failure mode from brittle to ductile. In fact, the efficient crack initiation in glassy PLA, which was provided by the well-dispersed additive with good interfacial adhesion to the matrix, enhanced the PLA elongation at break.

Expertise from plasticizing polyvinylchloride teaches that mixtures of different plasticizers are efficient for increasing toughness, because they make use of different mechanisms available for ductility improvement [49]. For example, a mixture of tributyl citrate (TBC) and a block copolymer PLA-g-polyethyleneglycol yielded a material with high elongation at break and satisfying stress at yield [30]. Al-Mulla *et al*. [55] successfully used modified nanoclays in combination with epoxidized soybean oil to increase stiffness and ductility. The combination of PLA with rubber and compatibilizers has also been investigated by several authors, showing important gains in ductility, with an elongation at break of up to 160% for high rubber concentrations [60] or bicontinous phases [61], and up to 200% when using compatibilizers [62, 63]. However, these solutions often require the inclusion of several additives, chemically modified and costly components that increase the price of the final formulation, which is inappropriate for a large volume production. Finding a low cost biobased and biodegradable toughening agent would therefore help PLA to conquer new markets.

Vegetable oils contain a number of potentially interesting molecules for PLA toughening and the refinery of vegetable oils gives rise to several by-products. Among those, oil deodorization condensates represent a high-volume by-product, which is chemically close to the vegetable oil. They are obtained by distillation in the aim of purifying the raw oil from odorous compounds, which are negative for the sensorial properties of vegetable oils. Deodorization condensates contain free fatty acids, glycerides and unsaponifiable molecules. The objective of this study was to use vegetable oils and the by-product deodorization condensate as produced for toughening PLA. The individual molecules which make up oils and deodorization condensates were tested on the mechanical properties and several vegetable oils were screened.

2. Experimental

2.1. Materials

PLA 4060D was supplied by NatureWorks (U.S.A.) and consists of 89±1% L-lactic acid and 11±1% D-lactic acid units, making it unable to crystallize under common conditions [1, 64]. The glass transition temperature (T_g) obtained from differential scanning calorimetry (DSC) measurements was 56°C. Average molecular weights obtained from size exclusion chromatography (SEC) measurements were M_w = 236 800 g·mol^{-1}, M_n = 103 700 g·mol^{-1} and dispersity M_w/M_n = 2,28.

Hydrogenated palm oil (HPO), Hydrogenated Copra Oil (HCO), Rapeseed Oil Deodorization Condensate (RODC), Soybean Oil Deodorization Condensate (SODC), Olive Oil Deodorization Condensate (OODC) and Palm Oil Deodorization Condensate (PODC) were supplied by ITERG (Bordeaux, France).

Palmitic acid (purity >98%) *i.e*. hexadecanoic acid (C16:0), oleic acid (purity >96%) *i.e*. 9-octadecenoic acid (C18:1), squalene (purity >98%) *i.e*. (6E,10E,14E,18E)-2,6,10,15,19,23-hexamethyltetracosa-2,6,10,14,18,22-hexaene, and alpha-toco-

pherol (purity >96%) *i.e*. (2R)-2,5,7,8-tetramethyl-2-[(4R,8R)-(4,8,12-trimethyltridecyl)]-6-chromanol, were supplied by Sigma-Aldrich (France).

2.2. Film fabrication

Prior to melt-blending, PLA pellets were dried at 60°C for 24 h under dried air using a SOMOS 60L. Relative humidity of dried pellets was controlled to be lower than 350 ppm using an Aboni FMX Hydrotracer (France). Melt-mixing of PLA with or without additives was carried out using a twin screw extruder (Thermo Haake Ptw 16-40D, France), having a screw diameter of 16 mm and a length to diameter ratio (*L*/*D*) 40:1. A temperature of 180°C was used to process by twin-screw extrusion the PLA pellets as reference material, while the temperature profile of the 7 heating zones decreased from 180 to about 150/130°C along the extrusion flow, depending on the nature and the amount of additive. Screw speed was 300 rpm. The exact temperature profile for each formulation is given in Table 1. To properly control the feed rate of additives, which are solid at room temperature, a home-made apparatus consisting in a heated syringe was used. Obtained pellets were stored into hermetic sealed metalized bags to avoid PLA rehydration.

Films of about 0.8 mm thickness containing palmitic acid, oleic acid, hydrogenated palm oil, hydrogenated copra oil, squalene, α-tocopherol and some combinations of these products were obtained using a single screw extruder (Scamex Rheoscam, France), mounted with a screw of 20 mm diameter and a length to diameter ratio (*L*/*D*) 12:1 and a flat die of 40 mm width and 1 mm thickness. Films were stretched and cooled with chill rolls. Due to the short length of the screw, an increasing temperature profile from 180 to 195°C over the 3 heating zones was used for PLA, while it was decreasing from 180

Table 1. Processing conditions of melt-mixing twin screw extrusion

Formulation		Temperature profile [°C]
Neat PLA		175/180/190/190/190/190/180
PLA + 10 wt% C16:0		175/180/180/170/170/170/170
PLA + 10 wt% C18:1		175/180/180/170/170/170/170
PLA + 10 wt% [50 wt% C16:0 + 50 wt% C18:1]		175/180/180/170/170/170/170
PLA + 10 wt% [95 wt% (50 wt% C16:0 + 50 wt% C18:1) + 5 wt% HPO]		175/180/180/170/170/170/170
PLA +	5 wt% HCO	175/180/180/180/180/170/170
	10 wt% HCO	175/180/180/180/180/170/170
	15 wt% HCO	175/180/180/180/170/170/160
PLA +	5 wt% HPO	175/180/180/180/180/170/170
	10 wt% HCO	175/180/180/180/180/170/170
	15 wt% HCO	175/180/180/180/180/170/170
PLA +	5 wt% α-tocopherol	175/180/180/180/180/180/180
	10 wt% α-tocopherol	175/180/180/180/180/180/170
	15 wt% α-tocopherol	175/180/180/180/180/170/170
PLA +	5 wt% squalene	175/180/180/180/180/180/180
	10 wt% squalene	175/180/180/180/180/170/170
	15 wt% squalene	175/180/180/180/180/170/170
PLA +	5 wt% RODC	175/180/180/180/180/175/170
	10 wt% RODC	175/180/180/180/180/170/160
	15 wt% RODC	175/180/180/180/180/170/160
	20 wt% RODC	175/180/180/180/170/160/150
PLA +	5 wt% SODC	175/180/180/180/180/175/170
	10 wt% SODC	175/180/180/180/180/170/160
	15 wt% SODC	175/180/180/180/180/170/160
	20 wt% SODC	175/180/180/180/170/160/150
PLA +	5 wt% OODC	175/180/180/170/170/170/170
	10 wt% OODC	175/180/180/170/170/170/170
	15 wt% OODC	175/180/180/170/170/160/160
	20 wt% OODC	175/180/180/170/160/150/150
PLA +	5 wt% PODC	175/180/180/180/180/175/170
	10 wt% PODC	175/180/180/180/170/160/155
	15 wt% PODC	175/180/180/180/170/160/150
	20 wt% PODC	175/180/180/170/160/150/135

Table 2. Processing conditions of cast films extrusion

Formulation		Temperature profile [°C]	Die temperature [°C]
Neat PLA		180/190/195	185
PLA + 10 wt% C16:0		180/180/175	170
PLA + 10 wt% C18:1		180/180/175	170
PLA + 10 wt% [50 wt% C16:0 + 50 wt% C18:1]		180/180/175	170
PLA + 10 wt% [95 wt% (50 wt% C16:0 + 50 wt% C18:1) + 5 wt% HPO]		180/180/175	170
PLA +	5 wt% HCO	180/180/180	180
	10 wt% HCO	180/170/170	170
	15 wt% HCO	180/170/170	170
PLA +	5 wt% HPO	180/180/180	170
	10 wt% HPO	180/170/170	170
	15 wt% HPO	180/170/170	170
PLA +	5 wt% α-tocopherol	180/180/180	180
	10 wt% α-tocopherol	180/180/180	180
	15 wt% α-tocopherol	180/175/170	170
PLA +	5 wt% squalene	180/180/180	180
	10 wt% squalene	180/180/175	170
	15 wt% squalene	180/180/170	170

to about 170°C for blends. The specific temperatures depending on the nature and the amount of additive are given in Table 2.

In the case of the deodorization condensates of the vegetable oils (RODC, SODC, OODC, PODC), the available quantity was insufficient for carrying out a single screw extrusion in the aim to obtain films. In that case PLA sheets of 1 mm thickness were thermo-moulded by compression at 220 bar (Laboratory Press Gibitre Instruments 20 tons, Italy). For this, pellets were pre-melted at 180°C without pressure during 180 seconds then heating plates were closed with progressive increase in pressure during 120 seconds to eliminate air bubbles.

2.3. Chemical and physical chemical characterization of vegetable oils and deodorization condensates

Glyceride composition of fats was determined according to the IUPAC 6.002 and EN 14105 standards using a Shimadzu GC-2010 Plus gas chromatograph (France) equipped with a Zebron ZB 5 HT Inferno (15 m, 0.25 mm, 0.1 µm) column and a flame ionization detector set at 380°C. The vector gas was H_2 at a flow rate of 1.17 mL·min^{-1}. Both the injector and the oven temperature were set at 60°C for 3 min, then raised to 370°C at 10°C·min^{-1} and held at 370°C for 12 min. Direct on-column injection was performed.

Fatty acid composition was determined according to the ISO 12966-2 standard using a Shimadzu GC-2010 Plus gas chromatograph (France) equipped with a BPX70 (50 m, 0.22 mm, 0.25 µm) column, and a flame ionization detector set at 250°C. The vector gas was H_2 at a flow rate of 0.32 mL·min^{-1}. The oven temperature was set at 60 C for 2 min, raised to 170°C at 20°C·min^{-1}, held at 170°C for 25 min, raised to 230°C at 4°C·min^{-1} and held at 230°C for 10 min. The injector temperature was set at 250°C and a split ratio of 200 was used.

Acid value was determined according to the ISO 660 standard using a mixture of ethanol 95% and diethylic ether as solvent, potassium hydroxide 0.5 mol·L^{-1} in ethanol 95% as titrant and alkali blue 6B as indicator.

Saponification value was determined according to the ISO 3657 standard. Samples were saponified with potassium hydroxide 0.5 mol·L^{-1} in ethanol 95% boiled under reflux during 2 h. Hydrochloric acid 0.5 mol·L^{-1} was used as titrant and alkali blue 6B as indicator.

Water content was measured using a Mettler Toledo HB43 S Halogen Moisture Analyzer set (France) at 103°C.

Melting point of free fatty acids was determined from literature [65]. Estimation of mono, di- and triglycerides average chemical structure of oil deodorization condensates was based on the averages unsaturation number and the alkyl chains length of the corresponding free fatty acids composition profile (Table 3). Average glycerides melting point was estimated calculating a weighted average of the

Table 3. Composition of hydrogenated vegetable oils and vegetable oil deodorization condensates

Type			HPO	HCO	RODC	SODC	OODC	PODC
Glyceride composition [%]	Free fatty acids		0.0	0.0	39.0	43.1	39.2	95.4
	Monoglycerides		0.2	0.0	11.2	2.9	2.0	1.7
	Diglycerides		10.6	0.0	2.7	9.0	8.4	2.2
	Triglycerides		88.9	100	12.2	16.8	33.5	0.7
	Sterols (α-tocopherol)		0.0	0.0	25.7	9.8	1.6	0.0
	Hydrocarbons (Squalene)		0.0	0.0	0.0	13.8	13.0	0.0
	Unidentified		0.3	0.0	9.2	4.6	2.3	0.0
Acid value [mg KOH·g^{-1}]			0.1	0.1	65.3	68.4	47.7	201.0
Saponification value [mg KOH·g^{-1}]			198.6	255.2	125.1	157.9	162.2	205.7
Water content [%]			0.11	0.10	0.55	0.34	0.37	0.16
Fatty acid composition [%]	Caproic acid	C6:0	0.0	0.5	0.0	0.0	0.0	0.0
	Caprylic acid	C8:0	0.0	6.8	0.0	0.0	0.0	0.0
	Capric acid	C10:0	0.0	5.7	0.0	0.0	0.1	0.0
	Lauric acid	C12:0	0.5	47.5	0.0	0.8	0.0	0.4
	Myristic acid	C14:0	1.2	18.1	0.0	0.4	0.0	1.3
	Palmitic acid	C16:0	43.6	9.4	7.4	12.3	11.3	49.8
	Palmitoleic acid	C16:1	0.0	0.0	0.0	0.0	0.0	0.2
	Stearic acid	C18:0	53.8	10.8	3.4	4.1	2.5	4.1
	Oleic acid	C18:1	0.0	1.0	27.3	21.7	69.5	35.2
	Linoleic acid	C18:2	0.0	0.0	42.4	49.7	10.9	7.8
	Linolenic acid	C18:3	0.0	0.0	1.5	6.4	0.6	0.3
	Arachidic acid	C20:0	0.5	0.1	0.5	0.3	0.4	0.3
	Eicosenoic acid	C20:1	0.0	0.0	0.3	0.2	0.4	0.1
	Behenic acid	C22:0	0.1	0.0	1.0	0.5	0.0	0.0
	Lignoceric acid	C24:0	0.1	0.0	0.5	0.2	0.1	0.0
	Unidentified		0.5	0.1	0.2	15.7	13.4	4.2
Average alkyl chain carbon quantity			17.1	13.0	17.9	17.7	17.8	16.9
Average alkyl chain unsaturation quantity			0.0	0.0	1.4	1.5	1.0	0.5

specific melting points of the contained molecules taken from references [65–67]. Physical properties of molecules are given in Table 4.

2.4. Calculation of solubility parameters

Molar volumes and molar attraction constants of polylactide and additives were determined according to the van Krevelen and Hoftyzer atomic group contribution method [68]. Average molar volumes and average molar attraction constants of mono, di and triglycerides of oil deodorization condensates were estimated based on average chemical structures previously determined.

Hansen Solubility parameters were calculated using Equations (1), (2) and (3) [69, 70]. Used molar constant values [68] are presented in Table 5:

$$\delta_d = \frac{\Sigma F_{dt}}{\Sigma V_i} \quad (1)$$

$$\delta_p = \frac{\sqrt{\Sigma F_{Pi}^2}}{\Sigma V_i} \quad (2)$$

$$\delta_h = \frac{\sqrt{\Sigma E_{hi}}}{\Sigma V_i} \quad (3)$$

where δ_d is the dispersion component of the solubility parameter in J$^{1/2}$·cm$^{-3/2}$, δ_p the polar component of the solubility parameter in J$^{1/2}$·cm$^{-3/2}$, δ_h the hydrogen bonding component of the solubility parameter in J$^{1/2}$·cm$^{-3/2}$, F_d the dispersion contribution of the molar attraction constant in (J$^{1/2}$·cm$^{-3/2}$)·mol^{-1}, F_p the polar contribution of the molar attraction constant in (J$^{1/2}$·cm$^{-3/2}$)·mol^{-1}, E_h the hydrogen bonding energy contribution of the molar attraction constant in J·mol^{-1} and V the molar volume contribution of the chemical group involved in cm^3·mol^{-1}.

The solubility of the molecules in PLA (Table 4) was assessed using the HSP Relative Energy Difference (RED) from Equations (4) and (5):

$$Distance = \sqrt{4(\delta_{d_{molec}} - \delta_{d_{PLA}})^2 + (\delta_{p_{molec}} - \delta_{p_{PLA}})^2 + (\delta_{h_{molec}} - \delta_{h_{PLA}})^2} \quad (4)$$

$$RED = \frac{Distance}{Radius} \quad (5)$$

Table 4. Physical properties and solubility parameters of fatty acids, mono-, di-, and triglycerides contained in the hydrogenated vegetable oils and oil deodorization condensates

			Molar weight [g·mol^{-1}]	Molar volume [cm^3·mol^{-1}]	Melting point [°C]	Hansen Solubility Parameters (HSP)				
						δ_d [J$^{1/2}$·cm$^{-3/2}$]	δ_p [J$^{1/2}$·cm$^{-3/2}$]	δ_h [J$^{1/2}$·cm$^{-3/2}$]	Distance with PLA	RED with PLA
PLA 4060D			242 800	–	–	18.6	9.9	6.0	(radius: 10.7)	–
Free fatty acids	Caproic acid	C6:0	116	126	–3[a]	16.06	3.32	8.89	8.80	0.82
	Caprylic acid	C8:0	144	159	16[a]	16.20	2.65	7.94	8.91	0.83
	Capric acid	C10:0	172	191	31[a]	16.30	2.20	7.24	9.05	0.85
	Lauric acid	C12:0	200	223	44[a]	16.37	1.88	6.70	9.20	0.86
	Myristic acid	C14:0	228	255	55[a]	16.42	1.65	6.26	9.34	0.87
	Palmitic acid	C16:0	256	287	63[a]	16.46	1.46	5.90	9.46	0.88
	Palmitoleic acid	C16:1	254	282	1[a]	16.27	1.49	5.95	9.62	0.90
	Stearic acid	C18:0	285	320	70[a]	16.49	1.31	5.59	9.58	0.89
	Oleic acid	C18:1	283	314	13[a]	16.32	1.34	5.64	9.71	0.91
	Linoleic acid	C18:2	280	309	–9[a]	16.14	1.36	5.69	9.86	0.92
	Linolenic acid	C18:3	278	304	–14[a]	15.95	1.38	5.74	10.03	0.94
	Arachidic acid	C20:0	313	352	75[a]	16.52	1.19	5.33	9.68	0.90
	Eicosenoic acid	C20:1	311	347	23[a]	16.36	1.21	5.37	9.80	0.92
	Behenic acid	C22:0	341	384	80[a]	16.54	1.09	5.10	9.77	0.91
	Lignoceric acid	C24:0	369	416	84[a]	16.55	1.01	4.90	9.85	0.92
Monoglycerides	HPO	$(HO)_2$–Gly–(C17.1:0)	346	346	68–76[b]	17.14	2.49	11.66	9.77	0.91
	RODC	$(HO)_2$–Gly–(C17.9:1.4)	354	351	10–22[b]	16.92	2.45	11.56	9.89	0.92
	SODC	$(HO)_2$–Gly–(C17.5:1.5)	351	348	8–18[b]	16.56	2.47	11.63	10.17	0.95
	OODC	$(HO)_2$–Gly–(C17.8:1.0)	354	352	25–32[b]	16.98	2.44	11.56	9.84	0.92
	PODC	$(HO)_2$–Gly–(C16.9:0.5)	342	340	45–55[a, c]	17.07	2.53	10.00	8.93	0.83
Diglycerides	HPO	HO–Gly–$(C17.1:0)_2$	600	630	65–72[b]	16.82	1.36	7.34	9.35	0.87
	RODC	(HO)–Gly–$(C17.9:1.4)_2$	617	642	2–12[b]	16.59	1.33	6.49	9.48	0.89
	SODC	(HO)–Gly–$(C17.7:1.5)_2$	611	634	–4–8[b]	16.57	1.35	7.32	9.56	0.89
	OODC	(HO)–Gly–$(C17.8:1.0)_2$	615	643	10–20[b]	16.66	1.33	7.27	9.50	0.89
	PODC	(HO)–Gly–$(C16.9:0.5)_2$	592	619	42–48[b]	16.74	1.38	7.41	9.41	0.88
Triglycerides	HCO	Gly-$(C13:0)_3$	681	717	8–42	16.68	1.18	5.41	9.54	0.89
	HPO	Gly–$(C17.1:0)_3$	854	915	62–66[c]	16.70	0.93	4.79	9.82	0.92
	RODC	Gly–$(C17.9:1.4)_3$	879	932	–30– –26[c]	16.46	0.91	4.75	10.03	0.94
	SODC	Gly–$(C17.7:1.5)_3$	870	921	–32– –28[c]	16.44	0.92	4.78	10.04	0.94
	OODC	Gly–$(C17.8:1.0)_3$	877	933	–14– –10[c]	16.53	0.91	4.74	9.98	0.93
	PODC	Gly–$(C16.9:0.5)_3$	842	898	15–25[c]	16.61	0.95	4.84	9.87	0.92
Others	α-tocopherol	–	431	436	2[a]	17.63	1.47	7.27	8.74	0.82
	Squalene		411	477	–7[a]	16.10	0.00	0.00	12.61	1.18

[a]from [65], [b]from [66], [c]from [67]

Table 5. Used group contribution molar constants

Group	F_d [$(J^{1/2}\cdot cm^{-3/2})\cdot mol^{-1}$]	F_p^2 [$(J\cdot cm^{-3})\cdot mol^{-1}$]	E_h [$J\cdot mol^{-1}$]	Molar volume [$cm^3\cdot mol^{-1}$]
$-CH_3$	420	0	0	33.5
$-CH_2-$	270	0	0	16.1
=CH–	200	0	0	13.5
>CH–	80	0	0	–1.0
>C<	–70	0	0	–1
=C<	70	0	0	–5.5
–COO–	390	240 100	7 000	18
–COOH	530	176 400	10 000	28.5
–OH	210	250 000	20 000	10
Ring	190	0	0	16

where δ_d, δ_p, and δ_h are the components of the solubility parameter of the molecules and the PLA obtained from Equations (1), (2) and (3), where the radius value is the maximal distance obtained from [71] beyond which the molecules are not miscible anymore with the polymer. Therefore, the closer the RED value to zero, the better the compatibility. A RED value higher than 1 means a theoretical non-miscibility of the additive with PLA.

2.5. Physical-chemical characterization PLA blends

Differential Scanning Calorimetry (DSC) analyses were performed using a Mettler Toledo (France) DSC1 STARe System under nitrogen atmosphere (50 mL·min^{-1}) in 40 µL standard Aluminum pans (Mettler). Calibration of the device was done using Indium and Zinc standards. Calorimetric scans of additives were performed from –80 to 220°C at a heating rate of 2°C·min^{-1}. Experiments were carried out in duplicate. Calorimetric scans of blended PLA samples were done at a heating/cooling rate of 10°C·min^{-1}. The first heating scan for sample rejuvenation was performed from 25 to 75°C with an isotherm at 75°C during 2 min. Then, the cooling scan was from 75 to –20°C and the second heating scan from –20 to 100°C. The glass transition temperature (T_g) was taken at the midpoint of the second heating scan. Experiments were done in triplicate.

Tensile properties were investigated at 23°C, relative humidity (RH) 50±10 % and cross-head speed of 25 mm·min^{-1}, using an universal tensile machine (Instron model 4301, France) equipped with a load cell 1000±1 N and without extensiometer. The dog bone shaped samples (ISO 527-2, type 5A) were directly cut from the materials. Prior to tensile testing, samples were conditioned at 23°C and 50±10% RH for at least 72 h. Each mechanical characteristic value is an average of 8 measurements.

Uniaxial deformation under an optical microscope was done in cutting rectangular samples of 20 mm length, 4 mm width, and 0.8 mm thickness from blank PLA, PLA + 10 wt% C16:0, PLA + 10 wt% C18:1 and PLA + 10 wt% PODC films. They were stretched at 5 mm·min^{-1} using a homemade tensile machine placed under an Olympus Japan optical microscope mounted with WHK 10×/20 L ocular lens and MD Plan 10 0.25 objective lens. Observations were performed in optical transmission light mode using a Sony CCD-IRIS Model DXC-107P camera (France).

The morphology of the dispersed phase of PLA + 10 wt% C16:0, PLA + 10 wt% C18:1 and PLA + 10 wt% PODC materials before and after being stretched was observed with Scanning Electron Microscopy (SEM) (Hitachi 4800 II, France). Observations were directly conducted on the longitudinal surface of the dog bone shaped samples without any previous preparation.

2.6. Principal component analysis (PCA)

PCA was carried out considering the contents of each free fatty acid, mono, di and triglyceride types, hydrocarbons, sterols and water, the acid and saponification values and the measured elongation at break [%], Young modulus and T_g values of the PLA formulations tested. PCA was done with XLstat software.

3. Results and discussion

3.1. Effects of free fatty acids, glycerides, α-tocopherol and squalene on PLA ductility

Individual components present in vegetable oils, which could feature toughening ability for PLA, as free fatty acids, glycerides, and the unsaponifiable

components as α-tocopherol and squalene were tested. In order to achieve the most efficient formulation, the solubility of a molecule in the polymer matrix is one determinant for its plasticizing power [37]. Therefore the Hansen Solubility Parameters (HSP) of each compound was calculated. HSP (Table 4) shows low solubility of the different compounds in the PLA matrix. All the obtained values are close to one, which marks the solubility limit. The highest solubility (although still modest) was displayed by small fatty acids and α-tocopherol. The mechanical and thermal properties of the corresponding compounds are given in Table 6. The raw data of typical stress/strain curves of blends are presented in Figure 1. The DSC thermograms of neat additives in Figure 2 and of blends in Figure 3 for further information.

Literature studies on the use of vegetable oil as toughening agent of PLA showed that generally chemical modification is required to obtain positive effects [50, 52–54, 56–58, 72]. Not surprisingly due to their low solubility in PLA, the impact of the tested fatty acids (C16:0, C18:1), vegetable oils (HPO and HCO) and unsaponifiable compounds on T_g was negligible. However, despite the low solubility of the compounds, PLA ductility was increased in some cases. In particular, HCO, which contains mainly triglycerides, but with short chain length, improved the PLA ductility and lowered the apparent Young modulus, stress and elongation at yield. HPO, which mostly contains triglycerides and some diglycerides with higher chain length did not bring significant ductility enhancement nor T_g decrease. HSP of di- and triglycerides from HPO and triglycerides from HCO

Table 6. Mechanical and thermal properties of formulations

Formulation		Elongation at break [%]	app. Young modulus[a] [MPa]	Elongation at yield [%]	Stress at yield [MPa]	T_g [°C]
PLA (twin screw pellets)		6±1	1760±90	4.2±0.4	64±5	56.3±0.2
PLA + 10 wt% C16:0		4±1	1720±60	3.2±0.1	50±3	49.3±0.1
PLA + 10 wt% C18:1		16±5	1440±50	2.2±0.1	28±2	45.2±0.2
PLA + 10 wt% [50 wt% C16:0 + 50 wt% C18:1]		45±12	1590±80	2.2±0.1	31±2	40.7±0.3
PLA + 10 wt% [95 wt% (50 wt% C16:0 + 50 wt% C18:1) + 5 wt% HPO]		74±15	1550±120	2.2±0.2	25±4	39.8±0.4
PLA +	5 wt% HCO	9±3	1680±70	3.6±0.2	51±1	54.1±0.2
	10 wt% HCO	9±6	1540±80	3.6±0.2	42±2	54.1±0.1
	15 wt% HCO	11±5	1460±70	3.8±0.2	38±2	54.8±0.3
PLA +	5 wt% HPO	55±20	1610±50	2.7±0.1	38±1	52.6±0.2
	10 wt% HPO	85±15	1420±70	2.6±0.2	26±2	54.4±0.4
	15 wt% HPO	91±14	1300±80	2.4±0.1	26±1	53.9±0.3
PLA +	5 wt% α-tocopherol	6±2	1150±90	3.8±0.2	41±4	51.3±0.2
	10 wt% α-tocopherol	5±2	1070±60	4.0±0.4	31±3	49.8±0.2
	15 wt% α-tocopherol	8±3	990±70	3.9±0.3	29±4	47.1±0.2
PLA +	5 wt% squalene	38±7	1180±90	3.3±0.4	36±7	51.4±0.2
	10 wt% squalene	51±9	990±60	3.1±0.9	28±3	49.5±0.2
	15 wt% squalene	29±7	890±80	2.9±0.7	19±2	49.4±0.1
PLA +	5 wt% RODC	22±3	1530±80	3.2±0.2	40±3	52.6±0.2
	10 wt% RODC	55±7	1490±140	2.4±0.2	28±4	49.1±0.1
	15 wt% RODC	65±15	1380±155	2.3±0.3	23±4	48.8±0.1
	20 wt% RODC	73±20	1270±150	2.2±0.3	20±4	48.5±0.3
PLA +	5 wt% SODC	29±8	1550±110	3.3±0.3	41±7	50.6±0.1
	10 wt% SODC	73±18	1510±90	2.3±0.2	25±5	49.4±0.3
	15 wt% SODC	80±13	1340±80	2.2±0.3	23±3	48.7±0.1
	20 wt% SODC	52±15	1220±100	2.1±0.4	16±4	47.5±0.1
PLA +	5 wt% OODC	49±6	1430±90	3.1±0.3	34±4	49.5±0.2
	10 wt% OODC	85±17	1490±90	2.6±0.2	31±2	49.0±0.1
	15 wt% OODC	88±16	1360±70	2.1±0.2	20±3	48.5±0.1
	20 wt% OODC	67±16	1370±110	2.2±0.2	21±3	48.7±0.1
PLA +	5 wt% PODC	51±17	1680±110	2.5±0.2	36±2	45.3±0.1
	10 wt% PODC	132±18	1460±40	2.1±0.2	24±1	39.2±0.2
	15 wt% PODC	179±15	1180±130	2.3±0.3	18±2	35.1±0.2
	20 wt% PODC	84±31	1130±60	2.0±0.4	14±3	33.8±0.2

[a]apparent Young modulus for comparison reasons obtained without extensiometer

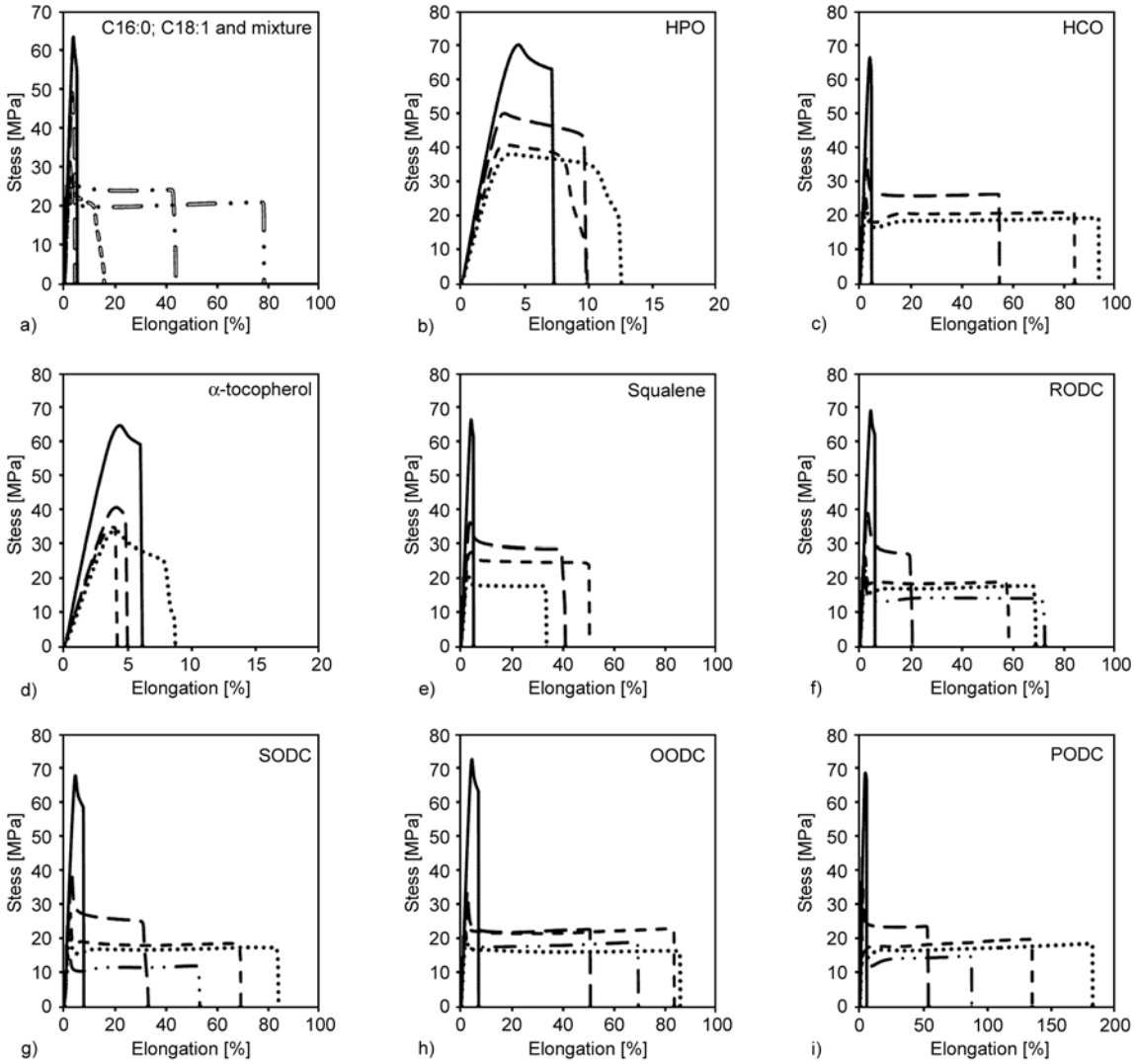

Figure 1. Stress/strain curves of PLA blends with free fatty acids, hydrogenated vegetable oils (HPO and HCO), unsaponifiable compounds (squalene, α-tocopherol), and vegetable oil deodorization condensates (palm oil PODC, olive oil OODC, soybean oil SODC and rapeseed oil RODC); (—) neat PLA; (== ==) PLA + 10 wt% C16:0; (= =) PLA + 10 wt% C18:1; (== •) PLA+ 10 wt% [50 wt% C16:0 + 50 wt% C18:1]; (== • •) PLA + 10 wt% [95 wt% (50 wt% C16:0 + 50 wt% C18:1) + 5 wt% HPO]; (— —) PLA + 5 wt% additive; (- - -) PLA + 10 wt% additive; (• •) PLA + 15 wt% additive; (— • •) PLA + 20 wt% additive

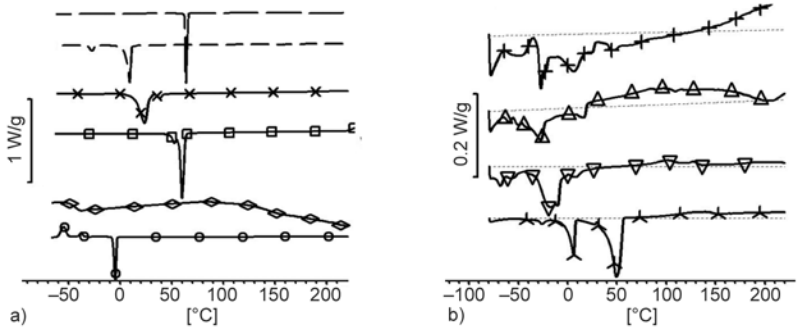

Figure 2. Thermograms (first heating scan) of free fatty acids, hydrogenated vegetable oils (HPO and HCO), unsaponifiable compounds (squalene, α-tocopherol), and vegetable oil deodorization condensates (palm oil PODC, olive oil OODC, soybean oil SODC and rapeseed oil RODC); (— —) C16:0; (– –) C18:1; (×) HCO; (□) HPO; (◊) α-tocopherol; (○) squalene; (+) RODC; (Δ) SODC; (▽) OODC; (⅄) PODC

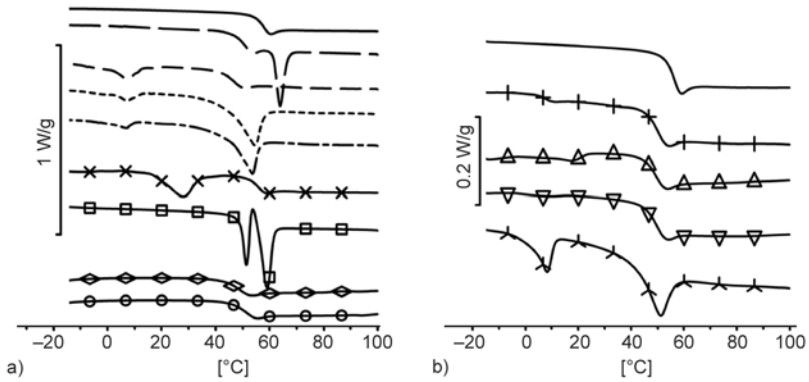

Figure 3. Thermograms (second heating scan) of PLA blends with free fatty acids, hydrogenated vegetable oils (HPO and HCO), unsaponifiable compounds (squalene, α-tocopherol), and vegetable oil deodorization condensates (palm oil PODC, olive oil OODC, soybean oil SODC and rapeseed oil RODC); (—) neat PLA; (— —) PLA + 10 wt% C16:0; (– –) PLA + 10 wt% C18:1; (- - -) PLA + 10 wt% [50 wt% C16:0 + 50 wt% C18:1]; (— -) PLA + 10 wt% [95 wt% (50 wt% C16:0 + 50 wt% C18:1) + 5 wt% HPO]; (×) PLA + 10 wt% HCO; (□) PLA + 10 wt% HPO; (◊) PLA + 10 wt% α-tocopherol; (○) PLA + 10 wt% squalene; (+) PLA + 10 wt% RODC; (Δ) PLA + 10 wt% SODC; (▽) PLA + 10 wt% OODC; (⅄) PLA + 10 wt% PODC

were close, while the average molar volume and molecular weight of triglycerides from HCO are smaller than the ones from HPO (Table 2). Testing of single fatty acids with longer chain length (C16:0, C18:1) showed that they were not able to increase PLA ductility. This is coherent with existing literature. For example, Jacobsen and Fritz [73] studied PLA blends with fatty acid esters. No significant ductility improvement was observed. The blending with the unsaponifiable compound α-tocopherol showed small gains in elongation at break, which extends already existing knowledge. It was already shown that the use of α-tocopherol as a natural antioxidant in PLA at small quantities (<4 wt%) induced a slightly T_g decrease [74] but no increase in elongation at break [75]. Here, no elongation at break improvement upon was found using greater α-tocopherol amounts, despite solubility was assessed to be higher than other molecules (such as HPO and HCO, Table 4) and a T_g decrease was observed (Table 3). Squalene, which is a natural tri-terpene found in vegetable oils, showed some toughening abilities (Table 6) despite its low solubility in PLA (Table 4). In fact, the creation of a dispersed phase promoting crazing was most probably responsible for this effect [37].

The most interesting result was obtained upon mixing different compounds. A mix of C18:1 and C16:0 fatty acids increased the PLA ductility much more than using them separately. The Young modulus and the T_g remained higher than using only C18:1 likely because of its lower content involved, while the stress and elongation at yield were lessened as much as adding only C18:1. Mixture made of [95 wt% (50 wt% C16:0 + 50 wt% C18:1) + 5 wt% HPO] at a total content of 10 wt% in PLA, further enhanced the ductility. There was apparently a synergistic effect between compounds, which can be possibly exploited.

3.2. Properties of PLA blends with vegetable oil deodorization condensates

Deodorization oil condensates are mixtures of different molecules contained in vegetable oils, the composition of which depends on the botanic source and oil refinery process. Four kinds of oil deodorization condensates (RODC, SODC, OODC and PODC) were blended with PLA, each at four concentrations (5, 10, 15 and 20 wt%). As shown in Table 3, content in free fatty acids, mono di or triglycerides, sterols (mainly alpha-tocopherol) and hydrocarbons (mainly squalene) was highly variable, as well as unsaturation degree of fatty acids. From the composition, an average HSP was calculated and is given in Table 4. As observed in Table 4, the longer and/or more unsaturated the alkyl chain is, the lower the solubility in PLA. However, except for very short fats alkyl chains and organic compounds as α-tocopherol or squalene, HSP of involved molecules appear to be rather similar. Mechanical and thermal properties of PLA/oil deodorization condensates blends are given in Table 6 and typical curves of raw data are shown in the Figure 1. Significant increases in elongation at break were obtained, especially with the PODC. Addition of too much additive, *i.e.* about 20 wt%, induced a stagnation or decrease in the elongation at break. All the deodorization condensates led to a

lowering in the stress and elongation at yield. Interestingly, the apparent Young modulus of materials remained high. The stress/strain curves (Figure 1) showed that the yielding peak shrunk and flattened with the increase in additive content, as if the yield critical stress would tend to meet the plateau value where the stress remains constant with the strain. There is thus an important gain of using native mixtures of fatty acids present in deodorisation condensates for PLA ductility increase.

3.3. Study of the deformation mechanisms involved in PLA/oil deodorization condensates blends

In all samples the T_g remained higher than the measurement temperature, the main deformation mechanism was thus crazing of the glassy polymer [37]. The yield process in glassy amorphous polymers can be described as a stress induced glass-transition. In fact, because PLA Poisson's ratio is less than 0.5 (ν_{PLA} = 0.36) [76], the volume of PLA increases when subjected to tensile stress. Correspondingly, samples experienced important stress whitening, which appeared simultaneously with yielding. Stress whitening is caused by the formation of sizeable microvoids in the polymer matrix due to cavitation and crazes [77]. Crazes can also be initiated inside non-miscible inclusions in the polymer matrix or on the interface between inclusion and polymer in the case of low compatibility. The addition of oil deodorization condensates initiated crazes at stress levels substantially below those of the brittle failure of neat PLA, which propagated perpendicularly to the stretching direction. Morphological analysis of the form and size of inclusions of PODC, C16:0 and C18:1 was done to help interpretation. Figure 4 shows SEM micrographs of [PLA/C16:0], [PLA/C18:1] and [PLA/PODC] 90 wt%/ 10 wt% blends. [PLA/C16:0] blends exhibit rods of about 5 to 10 μm length and 1 to 2 μm width, corresponding to fatty acid crystals. [PLA/C18:1] showed small spherical domains of fatty acids of about 0.5 μm diameters and some aggregates of about 3 to 5 μm diameters. The [PLA/PODC] blend micrograph showed both rods and aggregates of droplets, where the droplets appear to be distributed all around the crystals.

Figure 5 shows optical micrographs in transmission mode of stretched samples under the microscope taken at different percentages of elongation. Many small cracks started appear in neat PLA when approaching the yield peak, which is common for glassy amorphous polymers. Addition of C16:0, *i.e.* rod like crystals, increased both the occurrence and the length of cracks. Cracks quantity upon stretching caused the material to become opaque.

Failure of the blend revealed PLA fibrils. C18:1, *i.e.* small spherical liquid domains, induced fewer but much larger cracks as if their extensibility was eased. PODC, *i.e.* mostly a combination of C16:0 and C18:1 and some minor constituents, showed a high number of cracks but with smaller width as if using only C18:1. The mixture of palmitic acid crystals and liquid inclusions of oleic acid had thus a synergistic effect allowing for efficient craze initiation by the crystals and by cavitation inside the liquid inclusions. The superior performance of the PODC blends seems thus to be linked to the chemical composition in fatty acids and the presence of the minor constituents.

3.4. Role of the chemical composition of deodorization condensates in PLA ductility improvement

A Principal Components Analysis (PCA) was carried out including composition data and physicochemical characteristics of the deodorization condensates and of the PLA samples. Figure 6 shows the principal components projection plot of F1 and F2 of the data set. Only 50% of the total variance in these PLA samples is extracted according to F1 and F2 axes. In fact, scores of formulations containing

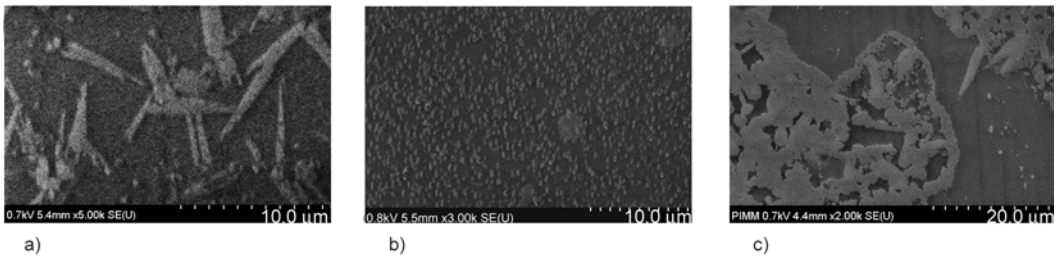

Figure 4. SEM micrographs of (a) C16:0, (b) C18:1 and (c) PODC blends with PLA at 10 wt%

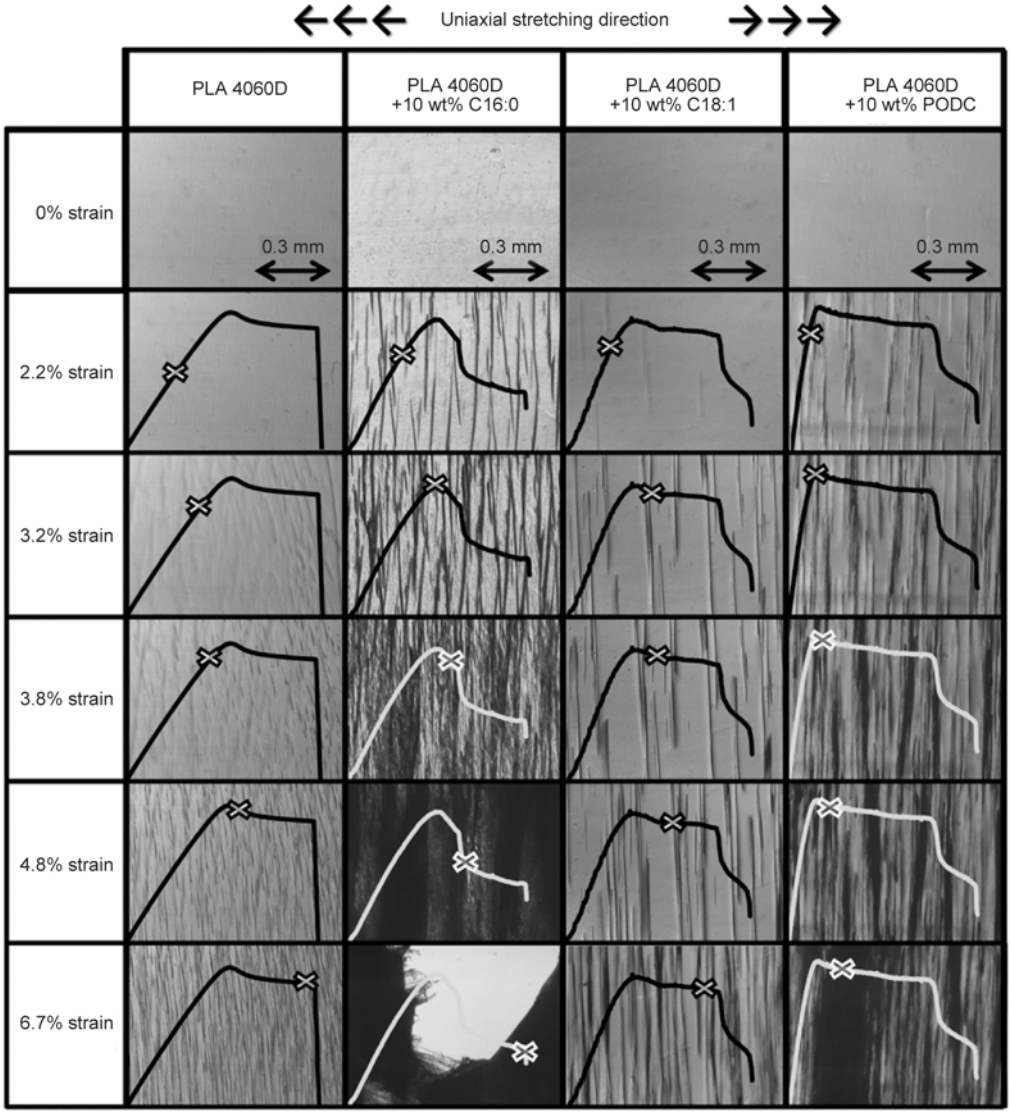

Figure 5. Optical micrographs of uniaxially stretched PLA and PLA blends with free fatty acids (C16:0, C18:1) and palm oil deodorization condensate (PODC) at different strain

squalene, α-tocopherol, HPO, HCO and mixtures of C16:0, C18:1 and HPO are not discriminated. However discrimination of PLA samples containing deodorization condensates of each kind of vegetable oils and according to their respective amount is obtained. Corresponding loadings are plotted in Figure 7. The positive part of F1 axis appears to be mainly governed by the elongation at break and as opposed to its negative part with the T_g. The F2 axis mostly separates fats as a function of the unsaturation and length of their alkyl chains. Looking at the elongation at break improvement, unsaturation of alkyl chains appears to be required, but the lower the ratio, the larger the enhancement was. Medium alkyl chain length, *i.e.* from lauric (C12) to stearic (C18) acid, also tends to be preferable than the long

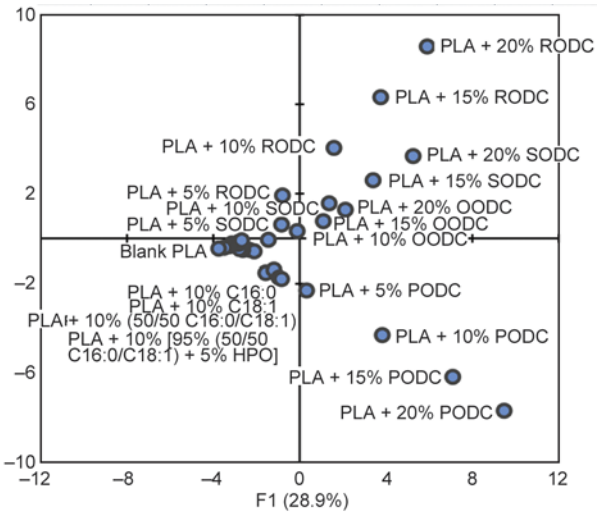

Figure 6. Principal components projection plot of F1 and F2 of the data set

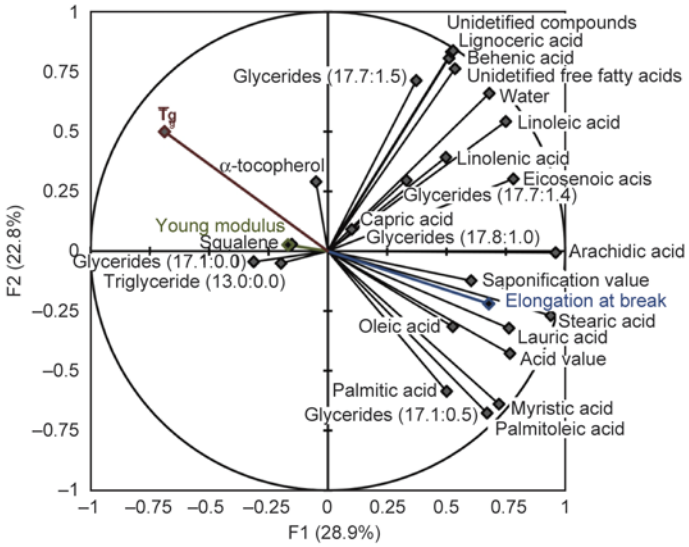

Figure 7. Loadings plot of the Principal Components Analysis of the dataset

ones as behenic (C22) or lignoceric (C24) acids. Both the unsaturation and the length of alkyl chains are main physical factors governing the melting point of fats. One common point is that unsaturation decreases melting points while length increases it. Therefore, efficiency of fats in toughening PLA appeared to be linked to medium melting point properties. A mixture of crystalline and liquid fatty acids at room temperature seemed favorable. This could explain the ability of HCO triglycerides to increase the PLA ductility while HPO did not, although their HSP were similar, as their ability to depress the T_g of PLA. In fact, due to short alkyl chains, HCO triglycerides are waxy at room temperature. The DSC thermogram (Figure 2) shows a broad melting peak going from 8 to 42°C of HCO while it is beyond 55°C for HPO. Literature shows that combining liquid and solid additives can sometimes be effective for PLA [78]. Acid and saponification values are related to the elongation at break improvement (Figure 7). Therefore, the higher the esterified fats and/or the free fatty acid contents, the better the efficiency of the additive. In opposite, unidentified compounds, *i.e.* mostly unsaponifiable compounds, are not favorable to the ductility increase. Therefore, the superiority in toughening abilities of the PODC compared to the alike mixture made of [95 wt% (50 wt% C16:0 + 50 wt% C18:1) + 5 wt% HPO] can be attributed to the complex and favorable mixture of fatty acids having different chain length.

4. Conclusions

By-products of the vegetable oils industry, namely deodorization condensates, were investigated as biobased additives for ductility improvement of PLA. The deodorization condensates improved substantially the elongation at break of PLA up to 180%. The glass transition was merely decreased which brought ductility to the still glassy polymer. The deformation mechanism was efficient craze initiation delaying failure. Most importantly, it was shown that the industrial by-product of the palm oil refinery had superior properties compared to mixtures of fatty acids and vegetable oils because it contained a mixture of fatty acids with melting points below and beyond room temperature. This makes deodorization condensates efficient and low price additives for PLA able to be used in commodity applications such as food packaging.

Acknowledgements

This work was supported by Brodart Packaging and the BIP-ADEME French project CREABioM. The authors greatly thank the laboratory Institut des Corps Gras (ITERG – Bordeaux, France) for its technical support.

References

[1] Auras R., Harte B., Selke S.: An overview of polylactides as packaging materials. Macromolecular Bioscience, **4**, 835–864 (2004).
DOI: 10.1002/mabi.200400043

[2] Auras R. A., Singh S. P., Singh J. J.: Evaluation of oriented poly(lactide) polymers vs. existing PET and oriented PS for fresh food service containers. Packaging Technology and Science, **18**, 207–216 (2005). DOI: 10.1002/pts.692

[3] Petersen K., Væggemose Nielsen P., Bertelsen G., Lawther M., Olsen M., Nilsson N., Mortensen G.: Potential of biobased materials for food packaging. Trends in Food Science and Technology, **10**, 52–68 (1999). DOI: 10.1016/S0924-2244(99)00019-9

[4] Solarski S., Ferreira M., Devaux E., Fontaine G., Bachelet P., Bourbigot S., Delobel R., Coszach P., Murariu M., Da Silva Ferreira A., Alexandre M., Degee P., Dubois P.: Designing polylactide/clay nanocomposites for textile applications: Effect of processing conditions, spinning, and characterization. Journal of Applied Polymer Science, **109**, 841–851 (2008). DOI: 10.1002/app.28138

[5] Zhang J-F., Sun X.: Mechanical and thermal properties of poly(lactic acid)/starch blends with dioctyl maleate. Journal of Applied Polymer Science, **94**, 1697–1704 (2004). DOI: 10.1002/app.21078

[6] Södergård A., Stolt M.: Properties of lactic acid based polymers and their correlation with composition. Progress in Polymer Science, **27**, 1123–1163 (2002). DOI: 10.1016/S0079-6700(02)00012-6

[7] Amass W., Amass A., Tighe B.: A review of biodegradable polymers: Uses, current developments in the synthesis and characterization of biodegradable polyesters, blends of biodegradable polymers and recent advances in biodegradation studies. Polymer International, **47**, 89–144 (1998). DOI: 10.1002/(SICI)1097-0126(1998100)47:2<89::AID-PI86>3.0.CO;2-F

[8] Kaplan D. L.: Biopolymers from renewable resources. Springer, Heidelberg (1998). DOI: 10.1007/978-3-662-03680-8

[9] Lowe C.: Preparation of high molecular weight polyhydroxyacetic ester. U.S. Patent 2668162 A, USA (1954).

[10] Gruber P. R., Hall E. S., Kolstad J. J., Iwen M. L., Benson R. D., Borchardt R. L.: Continuous process for the manufacture of lactide and lactide polymers. U.S. Patent 6326458, USA (2001).

[11] Gruber P. R., Hall E. S., Kolstad J. J., Iwen M. L., Benson R. D., Borchardt R. L.: Continuous process for manufacture of lactide polymers with purification by distillation. U.S. Patent 5357035, USA (1994).

[12] Avérous L.: Monomers, polymers and composites from renewable resources. in 'Polylactic acid: Synthesis, properties and applications' Elsevier, Amsterdam, 433–450 (2008).

[13] Siracusa V., Rocculi P., Romani S., Rosa M. D.: Biodegradable polymers for food packaging: A review. Trends in Food Science and Technology, **19**, 634–643 (2008). DOI: 10.1016/j.tifs.2008.07.003

[14] Liu H., Zhang J.: Research progress in toughening modification of poly(lactic acid). Journal of Polymer Science Part B: Polymer Physics, **49**, 1051–1083 (2011). DOI: 10.1002/polb.22283

[15] Li Y., Shimizu H.: Toughening of polylactide by melt blending with a biodegradable poly(ether)urethane elastomer. Macromolecular Bioscience, **7**, 921–928 (2007). DOI: 10.1002/mabi.200700027

[16] NatureWorks. Technology focus report: Toughened PLA. Ver.3/1/2007 (2007).

[17] Zhang W., Chen L., Zhang Y.: Surprising shape-memory effect of polylactide resulted from toughening by polyamide elastomer. Polymer, **50**, 1311–1315 (2009). DOI: 10.1016/j.polymer.2009.01.032

[18] Byrne F., Ward P. G., Kennedy J., Imaz N., Hughes D., Dowling D. P.: The effect of masterbatch addition on the mechanical, thermal, optical and surface properties of poly(lactic acid). Journal of Polymers and the Environment, **17**, 28–33 (2009). DOI: 10.1007/s10924-009-0119-x

[19] Murariu M., Da Silva Ferreira A., Degée P., Alexandre M., Dubois P.: Polylactide compositions. Part 1: Effect of filler content and size on mechanical properties of PLA/calcium sulfate composites. Polymer, **48**, 2613–2618 (2007). DOI: 10.1016/j.polymer.2007.02.067

[20] Murariu M., Da Silva Ferreira A., Duquesne E., Bonnaud L., Dubois P.: Polylactide (PLA) and highly filled PLA – Calcium sulfate composites with improved impact properties. Macromolecular Symposia, **272**, 1–12 (2008). DOI: 10.1002/masy.200851201

[21] Hughes P. A., Becraft M. L., Opusko S.: Polymeric blend comprising polylactic acid. U.S. Patent 20070255013 A1, USA (2007).

[22] Brulé B., Fine T., Flat J-J., Yasuda M.: Composite based on polylactic acid and polyamide, having improved impact resistance, its manufacturing process and use. World Patent WO2007144543 (2007).

[23] Markarian J.: Biopolymers present new market opportunities for additives in packaging. Plastics, Additives and Compounding, **10**, 22–25 (2008). DOI: 10.1016/S1464-391X(08)70091-6

[24] Jin H-J., Chin I-J., Kim M-N., Kim S-H., Yoon J-S.: Blending of poly(L-lactic acid) with poly(*cis*-1,4-isoprene). European Polymer Journal, **36**, 165–169 (2000). DOI: 10.1016/S0014-3057(99)00041-5

[25] Li Y., Shimizu H.: Improvement in toughness of poly (L-lactide) (PLLA) through reactive blending with acrylonitrile–butadiene–styrene copolymer (ABS): Morphology and properties. European Polymer Journal, **45**, 738–746 (2009). DOI: 10.1016/j.eurpolymj.2008.12.010

[26] McCarthy S. P., Gross R. A., Ma W.: Polylactic acid based blends. U.S. Patent 5883199 A, USA (1999).

[27] Baiardo M., Frisoni G., Scandola M., Rimelen M., Lips D., Ruffieux K., Wintermantel E.: Thermal and mechanical properties of plasticized poly(L-lactic acid). Journal of Applied Polymer Science, **90**, 1731–1738 (2003).
DOI: 10.1002/app.12549

[28] Ljungberg N., Andersson T., Wesslén B.: Film extrusion and film weldability of poly(lactic acid) plasticized with triacetine and tributyl citrate. Journal of Applied Polymer Science, **88**, 3239–3247 (2003).
DOI: 10.1002/app.12106

[29] Murariu M., Da Silva Ferreira A., Alexandre M., Dubois P.: Polylactide (PLA) designed with desired end-use properties: 1. PLA compositions with low molecular weight ester-like plasticizers and related performances. Polymers for Advanced Technologies, **19**, 636–646 (2008).
DOI: 10.1002/pat.1131

[30] Lemmouchi Y., Murariu M., Dos Santos A. M., Amass A. J., Schacht E., Dubois P.: Plasticization of poly(lactide) with blends of tributyl citrate and low molecular weight poly(D,L-lactide)-b-poly(ethylene glycol) copolymers. European Polymer Journal, **45**, 2839–2848 (2009).
DOI: 10.1016/j.eurpolymj.2009.07.006

[31] Wang R. Y., Wan C. Y., Wang S. F., Zhang Y.: Morphology, mechanical properties, and durability of poly (lactic acid) plasticized with di(isononyl) cyclohexane-1,2-dicarboxylate. Polymer Engineering and Science, **49**, 2414–2420 (2009).
DOI: 10.1002/pen.21490

[32] Sierra J., Noriega M., Cardona E., Ospina S.: Relationship between properties, citrate content and postproduction time for a plasticized polylactic acid. in 'Proceedings of ANTEC 2010, Orlando, USA' 127–132 (2010).

[33] Courgneau C., Domenek S., Guinault A., Averous L., Ducruet V.: Analysis of the structure-properties relationships of different multiphase systems based on plasticized poly(lactic acid). Journal of Polymers and the Environment, **19**, 362–371 (2011).
DOI: 10.1007/s10924-011-0285-5

[34] Labrecque L. V., Kumar R. A., Davé V., Gross R. A., McCarthy S. P.: Citrate esters as plasticizers for poly (lactic acid). Journal of Applied Polymer Science, **66**, 1507–1513 (1997).
DOI: 10.1002/(SICI)1097-4628(19971121)66:8<1507::AID-APP11>3.0.CO;2-0

[35] Ljungberg N., Andersson T., Wesslén B.: Film extrusion and film weldability of poly(lactic acid) plasticized with triacetine and tributyl citrate. Journal of Applied Polymer Science, **88**, 3239–3247 (2003).
DOI: 10.1002/app.12106

[36] Yu J., Wang N., Ma X.: Fabrication and characterization of poly(lactic acid)/acetyl tributyl citrate/carbon black as conductive polymer composites. Biomacromolecules, **9**, 1050–1057 (2008).
DOI: 10.1021/bm7012857

[37] Ruellan A., Guinault A., Sollogoub C., Ducruet V., Domenek S.: Solubility factors as screening tools of biodegradable toughening agents of polylactide. Journal of Applied Polymer Science, in press (2015).
DOI: 10.1002/APP.42476

[38] Kulinski Z., Piorkowska E., Gadzinowska K., Stasiak M.: Plasticization of poly(L-lactide) with poly(propylene glycol). Biomacromolecules, **7**, 2128–2135 (2006).
DOI: 10.1021/bm060089m

[39] Kulinski Z., Piorkowska E.: Crystallization, structure and properties of plasticized poly(L-lactide). Polymer, **46**, 10290–10300 (2005).
DOI: 10.1016/j.polymer.2005.07.101

[40] Hu Y., Hu Y. S., Topolkaraev V., Hiltner A., Baer E.: Crystallization and phase separation in blends of high stereoregular poly(lactide) with poly(ethylene glycol). Polymer, **44**, 5681–5689 (2003).
DOI: 10.1016/S0032-3861(03)00609-8

[41] Jacobsen S., Fritz H. G.: Plasticizing polylactide – The effect of different plasticizers on the mechanical properties. Polymer Engineering and Science, **39**, 1303–1310 (1999).
DOI: 10.1002/pen.11517

[42] Martin O., Averous L.: Poly(lactic acid): Plasticization and properties of biodegradable multiphase systems. Polymer, **42**, 6209–6219 (2001).
DOI: 10.1016/S0032-3861(01)00086-6

[43] Pillin I., Montrelay N., Grohens Y.: Thermo-mechanical characterization of plasticized PLA: Is the miscibility the only significant factor? Polymer, **47**, 4676–4682 (2006).
DOI: 10.1016/j.polymer.2006.04.013

[44] Sheth M., Kumar R. A., Davé V., Gross R. A., McCarthy S. P.: Biodegradable polymer blends of poly(lactic acid) and poly(ethylene glycol). Journal of Applied Polymer Science, **66**, 1495–1505 (1997).
DOI: 10.1002/(SICI)1097-4628(19971121)66:8<1495::AID-APP10>3.0.CO;2-3

[45] Martino V., Ruseckaite R., Jiménez A.: Thermal and mechanical characterization of plasticized poly(*L*-lactide-*co*-*D,L*-lactide) films for food packaging. Journal of Thermal Analysis and Calorimetry, **86**, 707–712 (2006).
DOI: 10.1007/s10973-006-7897-3

[46] Martino V. P., Jiménez A., Ruseckaite R. A.: Processing and characterization of poly(lactic acid) films plasticized with commercial adipates. Journal of Applied Polymer Science, **112**, 2010–2018 (2009).
DOI: 10.1002/app.29784

[47] Ljungberg N., Wesslén B.: Thermomechanical film properties and aging of blends of poly(lactic acid) and malonate oligomers. Journal of Applied Polymer Science, **94**, 2140–2149 (2004).
DOI: 10.1002/app.21100

[48] Ren Z., Dong L., Yang Y.: Dynamic mechanical and thermal properties of plasticized poly(lactic acid). Journal of Applied Polymer Science, **101**, 1583–1590 (2006).
DOI: 10.1002/app.23549

[49] Rahman M., Brazel C. S.: The plasticizer market: An assessment of traditional plasticizers and research trends to meet new challenges. Progress in Polymer Science, **29**, 1223–1248 (2004).
DOI: 10.1016/j.progpolymsci.2004.10.001

[50] Robertson M. L., Chang K., Gramlich W. M., Hillmyer M. A.: Toughening of polylactide with polymerized soybean oil. Macromolecules, **43**, 1807–1814 (2010).
DOI: 10.1021/ma9022795

[51] Gramlich W. M., Robertson M. L., Hillmyer M. A.: Reactive compatibilization of poly(l-lactide) and conjugated soybean oil. Macromolecules, **43**, 2313–2321 (2010).
DOI: 10.1021/ma902449x

[52] Ali F., Chang Y-W., Kang S. C., Yoon J. Y.: Thermal, mechanical and rheological properties of poly (lactic acid)/epoxidized soybean oil blends. Polymer Bulletin, **62**, 91–98 (2009).
DOI: 10.1007/s00289-008-1012-9

[53] Xu Y-Q., Qu J-P.: Mechanical and rheological properties of epoxidized soybean oil plasticized poly(lactic acid). Journal of Applied Polymer Science, **112**, 3185–3191 (2009).
DOI: 10.1002/app.29797

[54] Xiong Z., Yang Y., Feng J., Zhang X., Zhang C., Tang Z., Zhu J.: Preparation and characterization of poly(lactic acid)/starch composites toughened with epoxidized soybean oil. Carbohydrate Polymers, **92**, 810–816 (2012).
DOI: 10.1016/j.carbpol.2012.09.007

[55] Al-Mulla E. A. J., Suhail A. H., Aowda S. A.: New biopolymer nanocomposites based on epoxidized soybean oil plasticized poly(lactic acid)/fatty nitrogen compounds modified clay: Preparation and characterization. Industrial Crops and Products, **33**, 23–29 (2010).
DOI: 10.1016/j.indcrop.2010.07.022

[56] Silverajah V. S. G., Ibrahim N. A., Zainuddin N., Yunus W., Abu Hassan H.: Mechanical, thermal and morphological properties of poly(lactic acid)/epoxidized palm olein blend. Molecules, **17**, 11729–11747 (2012).
DOI: 10.3390/molecules171011729

[57] Silverajah V. S. G., Ibrahim N. A., Yunus W., Abu Hassan H., Woei C. B.: A comparative study on the mechanical, thermal and morphological characterization of poly(lactic acid)/epoxidized palm oil blend. International Journal of Molecular Sciences, **13**, 5878–5898 (2012).
DOI: 10.3390/ijms13055878

[58] Al-Mulla E. A. J., Yunus W. M. Z. W., Ibrahim N. A. B., Ab Rahman M. Z.: Properties of epoxidized palm oil plasticized polytlactic acid. Journal of Materials Science, **45**, 1942–1946 (2010).
DOI: 10.1007/s10853-009-4185-1

[59] NatureWorks: Technology focus report: Polylactic acid containing fillers and fibres (2007).

[60] Bitinis N., Fortunati E., Verdejo R., Bras J., Kenny J. M., Torre L., Lopez-Manchado M. A.: Poly(lactic acid)/natural rubber/cellulose nanocrystal bionanocomposites. Part II: Properties evaluation. Carbohydrate Polymers, **96**, 621–627 (2013).
DOI: 10.1016/j.carbpol.2013.03.091

[61] Yuan D., Chen K., Xu C., Chen Z., Chen Y.: Cross-linked bicontinuous biobased PLA/NR blends via dynamic vulcanization using different curing systems. Carbohydrate Polymers, **113**, 438–445 (2014).
DOI: 10.1016/j.carbpol.2014.07.044

[62] Thepthawat A., Srikulkit K.: Improving the properties of polylactic acid by blending with low molecular weight polylactic acid-*g*-natural rubber. Polymer Engineering and Science, **54**, 2770–2776 (2014).
DOI: 10.1002/pen.23835

[63] Ayutthaya W. D. N., Poompradub S.: Thermal and mechanical properties of poly(lactic acid)/natural rubber blend using epoxidized natural rubber and poly (methyl methacrylate) as *co*-compatibilizers. Macromolecular Research, **22**, 686–692 (2014).
DOI: 10.1007/s13233-014-2102-1

[64] Hughes J., Thomas R., Byun Y., Whiteside S.: Improved flexibility of thermally stable poly-lactic acid (PLA). Carbohydrate Polymers, **88**, 165–172 (2012).
DOI: 10.1016/j.carbpol.2011.11.078

[65] Bradley J-C., Lang A., Williams A.: Jean-Claude Bradley double plus good (highly curated and validated) melting point dataset (2014).
DOI: 10.6084/m9.figshare.1031638

[66] Vereeckeen J., Foubert I., Meeussen W., Lesaffer A., Dewettinck K.: Fat structuring with partial acylglycerols: Effect on solid fat profiles. European Journal of Lipid Science and Technology, **111**, 259–272 (2009).
DOI: 10.1002/ejlt.200800151

[67] Sato K.: Kinetic aspects in polymorphic crystallization and transformation of fats mixed and dispersed systems. in 'Physical properties of fats, oils, and emulsifiers' (ed.: Widlak N.) The American Oil Chemists Society, Champaign, 33–48 (1999).

[68] Van Krevelen D. W., Te Nijenhuis K.: Cohesive properties and solubility. in 'Properties of polymers' (eds.: Van Krevelen D. W., Te Nijenhuis K.) Elsevier, Amsterdam, 189–228 (2009).

[69] van Krevelen D. W.: Chemical structure and properties of coal. XXVIII. Coal constitution and solvent extraction. Fuel, **44**, 229–242 (1965).

[70] Van Krevelen D. W., Hoftyzer P. J.: Practical evaluation of the [η]–*M* relationship. III. Estimation of the exponent A. Journal of Applied Polymer Science, **11**, 2189–2200 (1967).
DOI: 10.1002/app.1967.070111109

[71] Abbott S. J.: Chemical compatibility of poly (lactic acid): A practical framework using hansen solubility parameters. in 'Poly(lactic acid): Synthesis, structures, properties, processing, and applications' (eds.: Auras R., Lim L. T., Selke S., Tsuji H.) Wiley, Hoboken, 83–93 (2010).

[72] Robertson M. L., Paxton J. M., Hillmyer M. A.: Tough blends of polylactide and castor oil. ACS Applied Materials and Interfaces, **3**, 3402–3410 (2011).
DOI: 10.1021/am2006367

[73] Jacobsen S., Fritz H. G.: Plasticizing polylactide – The effect of different plasticizers on the mechanical properties. Polymer Engineering and Science, **39**, 1303–1310 (1999).
DOI: 10.1002/pen.11517

[74] Manzanarez-López F., Soto-Valdez H., Auras R., Peralta E.: Release of α-tocopherol from poly(lactic acid) films, and its effect on the oxidative stability of soybean oil. Journal of Food Engineering, **104**, 508–517 (2011).
DOI: 10.1016/j.jfoodeng.2010.12.029

[75] Hwang S. W., Shim J. K., Selke S. E. M., Soto-Valdez H., Matuana L., Rubino M., Auras R.: Poly(L-lactic acid) with added α-tocopherol and resveratrol: Optical, physical, thermal and mechanical properties. Polymer International, **61**, 418–425 (2012).
DOI: 10.1002/pi.3232

[76] Jamshidian M., Tehrany E. A., Imran M., Jacquot M., Desobry S.: Poly-lactic acid: Production, applications, nanocomposites, and release studies. Comprehensive Reviews in Food Science and Food Safety, **9**, 552–571 (2010).
DOI: 10.1111/j.1541-4337.2010.00126.x

[77] Lampman S.: Fracture and fractography. in 'Characterization and failure analysis of plastics' (ed.: Lampman S.) ASM International, Materials Park, 404–416 (2003).

[78] Notta-Cuvier D., Odent J., Delille R., Murariu M., Lauro F., Raquez J. M., Bennani B., Dubois P.: Tailoring polylactide (PLA) properties for automotive applications: Effect of addition of designed additives on main mechanical properties. Polymer Testing, **36**, 1–9 (2014).
DOI: 10.1016/j.polymertesting.2014.03.007

eXPRESS Polymer Letters Vol.9, No.12 (2015) 1104–1118
Available online at www.expresspolymlett.com
DOI: 10.3144/expresspolymlett.2015.99

Multifunctional nanocomposites of poly(vinylidene fluoride) reinforced by carbon nanotubes and magnetite nanoparticles

C. Tsonos[1,2*], *C. Pandis*[3], *N. Soin*[2], *D. Sakellari*[4], *E. Myrovali*[4], *S. Kripotou*[3], *A. Kanapitsas*[1], *E. Siores*[2,5]

[1]Electronics Engineering Department, Technological Educational Institute (TEI) of Sterea Ellada, 35100 Lamia, Greece
[2]Institute for Materials Research and Innovation (IMRI), University of Bolton, Deane Road, BL3 5AB Bolton, UK
[3]Physics Department, National Technical University of Athens, Zografou 15780 Athens, Greece
[4]Department of Physics, Aristotle University of Thessaloniki, 54124 Thessaloniki, Greece
[5]Technological Educational Institute of Athens, 12210 Athens, Greece

Received 12 May 2015; accepted in revised form 27 July 2015

Abstract. In the present study, the effect of nano magnetite (Fe_3O_4) content on structural, dielectric/electrical, magnetic and thermal properties of poly(vinylidene fluoride)/carbon nanotubes matrix, is investigated. Nanocomposite films of polyvinylidene fluoride, carbon nanotubes and Fe_3O_4 nanoparticles were prepared by the twin screw compounding method. Fe_3O_4, as magnetic inclusions was incorporated into the composites with carbon nanotubes loadings well above the percolation threshold, where conductive networks were formed. Magnetic characterization revealed the ferrimagnetic behavior of nanocomposites, with saturation magnetization values depending on magnetite content. Results obtained from the analysis of Fourier Transform Infrared Spectroscopy (FTIR), X-ray Diffraction (XRD) and Differential Scanning Calorimetry (DSC) techniques were very informative for the study of the polymorphism and crystallinity in PVDF. The incorporation of Fe_3O_4 inclusions in PVDF/CNT matrix, gradually increase both electrical conductivity and dielectric permittivity up to 10 wt% Fe_3O_4 content, while at the higher Fe_3O_4 content (15 wt%) reduced values were obtained. This behavior, at higher Fe_3O_4 content, should be possible related to the insulating and barrier role of Fe_3O_4 nanoparticles.

Keywords: *nanocomposites, dielectric properties, thermal properties*

1. Introduction

A great challenge in materials engineering is the production of multifunctional nanocomposites, which combine inexpensive materials with the ease of processing at large scale. Polyvinylidene fluoride (PVDF), is a semi-crystalline polymer having remarkable thermal stability, good chemical resistance and extraordinary pyroelectric and piezoelectric properties among polymers [1]. These properties combined with its high elasticity, relative transparency and ease of processing, make this material suitable for various technological applications [2]. PVDF shows a complex structure and it can exhibit five distinct crystalline phases related to different chain conformations, known as α, β, γ, δ and ε phases [3, 4]. Amongst them, β phase is the most active phase electrically and, to a lesser extent, γ phase. Thus, the use of PVDF as matrix in nanocomposites is one of the key parameters for a wide range of applications. Adding nanoparticles to a matrix such as PVDF can enhance its conductive performance and provide enhanced responses by capitalizing on the nature and properties of the nanoscale filler. The final properties of these nanocomposites mainly depend on

*Corresponding author, e-mail: tsonos@teilam.gr

parameters such as filler size, method of preparation and the dispersion of nanoparticles into the polymer matrix [5–7].

Among the nanosized fillers, iron oxides have become of long standing interest, because of their diverse variety of applications in electronic, magnetic, optical, and mechanical devices [8]. Iron oxide magnetic nanoparticles are one of most studied nanomaterials, especially due to their magnetic properties, biocompatibility, biodegradability and low cost. Magnetoelectric materials are a relatively new class of materials, where their magnetic nanoparticles and polymer matrix allow a variety of applications in electronic, magnetic, optical, and mechanical devices [9, 10]. Magnetoelectric composites have become one of the most active research fields in the areas of materials science and engineering in recent years.

Fe_3O_4 nanoparticles and their composites have attracted enhanced attention and their critical size for superparamagnetic to ferrimagnetic transition has been determined to be near 30nm at room temperature [11]. PVDF/Fe_3O_4 composites exhibit superparamagnetic behavior with the presence of Fe_3O_4 nanoparticles, while the maximum for saturation magnetization was found to be 30.8 emu/g [12]. In composite films of PVDF/Fe_3O_4 which are fabricated by solvent casting method, it was found that the inclusion of nanosized Fe_3O_4 significantly enhances the crystallinity of PVDF and the β phase content [13]. Also, increased crystallinity enhances the ferrimagnetic properties of these composites whereas the latter improves the thermal stability and polarization effects. In another similar system, differential scanning calorimetry measurements revealed that the crystallinity of PVDF decreased with the addition of Fe_3O_4, while the conductivity of the composite films increased with increase in Fe_3O_4 content [14]. Fe_3O_4 nanoparticles were found to form some 50 nm–5 μm conglomerates in the PVDF matrices while the size of these conglomerates increased with the increase in Fe_3O_4 content [15].

Also, much work has been done in order to investigate the effect of carbon nanotubes (CNT) addition on the crystallization, the mechanical, electrical and thermal properties of PVDF/CNT composites. Furthermore the addition of a third phase in the form of inorganic inclusions has been explored with the aim to enhance the multifunctionality of the prepared ternary composites. For example, in very recent works on ternary PVDF/CNT composites it has been shown that the addition of graphene oxide enhances the thermal conductivity [16], while $BaTiO_3$ incorporation greatly increases the dielectric permittivity [17].

The present work deals with a novel three-phase PVDF based system with CNT and nanosized Fe_3O_4 as inclusions. To the best of our knowledge, there is no systematic work on PVDF/CNT/Fe_3O_4 ternary composites in the literature. This system comprises a new type of multifunctional materials that combine the ferroelectric and piezoelectric properties of PVDF with the electrical properties of CNT and the magnetic properties of Fe_3O_4. Fe_3O_4 nanoparticles were incorporated into the composites in various contents with CNT loadings well above the percolation threshold, where stable conductive networks were formed [18, 19]. The effect of Fe_3O_4 nanoparticles on PVDF/CNT blends, and especially the insulating and barrier role of these inclusions on both, dielectric response and conductive network formation of PVDF/CNT matrix, was investigated in this study.

2. Experimental details

2.1. Materials

Samples were composed of PVDF with suitable additives (CNT, Fe_3O_4) in the desired loading range of 4 to 19 wt% (total). More specifically, CNT content was kept constant and equal to 4 wt% while Fe_3O_4 contents were 0, 5, 10 and 15 wt%. PVDF was compounded with the nanofillers using a lab scale twin screw compounder (Thermo Scientific) with counter rotating screws. A PVDF homopolymer, SOLEF 1008 (from Solvay Solexis) was used for the production of samples. The polymer had melt flow index (MFI) of 8 g/10 min at 230°C (under a load of 2.16 kg). Multiwalled CNT were obtained from Cheap Tubes Inc. with a mean outer diameter of <10 nm, length of 10–30 μm, purity >90% (by wt%) and an ash content of less than 1.5 wt%. No further purification or acid treatment of the CNT was carried out and the samples were used as-received. Fe_3O_4 nanopowder was obtained from Aldrich with average particle size <50 nm and purity >98%. The PVDF pellets (500 grams) were mixed with the suitable weight of additive and then passed through the twin screw extruder. Extruder temperature profile was set at 150°C (at hopper end) with 10°C incremental changes across the heated barrel (165, 175, 185, 195°C) with a final temperature of 195°C at the die head. Temperature profile was set in such a manner that the polymer started to melt in the mid-

dle of the barrel and then by the time it reached to the die head, the viscosity of it was reduced significantly. Polymer pellet-additive mixture was fed to the counter rotating screw at 13% feed rate and was moved across the length of the screw at 40% torque corresponding to 350 rpm screw speed. Monofilament obtained from the die head was then passed through a cooling bath using a set of rollers from where it was passed onto a chopping unit which made homogeneous pellets (~ 5 mm long) from it. The pellets were then dried overnight at 75°C to remove the adsorbed water before further processing. The samples were pressed at a pressure of 40 kg/cm^2 for duration of 2 min 30 sec and then allowed to cool down at the same pressure using a cold press which rapidly cooled down the samples to room temperature in approximately 2 mins. The final sample weight was approximately 48 g, with the rest of additive mix lost to overflow of the polymer to the outside of the mould. The twin screw compounding enabled better quality of mixing at low melt temperatures and hence the material degradation was avoided.

2.2. Characterization

Morphology was studied by field emission Scanning Electron Microscopy (FE-SEM) using FEI Nova nanoSEM 230 operating in high vacuum mode. Samples were cryofractured using liquid nitrogen and their cross section was examined using an accelerating voltage of 5 kV. The size of the particles from the SEM micrographs was measured using ImageJ software.

FTIR analysis was carried out using Thermo Scientific IS10 Nicolet FTIR spectrometer coupled with smart iTR accessory. A total of 64 scans at a resolution of ±2 cm^{-1} were taken during spectrum acquisition. Vendor provided OMINIC software was used to analyze the results and calculations of the beta phase.

XRD analysis of samples was performed at room temperature using X'Pert MRD (Panalytical) between the 2θ range of 5–40° at a scan speed of 0.02°/s. A CuKα radiation (λ = 0.154 nm) source performing at 45 kV and 40 mA was used.

Thermal transitions (crystallization/melting) were studied by DSC analysis carried out in nitrogen atmosphere in the temperature range from 20 to 200°C using a Q20 (TA instrument) apparatus. The weight of the measured samples was kept constant at ~5 mg. Heating and cooling rates were fixed to 10°C/min.

Magnetic measurements were performed, using Vibrating Sample Magnetometer (VSM) – Oxford 1.2 H/CF/HT at maximum applied fields of 1 T. For each sample magnetization versus applied field was recorded at room temperature.

Electrical/dielectric properties were studied by means of Dielectric Relaxation Spectroscopy (DRS) technique using Alpha analyzer in combination with a Quatro cryosystem for temperature control, both supplied by Novocontrol. Samples of 1 mm thickness were placed between two brass electrodes of 20 mm diameter and inserted as a capacitor in a Novocontrol sample cell. Golden electrodes were sputtered (using a sputter coater EMS 550) on both sides of the samples to assure good electrical contact between the sample and the gold-plated capacitor plates. The complex dielectric permittivity was recorded and measured in a broad frequency ranged from 1 to 10^6 Hz.

3. Results and discussion

3.1. Morphology

Figure 1 shows representative SEM micrographs of cryo-fractured surfaces obtained at magnification of 80 000×. Figure 1a shows the micrograph of pure PVDF for comparative analysis. The yellow squares for the samples containing CNT highlight the presence of several individual CNTs in the obtained micrographs (Figure 1b, a–c), indicative of a lack of agglomeration and presence of a good dispersion. It is important to note that the fractured samples were prepared using cryo-fracture and not the tensile fracture, which can sometimes lead to the fibrillation of PVDF and can be often misinterpreted as the CNT. Similarly, the green circles are indicative of the presence of Fe_3O_4 particles, which again show a good distribution across the PVDF matrix without significant agglomeration, having a mean diameter in the range of 50–100 nm. Furthermore, on increasing the Fe_3O_4 particle concentration to 15 wt% (sample PVDF/CNT/$(Fe_3O_4)_{15\%}$) larger agglomerates of Fe_3O_4 were observed (Figure 1d).

3.2. FTIR measurements

To calculate relative amount of the β phase in the composite film, FTIR tests for the pure PVDF and nanocomposites were undertaken and results are shown in Figure 2a. The polar β phase is technolog-

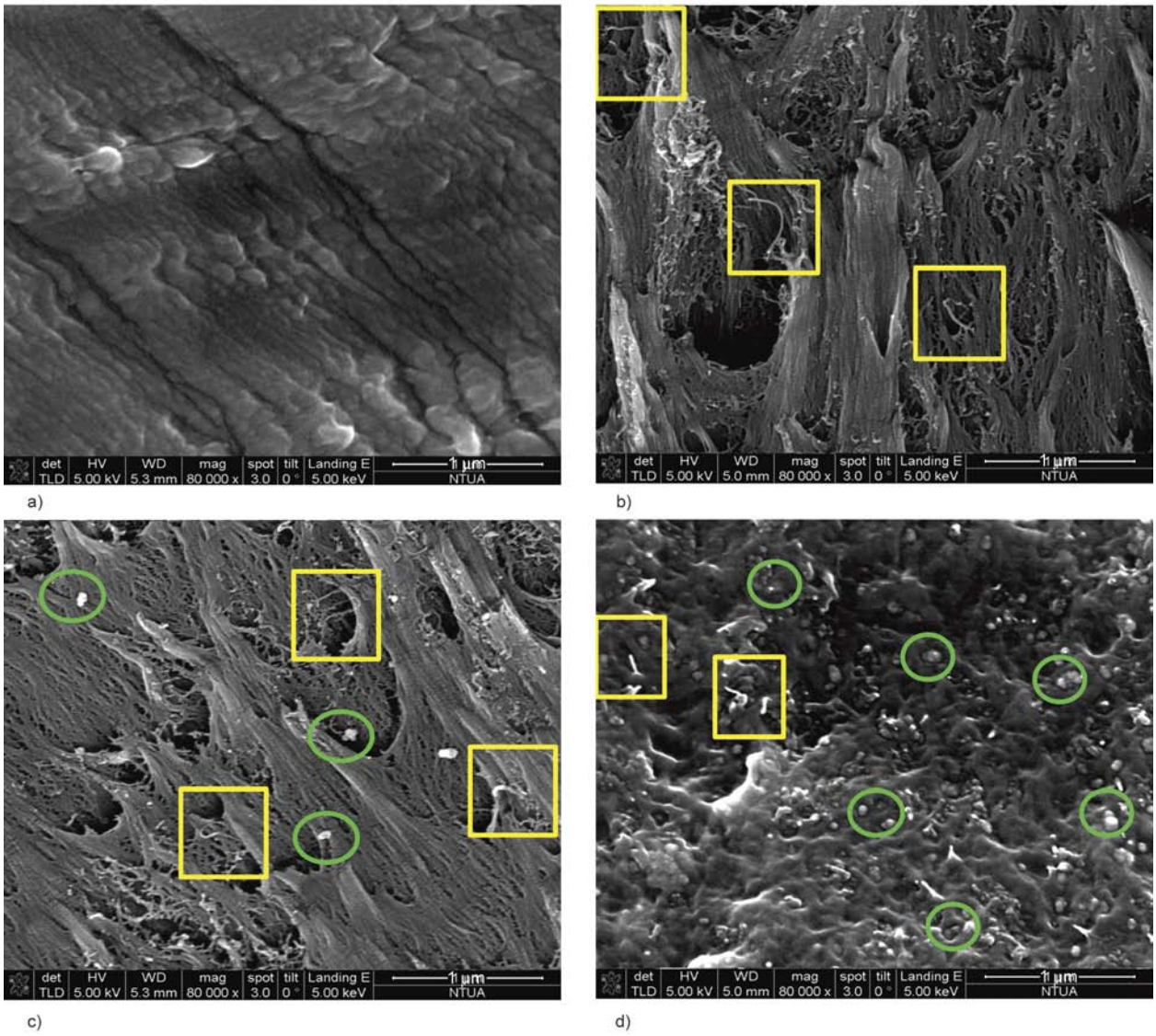

Figure 1. FE-SEM micrographs obtained at 80 000× magnification: (a) pure PVDF, (b) PVDF/CNT, (c) PVDF/CNT/$(Fe_3O_4)_{5\%}$, (d) PVDF/CNT/$(Fe_3O_4)_{15\%}$

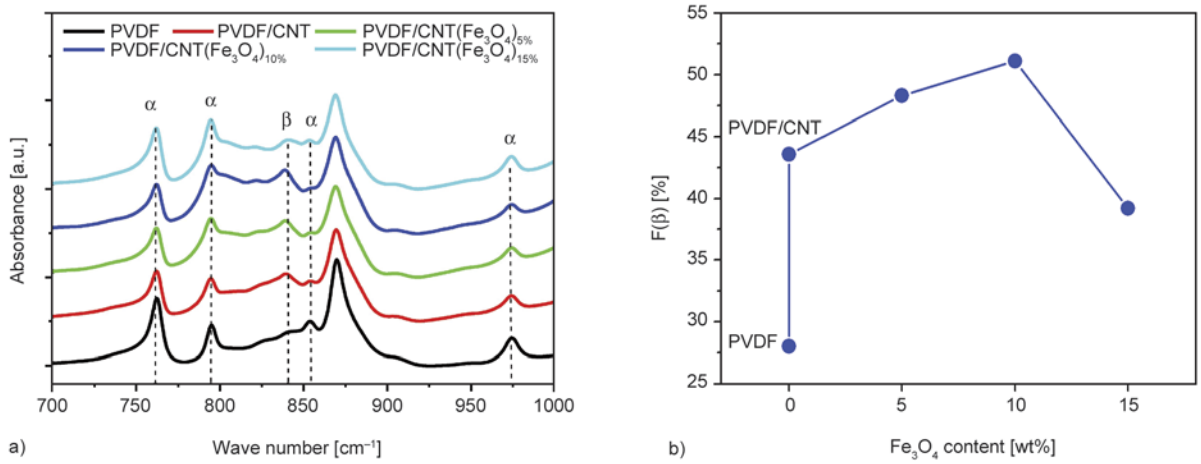

Figure 2. (a) FTIR spectra for the PVDF nanocomposites, (b) β phase content for the PVDF nanocomposites

ically most interesting as it shows the largest piezoelectric, ferroelectric and pyroelectric coefficients, as well as a high dielectric constant. Various characteristic absorption bands which correspond to the crystalline phases of PVDF systems have been reported [20–22], and some of these are present in

Figure 1a. Absorbance at 612, 760, 795, 853 and 974 cm^{-1}, correspond to the β phase, while absorbances at 511, 840, 878 and 1279 cm^{-1} corresponded to the β phase. The content fraction of phase in each sample of PVDF nanocomposites, $F(\beta)$, was calculated according to Equation (1) [23–25]:

$$F(\beta) = \frac{X_\beta}{X_\alpha + X_\beta} = \frac{A_\beta}{1.26A_\alpha + A_\beta} \quad (1)$$

where X_α and X_β are crystalline mass fractions of the α and β phases and A_α, A_β correspond to their absorbance at 760 and 840 cm^{-1} respectively. This relation gives the relative amount of the α and β phases in composites assuming that only these phases are present and has been used extensively in the literature. As shown in Figure 2b, the β content calculated for pristine PVDF samples and PVDF/CNT composite shows a huge increase from approximately 28 to 44%, signifying the effect of CNT in promoting the β phase crystallization. Similar behaviour has been seen in PVDF based composites prepared by melt compounding, in which the incorporation of CNT produced transformation of the phase into β phase [26, 27]. Furthermore, the incorporation of Fe_3O_4 nanoparticles in PVDF/CNT matrix slightly and gradually increases the β phase up to a maximum value of 51% for the sample with 10 wt% Fe_3O_4, while at the highest Fe_3O_4 content (i.e. 15 wt%) phase decreases to the value of 39%. Adding Fe_3O_4 nanoparticles was found to result also in α to β phase transformation in PVDF matrix [28, 29]. From these results it seems that it is mainly CNT that promote the formation of phase in PVDF nanocomposites, while the influence of Fe_3O_4 is less but not insignificant.

3.3. XRD analysis

Figure 3a shows X-ray diffractograms of pristine PVDF and PVDF/CNT nanocomposites with 5, 10, and 15 wt% Fe_3O_4 in the 2θ range between 5–40°. The well-known diffraction peaks of α phase of PVDF appearing at 2θ = 17.8, 18.5, 20 and 26.8°, are assigned to the lattice planes of (100), (020), (110) and (021) respectively [30]. Furthermore, for samples containing Fe_3O_4 the diffraction peak at 30.6° are assigned to Fe_3O_4 crystalline plane of (220) [13]. In fact, with the increase in the addition of Fe_3O_4, the peak becomes increasingly prominent. Interestingly, when CNT are incorporated in the PVDF

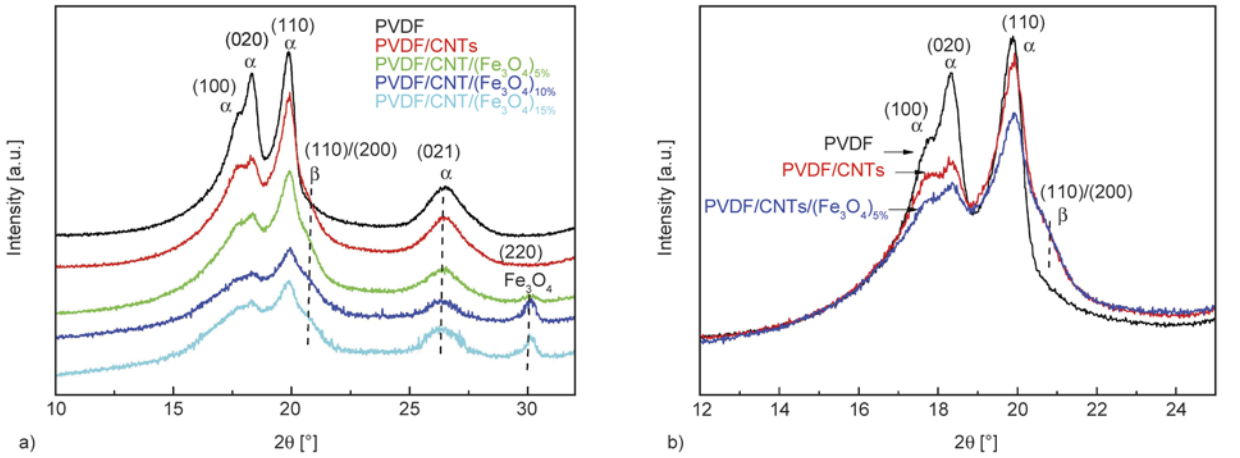

Figure 3. (a) XRD patterns of pure PVDF and PVDF nanocomposites with CNT and Fe_3O_4, (b) zoom of XRD patterns of pure PVDF and nanocomposites showing the existence of β phase for the nanocomposites containing CNT

Table 1. Results from DSC and XRD analysis

Sample	DSC						XRD
	First heating		Second heating			First cooling	
	T_m [°C]	T_{m2} [°C]	T_m [°C]	ΔH [J/g]	X_c [%]	T_c [°C]	X_c [%]
PVDF	173.0	165.5	171.4	50.6	48	137.70	49±2
PVDF/CNT	173.2	168.6	173.3	50.8	49	148.50	51±2
PVDF/CNT/$(Fe_3O_4)_{5\%}$	172.9	168.5	173.2	50.4	48	148.50	44±2
PVDF/CNT/$(Fe_3O_4)_{10\%}$	173.0	168.2	173.2	40.9	39	148.40	37±3
PVDF/CNT/$(Fe_3O_4)_{15\%}$	172.9	168.5	172.9	44.2	42	150.14	43±3

matrix, the appearance of a shoulder at 20.6°, attributed to the (110)/(200) planes of the β phase is observed [31]. The above can be seen more clearly in Figure 3b where a zoom in the 2θ range between 12–25° is presented. These findings suggest that the presence of CNT induces the formation of β phase [32], in accordance with FTIR analysis. For the determination of the crystallinity from the XRD profiles, the following equation has been used [33], $X_c = I_c/(I_c + I_\alpha)$, where I_c and I_α are the integrated intensities scattered by the crystalline and the amorphous phases, respectively. The degree of crystallinity of PVDF in the nanocomposites has been evaluated from diffractograms and reported in Table 1.

3.4. Thermal properties

During the first heating scan a double melting peak is observed in all studied samples (Figure 4a). For pristine PVDF a main peak around 173°C and a shoulder around 166°C were observed. The existence of double melting peak is generally attributed to the presence of crystallites of different thickness, variety of crystallites perfection, re-melting of crystallites formed during heating or existence of polymorphism [13]. When the samples were cooled from the melt, a single crystallization peak was found and the crystallization temperature, T_c, of pure PVDF was observed at 138°C. In the nanocomposites, a narrower crystallization peak and a shift of crystallization temperature T_c to higher temperatures (~10°C) compared to pure PVDF was detected. Interestingly, T_c was found to be independent of the Fe_3O_4 concentration and their effect is less pronounced as can be seen in Figure 4c. The increase of T_c upon addition of CNT is a clear indication of their essence as nucleating agents promoting heterogeneous crystallization, a feature commonly observed in polymer/CNT nanocomposites [34, 35], while narrowing of the crystallization peak implies a narrower crystallite size distribution [36].

During the second heating scan and after erasing the thermal history of each sample, a single melting peak, independent of the filler concentration, was observed around 173°C, slightly higher in the nanocomposites compared to pure PVDF (Figure 4b). Melting (T_m) and crystallization (T_c) temperatures together with the melting enthalpies (ΔH_m) recorded during second heating scan are reported in Table 1. The degree of crystallinity X_c of PVDF is calculated from Equation (2):

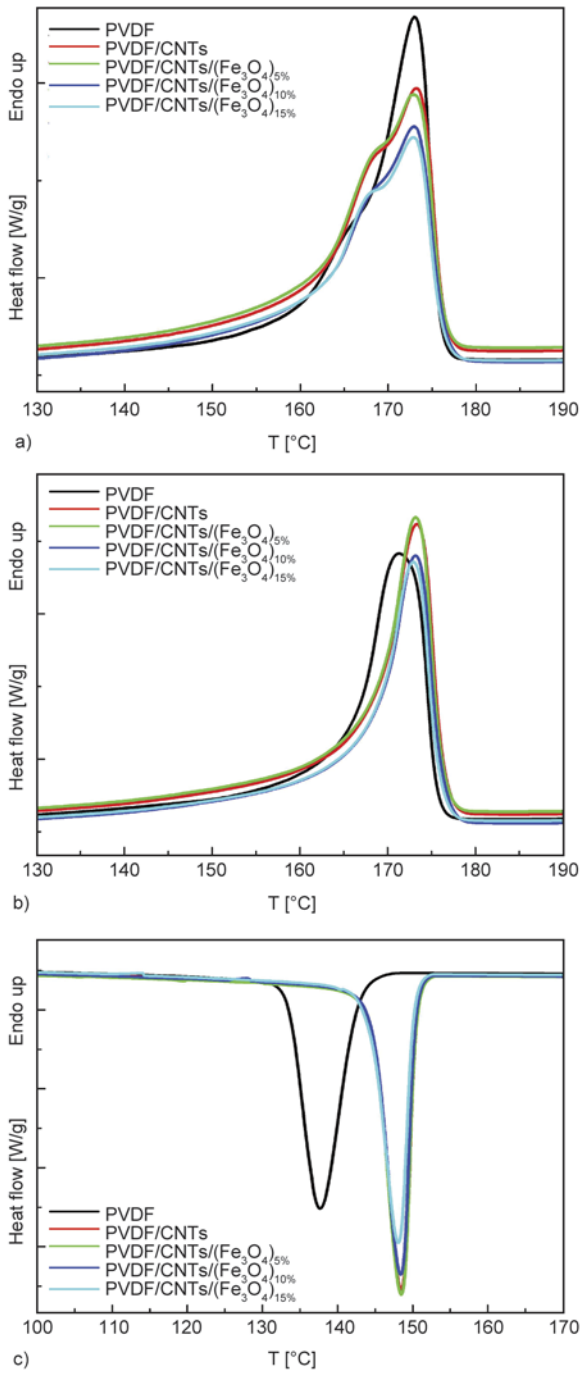

Figure 4. (a) DSC thermograms showing melting during first heating and (b) second heating scan, and (c) crystallization during cooling

$$X_c\,[\%] = \frac{\Delta H_m}{(1-\varphi)\Delta H_0}\cdot 100 \qquad (2)$$

where ΔH_0 is the melting enthalpy for 100% β crystalline PVDF and φ is the total weight fraction of fillers in nanocomposites. ΔH_0 was taken equal to 104.5 J/g. [37]. The degree of crystallinity is practically unaffected by the addition of CNT and for the lowest concentration sample of Fe_3O_4 particles. For

higher Fe_3O_4 content, a decrease of the degree of crystallinity was observed. A similar reduction in the crystallinity has been observed by other authors [14, 15]. This reduction in the crystallinity can be attributed to the inhibition effect of Fe_3O_4 addition on polymer crystal formation, similar to what has been observed with various other inorganic fillers. The above results are in accordance with those obtained from XRD analysis.

It should be noted that while DSC could be very accurate in the evaluation of the degree of crystallinity in PVDF, it could not be used in our case to distinguish between different polymorphs, in particular between α and β phase. The melting temperatures of crystallite phases are very close and both appear in the range 167–172°C [24]. In addition, when analyzing DSC results in PVDF nanocomposites, further caution must be taken for ascribing the melting peaks to either α or β phase, and DSC should be considered as complementary technique to FTIR or XRD, as its features are not only dependent on the crystalline phase, but also affected by crystalline defects which are particularly enhanced by the presence of nanofillers [30]. However, DSC is used to exclude the existence of γ phase as no melting peak has been observed at higher temperatures around 179–180°C [38]. Combination of results analysis of all three techniques (FTIR, XRD and DSC) are very informative for the study of the polymorphism and crystallinity in PVDF. FTIR and XRD allowed identifying the different crystalline phases giving a clear evidence of the enhancement of β phase of PVDF when CNT are incorporated, while DSC was used to evaluate the degree of crystallinity.

3.5. Magnetic characterization

Figure 5a presents hysteresis loops as recorded at room temperature for polymer nanocomposites, including CNT and Fe_3O_4 nanoparticles. The hysteresis loops confirm the ferromagnetic behavior of nanocomposites, which is attributed to magnetic nanoparticle content [13]. This magnetic behaviour is also observed in other similar composites systems [14]. Moreover, by increasing magnetite (Fe_3O_4) content a gradual change in hysteresis loops is observed. Specifically, saturation magnetization (M_s) increases, from 2.9 to 7.0 and 10.8 emu/g for PVDF nanocomposites with 5, 10 and 15 wt% Fe_3O_4 content respectively. As compared to the saturation magnetization

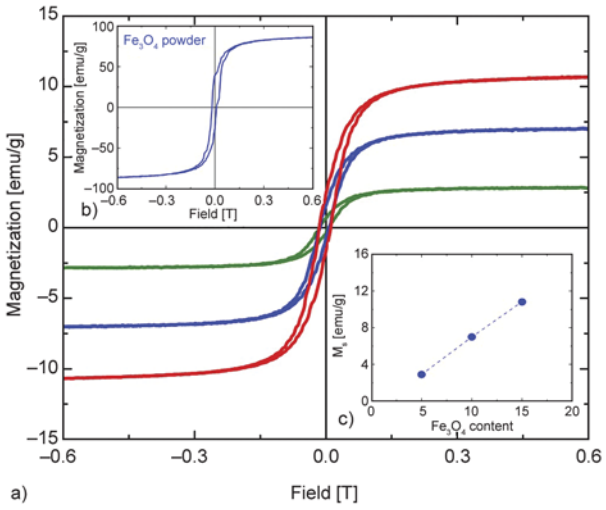

Figure 5. (a) Hysteresis loop recorded at room temperature for samples PVDF/CNT/(Fe_3O_4): 5, 10 and 15 wt% (green, blue and red respectively) in Fe_3O_4 content. Inset: saturation magnetization values with magnetite content, (b) Hysteresis loop recorded at room temperature for pure magnetite powder, (c) saturation magnetization values for magnetite nanocomposites as a function of Fe_3O_4 content.

value of 87.6 emu/g (Figure 5b), for the starting magnetite powder, these values are considerably lower due to their addition into a nonmagnetic polymer matrix as well as the low content (5–15 wt%) of the Fe_3O_4 nanoparticles [39]. The observed linear increase in the values of saturation magnetization (Figure 5c inset) can, however, be attributed to the high dispersion of the magnetic nanoparticles in the polymer matrix and is in accordance with the results obtained by various other authors [14, 15, 29].

3.6. Electrical and dielectric characterization

Figures 6a and 6b show the variation of dielectric permittivity (ε') and dielectric loss (ε'') for PVDF and its nanocomposites, as a function of frequency at room temperature. In the low frequency region (1–10^3 Hz) for all the nanocomposites, there is a significant increase of ε' values, between two and three orders of magnitude as compared to pristine PVDF samples. In fact, for the PVDF/CNT composite itself, a huge increase is observed from ~8 (at 10 Hz) to 2425 (at 10 Hz), largely due to the interaction between the PVDF and CNT. It is interesting to note that the dielectric permitivitty of the composite is higher than the PVDF matrix (about 10) and of carbon nanotubes alone (about 2000), thereby hinting at the synergistic interactions between them. Accord-

ing to the Maxwell-Wagner-Sillars (MWS) effect, when a current flows across the two-materials interfaces, charges can be accumulated at the interface between two dielectric materials with different relaxation times ($\tau = \varepsilon/\sigma$, where ε is the dielectric permittivity and σ is the conductivity). As the relaxation time of PVDF is significantly higher than that of CNT, the charge carriers are blocked at the internal interfaces due to the MWS effect, thereby enhancing the dielectric permittivity significantly. Moreover, in the study carried out by Yuan *et al.* [40], the formation of donor-acceptor complexes at the PVDF-CNT interfaces was shown to enhance the dielectric permittivity due to MWS effects. Now, as the Fe_3O_4 content increases in PVDF/CNT matrix, ε' values again gradually increase in the lower frequency region, while for the highest Fe_3O_4 content (15 wt%), ε' reduces below the corresponding values of PVDF/CNT. At 100 Hz, the PVDF/CNT/$(Fe_3O_4)_{15\%}$ sample presents the lowest ε' value (1120) between all the PVDF/CNT/Fe_3O_4 nanocomposites, while the maximum ε' value (12140) is exhibited by the PVDF/CNT/$(Fe_3O_4)_{10\%}$ sample. While the dielectric permittivity of Fe_3O_4 has a value below 100 at room temperature [41], it is obvious that the Fe_3O_4 nanoparticles play an important role on the dielectric properties of composites, with the increase in the ε' values (for 5 and 10 wt% Fe_3O_4 samples) caused by increasing the interfacial space-charge polarization between the polymer matrix and the Fe_3O_4 filler. Also, PVDF/CNT/$(Fe_3O_4)_{10\%}$ presents the highest stability in ε' values for frequencies below 100 kHz, an interesting property which could further be utilized for electronic devices.

Now, in the present system the content of CNT is higher than percolation threshold [18, 19], while the content of Fe_3O_4 is lower than the percolation threshold in PVDF/Fe_3O_4 systems [12]. As mentioned above, by increasing the Fe_3O_4 content in PVDF/Fe_3O_4 systems, ε' values gradually increase in low frequency region [12]. In the earlier work [12], it was observed that for Fe_3O_4 content of up to 6% volume fraction (similar concentration to our PVDF/CNT/$(Fe_3O_4)_{15\%}$), ε' reaches a value between 40–50 at 100 Hz. In our case, the dramatic increase of the dielectric permittivity to 7490 at 5 wt% Fe_3O_4 content suggests that a synergistic effect occurs between the PVDF-CNT matrix and the Fe_3O_4 nanoparticles. As discussed earlier, the high dielectric permit-

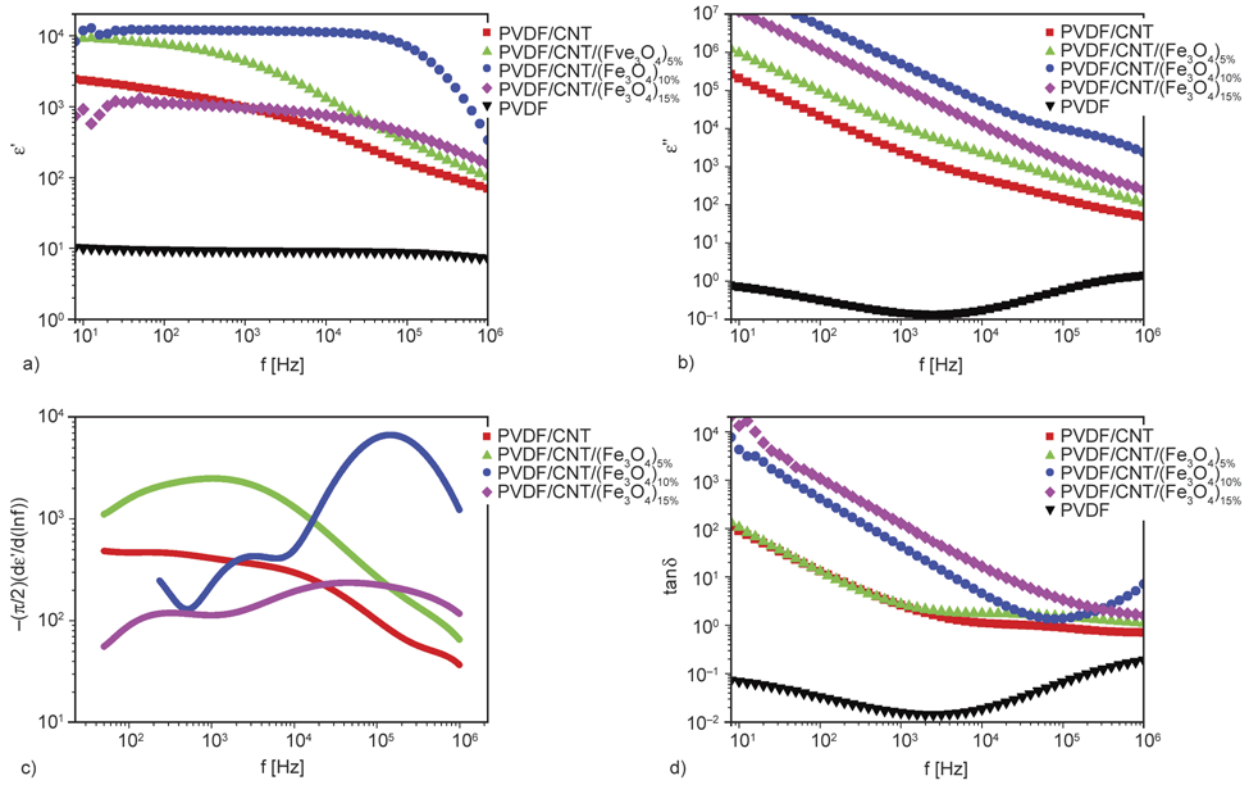

Figure 6. (a) Real part of dielectric permittivity, (b) imaginary part of dielectric permittivity, (c) imaginary part of dielectric permittivity after subtraction of DC conductivity according to the Equation (3) and (d) dissipation factor tanδ as a function of frequency for PVDF system at room temperature

tivity values at CNT content above the percolation threshold is related to the presence of a large number of nanocapacitor structures together with a large dipole moment of interfacial polarization wherein the conductive CNT act as nanoelectrodes and the PVDF matrix as nanodielectrics, experiencing interfacial polarization [42, 43]. The charges which are trapped at the nanofiller-polymer interface result in the MWS polarization effect. This leads to enormous increase in the dielectric permittivity and its strong frequency dependence at the low frequency regime.

The distribution of CNT within the insulating polymer matrix, except the formation of donor-acceptor complexes at the PVDF-CNT interface [40], forms lots of nanocapacitors connected not only in series but also in parallel combinations, while this nanocapacitor's formation can significantly improve the dielectric permittivity of the nanocomposites [44, 45]. Of course, the presence of the magnetite inclusions is expected to affect this nanocapacitors formation. As shown in Figure 6a, at the highest Fe_3O_4 content (15 wt%) the value of ε' (1121) is lower than that of PVDF/CNT (1636) at 100 kHz. This fact indicates a significant differentiation in the formation of nanocapacitors at higher Fe_3O_4 content. More specifically, at high Fe_3O_4 content it is possible that the Fe_3O_4 nanoparticles increase the insulatinge gaps between CNT which led to a reduction in the dielectric permittivity of nanocapacitors. The capacitance has an inverse relationship with the thickness of dielectric materials and therefore an increase in nanodielectric thickness leads to a reduction in capacitance despite the polar nature of Fe_3O_4.

In the PVDF-based nanocomposites, overall three relaxations are observed in the dielectric relaxation frequency spectra. From the low – frequencies to the high – frequencies, these relaxations were identified as MWS interfacial polarization, α_c relaxation and α_α relaxation, respectively. Here, two dielectric relaxations are evident in pristine PVDF at room temperature in the frequency spectra as shown in Figure 6b. The first peak at frequency higher than 1 MHz is the α_α relaxation, also referred to as the primary relaxation. The frequency limit of the instrument constrained the full view of this relaxation. However, earlier works have confirmed the peak around 1 MHz is related to the micro-Brownian cooperative motions of the main chain backbone and is essentially the dielectric manifestation of the glass transition temperature of the PVDF [46–48]. The second relaxation peak observed at lower than 10 Hz is the α_c relaxation and is attributed to molecular motions (rotation and twisting with a small lengthwise translation of the crystalline chain) of the PVDF crystalline region [47]. All the previous relaxations should be affected by the presence of the conductive CNT and semi-conductive Fe_3O_4 fillers. It was found that crystalline relaxation is not affected by the addition of the Fe_3O_4 filler in PVDF/Fe_3O_4 systems, while Fe_3O_4 loading has shown retardation in the glass transition dynamics [48].

As seen in Figure 6b, the presence of CNT makes almost the overall frequency spectra to be dominated by the effects related to the DC conductivity, which result in high values of ε''. The dielectric losses follow an ω^{-1} dependence according to $\varepsilon'' = \sigma_{dc}/(\varepsilon_0 \cdot \omega)$, where ε_0 is permittivity of vacuum and $\omega = 2\pi f$ the angular frequency. In the linear segment of logε'' *vs*. log$f$ representation of Figure 6b the sample PVDF/CNT/$(Fe_3O_4)_{10\%}$ presents higher losses, while the one of PVDF/CNT the lower. Deviation from the linear dependence ω^{-1} of the losses ε'' is present at higher frequencies in all nanocomposites. Especially, one shoulder is evidence above 100 kHz for the PVDF/CNT/$(Fe_3O_4)_{10\%}$, and its high values of ε'' suggest that it should be related to the motion of charges. The dominant contribution of Ohmic conduction makes difficult to extract information about the characteristics of dielectric relaxations which take place in nanocomposites as a result of nanofillers. One convenient technique to eliminate the contribution of Ohmic conduction is based on the following derivation (Equation (3)) [49]:

$$\varepsilon''_{\text{deriv}} = -\frac{\pi}{2} \cdot \frac{\partial \varepsilon'(f)}{\partial \ln f} \approx \varepsilon'' \tag{3}$$

which yields approximately the dielectric loss for the case of broad peaks. As a result, one can obtain conductivity-free dielectric loss peaks as depicted in the Figure 6c. The losses in PVDF/CNT occupy the whole frequency window with a tendency for saturation at lowest frequencies and a peak could be read at 170 Hz. The sample with the lowest Fe_3O_4 content also shows a broad peak with maximum value of dielectric loss, ε''_{max}, at frequency 1 kHz. The samples with the highest Fe_3O_4 concentrations (10 and 15 wt%) show two distinct peaks where the one at high frequency is more dominant. The high frequency peaks are located at frequencies 145 kHz

and 46 kHz for the specimens PVDF/CNT/$(Fe_3O_4)_{10\%}$ and PVDF/CNT/$(Fe_3O_4)_{15\%}$ respectively. For the same specimens the low frequency peaks occur at frequencies 3.3 and 330 kHz, respectively.

The high values of dielectric losses, ε''_{max}, of the Figure 6c peaks clearly suggest that the these relaxations, should be related to short range electric charges motion. Also, the values of the dielectric permittivity of the components (PVDF, CNT and Fe_3O_4), cannot explain the high permittivity values of nanocomposites in terms of simple mixing if one does not take place interfacial polarization effects. Thus, the loss peak which was detected at 170 Hz in PVDF/CNT (Figure 6c), should be related to the MWS interfacial polarization due to the formation of donor-acceptor complexes at the PVDF-CNT interface in conjunction with the nanocapacitor structure of CNT and PVDF matrix. At the lower Fe_3O_4 content (5 wt%), the presence of a broad loss peak at 1 kHz in Figure 6c, suggests that the formation of donor-acceptor complexes at the PVDF-CNT interface in conjunction with the nanocapacitor structure of CNT and PVDF matrix, has also the dominant role in the appearance of MWS interfacial polarization mechanism.

On the other hand, at higher Fe_3O_4 content (10 and 15 wt%) the low frequency loss peaks present a remarkable reduction of dielectric losses (ε''_{max}) values, which indicate that the presence of Fe_3O_4 inclusions restrict the contribution of nanocapacitor structure of CNT-PVDF matrix to the formation of interfacial polarization effects. This behaviour is consistent with the insulating effect of Fe_3O_4 inclusions discussed previously, commenting on the results of Figure 6a. The presence of semi-conductive Fe_3O_4, is expected to enhance the complexity as well as the number of interfaces between the components of our ternary system. The appearance of a second loss peak, more enhanced, at higher frequencies in PVDF/CNT/$(Fe_3O_4)_{10\%}$ and PVDF/CNT/$(Fe_3O_4)_{15\%}$ nanocomposites, should be connected to the Fe_3O_4 inclusions effects. These higher frequency relaxations, play a major role in forming the dielectric constant in PVDF/CNT/$(Fe_3O_4)_{10\%}$ and PVDF/CNT/$(Fe_3O_4)_{15\%}$ nanocomposites. In a study of Fe_3O_4–polypyrrole hybrid nanocomposites carried out by Dey *et al*. [41], the interface between polypyrrole and Fe_3O_4, was found to play an important role in producing a large dielectric constant. A MWS type interfacial polarization mechanism appears at high frequency range, caused from Fe_3O_4-polypyrrole interfaces and leads to a high dielectric constant in the nanocomposite. So, it is possible the second loss peak at higher frequencies in PVDF/CNT/$(Fe_3O_4)_{10\%}$ and PVDF/CNT/$(Fe_3O_4)_{15\%}$ nanocomposites, to be related with a MWS type interfacial polarization caused by a synergetic effect that occurs between the PVDF-CNT matrix and Fe_3O_4 inclusions interfaces.

The real and imaginary parts, ε' and ε'', of the complex dielectric function $\varepsilon^* = \varepsilon' - j\varepsilon''$, define the dissipation factor $\tan\delta = \varepsilon''/\varepsilon'$ which is of great importance in technological applications since it reflects the ratio of dissipated energy per stored energy. Figure 6d shows the dissipation factors of PVDF and its nanocomposites. It can be observed that the dissipation factor of nanocomposites present enhanced values in relation to the pure PVDF and as the frequency decreases, $\tan\delta$ almost linearly increases several orders of magnitude. While in the pure PVDF $\tan\delta$ takes values lower than 0.1 at all frequency spectra, the nanocomposites exhibit values higher than 1 almost at all frequency range. The nanocomposite PVDF/CNT/$(Fe_3O_4)_{15\%}$ with the higher dissipation factor, at lower frequency range, takes value of 127 at 1 kHz. Both PVDF/CNT/$(Fe_3O_4)_{5\%}$ and PVDF/CNT exhibit almost the same frequency dependence of dissipation factor at lower frequency region and also present the lower value of 2.7 at 1 kHz.

As one can observe in Figure 6d, one shoulder appears above 10 kHz in both PVDF/CNT and PVDF/CNT/$(Fe_3O_4)_{5\%}$. For the same relaxation process the peak in $\tan\delta$ is shifted at higher frequencies relatively to the one of imaginary part of dielectric permittivity. The relaxation ratio, $\Delta\varepsilon/\varepsilon_\infty + 1$, as well as the distribution parameters of the process will determine how close or far apart the peaks will be [50]. Therefore, the shoulders in $\tan\delta$ should be related to the relaxation process detected at low frequencies in both nanocomposites (Figure 6c).

The alternating current (AC) conductivity is a proper representation to correlate the macroscopic measurement to the microscopic movement of the charge carriers. Figure 7a shows the AC electrical conductivity of the studied system, which is determined by using the dielectric data as $\sigma' = \varepsilon_0\varepsilon''\omega$. All nanocomposites exhibit a plateau at lower frequencies which corresponds to DC conductivity, σ_{dc}. DC conductivity measurements which carried out with Keithley 2440 Sourcemeter confirm the previous allegation

with high accuracy. The lower value of DC conductivity between the nanocomposites is exhibited by PVDF/CNT. At 10 Hz, PVDF/CNT presents a value higher more than 5 orders of magnitude relatively to that of pure PVDF. This is an expected behavior since CNT content is well above the value of percolation threshold. By increasing the Fe_3O_4 content, DC conductivity increases up to PVDF/CNT/$(Fe_3O_4)_{10\%}$ which presents the maximum value of $2.8 \cdot 10^{-4}$ S/cm, more than two orders of magnitude higher than this of PVDF/CNT. At the higher Fe_3O_4 content, the DC conductivity reduces at a value of $6.7 \cdot 10^{-5}$ S/cm which is significantly higher than these of the rest two nanocomposites PVDF/CNT and PVDF/CNT/$(Fe_3O_4)_{5\%}$. The reduced value of DC conductivity at high Fe_3O_4 content should be related to the barrier effect of the Fe_3O_4 nanoparticles that disrupted the conductive network of CNT and made it more difficult for charge carriers to move throughout the network [51].

Electric modulus formalism has been proved very efficient in analyzing dielectric data of polymer matrix nanocomposites. The electric modulus is defined by Equation (4) as the inverse quantity of complex dielectric permittivity [52]:

$$M^* = M' + jM'' = \frac{1}{\varepsilon^*} = \frac{\varepsilon'}{\varepsilon'^2 + \varepsilon'^2} + j\frac{\varepsilon''}{\varepsilon'^2 + \varepsilon''^2} \quad (4)$$

where ε', M' are the real and ε'', M'' the imaginary parts of dielectric permittivity and electric modulus, respectively. Figure 7b shows the dependence of M'' as a function of frequency f, at room temperature. In pure PVDF, the peak which appears below 10 Hz is assigned as the α_c relaxation, while the one appearing at frequency higher than 1 MHz is the α_α relaxation. In nanocomposites the contribution of a high frequency relaxation is dominant, while a shoulder exists at lower frequency range which is more distinct in PVDF/CNT/$(Fe_3O_4)_{10\%}$. Figure 7c shows the best fitting of the following relation which consists of a sum of a Havriliak–Negami expression (Equation (5)) and a linear term:

$$M'' = \mathrm{Im}\left\{\frac{\Delta M'}{(1 + (j\omega\tau_{\mathrm{HN}})^{\alpha})^{\beta}}\right\} + A\omega^{\mathrm{n}} \quad (5)$$

to the experimental data of PVDF/CNT/$(Fe_3O_4)_{10\%}$ in order to separate these two contributions. The first term of Equation (4) represents the contribution of the lower frequencies relaxation, where $\Delta M' = M'_\infty - M'_s$, $M'_\infty = 1/\varepsilon'_\infty$, $M'_s = 1/\varepsilon'_s$. τ_{HN} is a characteristic relaxation time. α and β are the Havriliak-Negami shape parameters which correspond to the widening and asymmetry of relaxation times distribution and $\omega = 2\pi f$ the angular frequency of the applied electric field. The second term of Equation (4) represents the linear contribution of the higher frequency relaxation to the log–log frequency spectrum. The

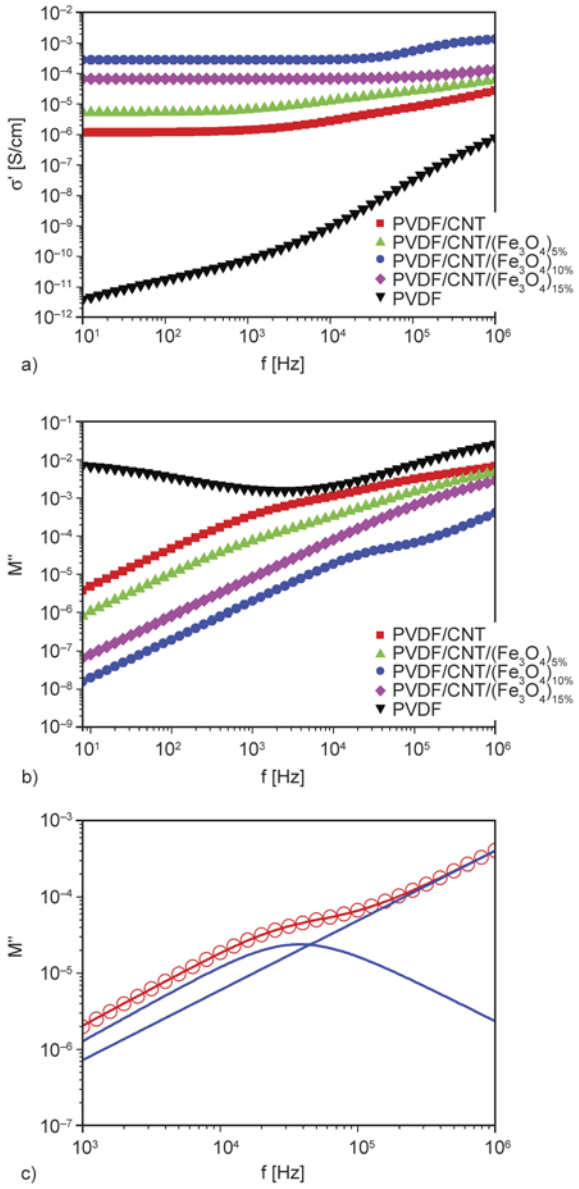

Figure 7. (a) AC electrical conductivity as a function of frequency for PVDF system at room temperature, (b) dependence of imaginary part of electric modulus as a function of frequency, for PVDF system at room temperature, (c) experimental data (red circles), total (red line) and individual (blue lines) fitting curves of the imaginary part M'' of electric modulus according to Equation (4) for the sample with 10 wt% Fe_3O_4 with parameters values: $\alpha = 1$, $\beta = 0.91$, $1/(2\pi\tau_{\mathrm{HN}}) = 35.3$ kHz, $\Delta M' = 5 \cdot 10^{-5}$, $A = 1.32 \cdot 10^{-9}$ and $n = 0.91$.

parameter A reflects the position and the strength of this mechanism while *n* defines the slope of the linear left–side contribution.

DC conductivity is given through the relation $\sigma_{dc} = \varepsilon_0\varepsilon_s\omega_0$, where ε_0 is the permittivity of vacuum, ε_s the dielectric constant and as ω_0 is taken the angular frequency which corresponds to maximum peak position of conductivity relaxation mechanism in the imaginary part of electric modules function, $\omega_0 = 2\pi f_{max,M''}$ [53]. As shown in Figure 7c the relaxation presents a maximum value of M'' at frequency $f_{max,M''} = 36.6$ kHz.

If we choose the value of $\varepsilon' = 12\,140$ at 100 Hz as the value of dielectric constant of PVDF/CNT/$(Fe_3O_4)_{10\%}$, then according to the previous relation the DC conductivity is found to be $2.5\cdot10^{-4}$ S/cm. This value is very close to the corresponding one extracted from the plateau of Figure 7a, which is $2.8\cdot10^{-4}$ S/cm. This fact is a strong indication that the relaxation which appears as shoulder in logM''–log$f$ plots of Figure 7b is the conductivity mechanism and $f_{max,M''}$ value separates the regions of short-range and long-range mobility of charges at the right-hand and left-hand sides of M'' maximum, respectively [54].

As it is obvious in Figure 7c, the shoulder of PVDF/CNT/$(Fe_3O_4)_{10\%}$ exists at the higher frequency, while the shoulder of PVDF/CNT is present at lower frequency. The characteristic frequency ω_0 is closely related to the relaxation time of conductivity mechanism via the relation $\tau_0 = 1/\omega_0$. So, higher ω_0 means faster conductivity relaxation. According to the relation $\sigma_{dc} = \varepsilon_0\varepsilon_s\omega_0$, the DC conductivity is proportional to both, dielectric permittivity and characteristic frequency ω_0. PVDF/CNT/$(Fe_3O_4)_{10\%}$ characterized from the higher values of dielectric permittivity and ω_0, so it is expected to have the higher σ_{dc} value. On the other hand, PVDF/CNT/$(Fe_3O_4)_{15\%}$ although presents the lower ε' value, the significantly high value of ω_0 dominates and so its σ_{dc} value is higher than that of PVDF/CNT and PVDF/CNT/$(Fe_3O_4)_{5\%}$.

The present study, which is related to the morphological, thermal, magnetic, dielectric and electrical characterization of the novel PVDF/CNT/Fe_3O_4 ternary system, was carried out at room temperature. Investigation of the dielectric properties as well as electrical properties at different temperature profiles using the same nanocomposites will be performed in an ensuing study.

4. Conclusions

Nanocomposites consisting of PVDF as matrix, acting as ferroelectric and piezoelectric phase, Fe_3O_4 nanopowders as magnetic (ferrite) phase and CNT as conductive phase were prepared by the twin screw compounding method. SEM measurements show a good dispersion of nanoinclusions in the PVDF matrix, and only at the used highest Fe_3O_4 particle concentration agglomerates containing three or more particles were observed. FTIR and XRD measurements provide clear evidence that mainly the presence of CNT induces the formation of β phase in nanocomposites. According to DSC measurements, the degree of crystallinity is practically unaffected by the addition of CNT for the lowest concentration of Fe_3O_4 particles. For higher Fe_3O_4, content a decrease of the degree of crystallinity is observed. From magnetic measurements, apart from the ferrimagnetic behavior of the prepared nanocomposites, the gradually increase of saturation magnetization values with the magnetite content is confirmed.

The overall frequency spectrum is dominated by the effects related to DC conductivity. The removing of the effect of ohmic conductivity, revealed dielectric loss peaks. In PVDF/CNT and PVDF/CNT/$(Fe_3O_4)_{5\%}$ one broad loss peak appears at the low frequencies region. At higher Fe_3O_4 content, the influence of Fe_3O_4 nanoparticles in PVDF-CNT matrix gives rise to the existence of a second loss peak, more enhanced at higher frequencies. The high values of both, dielectric losses, ε''_{max}, and dielectric permittivity, ε', suggest that these loss peaks are possible related to the MWS interfacial polarization mechanisms. The first one, at lower frequencies, should be related to the formation of donor-acceptor complexes at the PVDF-CNT interface in conjunction with the nanocapacitor structure of CNT and PVDF matrix. The second one, at higher frequencies, it is possible to be caused by a synergetic effect that occurs between the PVDF-CNT matrix and Fe_3O_4 inclusions interfaces.

However, it should be noted that further investigation is needed to clarify the origin of these two peaks.

Values of dielectric permittivity were significantly enhanced in the whole frequency range due to the presence of both CNT and Fe_3O_4. Composites with 10 wt% Fe_3O_4, present higher stability in dielectric permittivity values in almost the whole frequency

spectrum, a behavior interesting for electronics devices applications. The incorporation of Fe_3O_4 in PVDF/CNT matrix gradually increases the values of both, dielectric permittivity and DC conductivity, when the content of Fe_3O_4 is up to 10 wt%. At the higher magnetite content, the role of Fe_3O_4 as insulating barrier in the PVDF/CNT matrix should be dominant. On the one hand, Fe_3O_4 nanoparticles it is possible to increase the insulating gaps between CNT which led to a reduction in the dielectric permittivity of nanocapacitors, as well as to the total dielectric permittivity. On the other hand, the possible barrier effect of Fe_3O_4 nanoparticles restricts the conductive network of CNT and as a result reduces the DC conductivity. PVDF/CNT/Fe_3O_4 ternary composites constitute a very promising system with large potential in diverse fields since combines and matches together piezoelectric, electrical, dielectric and magnetic properties.

Acknowledgements

This research has been co-financed by the European Union (European Social Fund – ESF) and Greek national funds through the Operational Program 'Education and Lifelong Learning' of the National Strategic Reference Framework (NSRF) □ Research Funding Program: THALES. Investing in knowledge society through the European Social Fund. (MIS 379346).

The authors also would like to thank Associate Professor M. Angelakeris for providing access to VSM instrument.

References

[1] Sencadas V., Moreira V. M., Lanceros-Mendez S., Pouzada A. S., Filho R. G.: α- to β transformation on PVDF films obtained by uniaxial stretch. Materials Science Forum, **514–516**, 872–876 (2006). DOI: 10.4028/www.scientific.net/MSF.514-516.872

[2] Nalwa H. S.: Ferroelectric polymers: Chemistry, physics, and applications. Marcel Dekker, New York (1995).

[3] Kepler R. G., Anderson R. A.: Piezoelectricity and pyroelectricity in polyvinylidene fluoride. Journal of Applied Physics, **49**, 4490–4494 (1978). DOI: 10.1063/1.325454

[4] Lovinger A. J.: Annealing of poly(vinylidene fluoride) and formation of a fifth phase. Macromolecules, **15**, 40–44 (1982). DOI: 10.1021/ma00229a008

[5] Chiang C. K., Popielarz R.: Polymer composites with high dielectric constant. Ferroelectrics, **275**, 1–9 (2002). DOI: 10.1080/00150190214285

[6] Ishida H., Campbell S., Blackwell J.: General approach to nanocomposite preparation. Chemistry of Materials, **12**, 1260–1267 (2000). DOI: 10.1021/cm990479y

[7] Ezquerra T. A., Canalda J. C., Sanz A., Linares A.: On the electrical conductivity of PVDF composites with different carbon-based nanoadditives. Colloid and Polymer Science, **292**, 1989–1998 (2014). DOI: 10.1007/s00396-014-3252-6

[8] Prinz G. A.: Magnetoelectronics. Science, **282**, 1660–1663 (1998). DOI: 10.1126/science.282.5394.1660

[9] Kumar J., Singh R. K., Samanta S. B., Rastogi R. C., Singh R.: Single-step magnetic patterning of iron nanoparticles in a semiconducting polymer matrix. Macromolecular Chemistry and Physics, **207**, 1584–1588 (2006). DOI: 10.1002/macp.200600260

[10] Eerenstein W., Mathur N. D., Scott J. F.: Multiferroic and magnetoelectric materials. Nature, **442**, 759–765 (2006). DOI: 10.1038/nature05023

[11] Yang T-I., Brown R. N. C., Kempel L. C., Kofinas P.: Magneto-dielectric properties of polymer–Fe_3O_4 nanocomposites. Journal of Magnetism and Magnetic Materials, **320**, 2714–2720 (2008). DOI: 10.1016/j.jmmm.2008.06.008

[12] Wang X., Li W., Luo L., Fang Z., Zhang J., Zhu Y.: High dielectric constant and superparamagnetic polymer-based nanocomposites induced by percolation effect. Journal of Applied Polymer Science, **125**, 2711–2715 (2012). DOI: 10.1002/app.36587

[13] Prabhakaran T., Hemalatha J.: Ferroelectric and magnetic studies on unpoled poly (vinylidine fluoride)/Fe_3O_4 magnetoelectric nanocomposite structures. Materials Chemistry and Physics, **137**, 781–787 (2013). DOI: 10.1016/j.matchemphys.2012.09.064

[14] Bhatt A. S., Krishna Bhat D., Santosh M. S.: Crystallinity, conductivity, and magnetic properties of PVDF-Fe_3O_4 composite films. Journal of Applied Polymer Science, **119**, 968–972 (2011). DOI: 10.1002/app.32796

[15] Xu C., Ouyang C., Jia R., Li Y., Wang X..: Magnetic and optical properties of poly(vinylidene difluoride)/Fe_3O_4 nanocomposite prepared by coprecipitation approach. Journal of Applied Polymer Science, **111**, 1763–1768 (2009). DOI: 10.1002/app.29194

[16] Zhang W-B., Zhang Z-X., Yang J-H., Huang T., Zhang N., Zheng X-T., Wang Y., Zhou Z-W.: Largely enhanced thermal conductivity of poly(vinylidene fluoride)/carbon nanotube composites achieved by adding graphene oxide. Carbon, **90**, 242–254 (2015). DOI: 10.1016/j.carbon.2015.04.040

[17] Liu Z. D., Feng Y., Li W. L.: High dielectric constant and low loss of polymeric dielectric composites filled by carbon nanotubes adhering $BaTiO_3$ hybrid particles. RSC Advances, **5**, 29017–29021 (2015).
DOI: 10.1039/C5RA00639B

[18] Bauhofer W., Kovacs J. Z.: A review and analysis of electrical percolation in carbon nanotube polymer composites. Composites Science and Technology, **69**, 1486–1498 (2009).
DOI: 10.1016/j.compscitech.2008.06.018

[19] Li Q., Xue Q. Z., Gao X. L., Zheng Q. B.: Temperature dependence of the electrical properties of the carbon nanotube/polymer composites. Express Polymer Letters, **3**, 769–777 (2009).
DOI: 10.3144/expresspolymlett.2009.95

[20] Mandal B. P., Vasundhara K., Abdelhamid E., Lawes G., Salunke H. G., Tyagi A. K.: Improvement of magnetodielectric coupling by surface functionalization of nickel nanoparticles in ni and polyvinylidene fluoride nanohybrids. The Journal of Physical Chemistry C, **118**, 20819–20825 (2014).
DOI: 10.1021/jp5065787

[21] Lanceros-Mendez S., Mano J. F., Costa A. M., Schmidt V. H.: FTIR and DSC studies of mechanically deformed β-PVDF films. Journal of Macromolecular Science Part B: Physics, **40**, 517–527 (2001).
DOI: 10.1081/MB-100106174

[22] Vasundhara K., Mandal B. P., Tyagi A. K.: Enhancement of dielectric permittivity and ferroelectricity of a modified cobalt nanoparticle and polyvinylidene fluoride based composite. RSC Advances, **5**, 8591–8597 (2015).
DOI: 10.1039/C4RA09292A

[23] Salimi A., Yousefi A. A.: Analysis method: FTIR studies of β-phase crystal formation in stretched PVDF films. Polymer Testing, **22**, 699– 704 (2003).
DOI: 10.1016/S0142-9418(03)00003-5

[24] Gregorio Jr. R., Cestari M.: Effect of crystallization temperature on the crystalline phase content and morphology of poly(vinylidene fluoride). Journal of Polymer Science Part B: Polymer Physics, **32**, 859–870 (1994).
DOI: 10.1002/polb.1994.090320509

[25] Matsushige K., Nagata K., Imada S., Takemura T.: The II-I crystal transformation of poly(vinylidene fluoride) under tensile and compressional stresses. Polymer, **21**, 1391–1397 (1980).
DOI: 10.1016/0032-3861(80)90138-X

[26] Ke K., Pötschke P., Jehnichen D., Fischer D., Voit B.: Achieving β-phase poly(vinylidene fluoride) from melt cooling: Effect of surface functionalized carbon nanotubes. Polymer, **55**, 611–619 (2014).
DOI: 10.1016/j.polymer.2013.12.014

[27] Georgousis G., Pandis C., Kalamiotis A., Georgiopoulos P., Kyritsis A., Kontou E., Pissis P., Micusik M., Czanikova K., Kulicek J., Omastova M.: Strain sensing in polymer/carbon nanotube composites by electrical resistance measurement. Composites Part B: Engineering, **68**, 162–169 (2015).
DOI: 10.1016/j.compositesb.2014.08.027

[28] Martins P., Costa C., Lanceros-Mendez S.: Nucleation of electroactive β-phase poly(vinilidene fluoride) with $CoFe_2O_4$ and $NiFe_2O_4$ nanofillers: A new method for the preparation of multiferroic nanocomposites. Applied Physics A, **103**, 233–237 (2011).
DOI: 10.1007/s00339-010-6003-7

[29] Martins P., Costa C. M., Botelho G., Lanceros-Mendez S., Barandiaran J. M., Gutierrez J.: Dielectric and magnetic properties of ferrite/poly(vinylidene fluoride) nanocomposites. Materials Chemistry and Physics, **131**, 698–705 (2012).
DOI: 10.1016/j.matchemphys.2011.10.037

[30] Martins P., Lopes A. C., Lanceros-Mendez S.: Electroactive phases of poly(vinylidene fluoride): Determination, processing and applications. Progress in Polymer Science, **39**, 683–706 (2014).
DOI: 10.1016/j.progpolymsci.2013.07.006

[31] Levi N., Czerw R., Xing S., Iyer P., Carroll D. L.: Properties of polyvinylidene difluoride–carbon nanotube blends. Nano Letters, **4**, 1267–1271 (2004).
DOI: 10.1021/nl0494203

[32] Huang X., Jiang P., Kim C., Liu F., Yin Y.: Influence of aspect ratio of carbon nanotubes on crystalline phases and dielectric properties of poly(vinylidene fluoride). European Polymer Journal, **45**, 377–386 (2009).
DOI: 10.1016/j.eurpolymj.2008.11.018

[33] Campbell D., White J. R.: Polymer characterization: Physical techniques. Chapman and Hall, London (1989).

[34] Assouline E., Lustiger A., Barber A. H., Cooper C. A., Klein E., Wachtel E., Wagner H. D.: Nucleation ability of multiwall carbon nanotubes in polypropylene composites. Journal of Polymer Science, Part B: Polymer Physics, **41**, 520–527 (2003).
DOI: 10.1002/polb.10394

[35] Mičušík M., Omastová M., Pionteck J., Pandis C., Logakis E., Pissis P.: Influence of surface treatment of multiwall carbon nanotubes on the properties of polypropylene/carbon nanotubes nanocomposites. Polymers for Advanced Technologies, **22**, 38–47 (2011).
DOI: 10.1002/pat.1745

[36] Bhattacharyya A. R., Sreekumar T. V., Liu T., Kumar S., Ericson L. M., Hauge R. H., Smalley R. E.: Crystallization and orientation studies in polypropylene/single wall carbon nanotube composite. Polymer, **44**, 2373–2377 (2003).
DOI: 10.1016/S0032-3861(03)00073-9

[37] Nakagawa K., Ishida Y.: Annealing effects in poly (vinylidene fluoride) as revealed by specific volume measurements, differential scanning calorimetry, and electron microscopy. Journal of Polymer Science: Polymer Physics Edition, **11**, 2153–2171 (1973). DOI: 10.1002/pol.1973.180111107

[38] Gregorio Jr R.: Determination of the α, β, and γ crystalline phases of poly(vinylidene fluoride) films prepared at different conditions. Journal of Applied Polymer Science, **100**, 3272–3279 (2006). DOI: 10.1002/app.23137

[39] Cullity B. D., Graham C. D.: Introduction to magnetic materials. Wiley, New Jersey (2009).

[40] Yuan J-K., Yao S-H., Dang Z-M., Sylvestre A., Genestoux M., Bai J.: Giant dielectric permittivity nanocomposites: Realizing true potential of pristine carbon nanotubes in polyvinylidene fluoride matrix through an enhanced interfacial interaction. Journal of Physical Chemistry C, **115**, 5515–5521 (2011). DOI: 10.1021/jp1117163

[41] Dey A., De A., De S. K.: Electrical transport and dielectric relaxation in Fe_3O_4–polypyrrole hybrid nanocomposites. Journal of Physics: Condensed Matter, **17**, 5895–5910 (2005). DOI: 10.1088/0953-8984/17/37/025

[42] Wang L., Dang Z-M.: Carbon nanotube composites with high dielectric constant at low percolation threshold. Applied Physics Letters, **87**, 042903/1–042903/3 (2005). DOI: 10.1063/1.1996842

[43] Arjmand M., Apperley T., Okoniewski M., Sundararaj U.: Comparative study of electromagnetic interference shielding properties of injection molded versus compression molded multi-walled carbon nanotube/polystyrene composites. Carbon, **50**, 5126–5134 (2012). DOI: 10.1016/j.carbon.2012.06.053

[44] Simoes R., Silva J., Vaia R., Sencadas V., Costa P., Gomes J., Lanceros-Méndez S.: Low percolation transitions in carbon nanotube networks dispersed in a polymer matrix: Dielectric properties, simulations and experiments. Nanotechnology, **20**, 035703/1–035703/8 (2009). DOI: 10.1088/0957-4484/20/3/035703

[45] Yao S-H., Dang Z-M., Xu H-P., Jiang M-J., Bai J.: Exploration of dielectric constant dependence on evolution of microstructure in nanotube/ferroelectric polymer nanocomposites. Applied Physics Letters, **92**, 082902/1–082902/3 (2008). DOI: 10.1063/1.2870104

[46] Bello A., Laredo E., Grimau M.: Distribution of relaxation times from dielectric spectroscopy using Monte Carlo simulated annealing: Application to α–PVDF. Physical Review: B, **60**, 12764–12774 (1999). DOI: 10.1103/PhysRevB.60.12764

[47] Kochervinskii V. V., Malyshkina I. A., Markin G. V., Gavrilova N. D., Bessonova N. P.: Dielectric relaxation in vinylidene fluoride–hexafluoropropylene copolymers. Journal of Applied Polymer Science, **105**, 1107–1117 (2007). DOI: 10.1002/app.26145

[48] Chanmal C., Jog J.: Dielectric relaxation spectroscopy for polymer nanocomposites. in 'Characterization techniques for polymer nanocomposites' (ed.: Mittal V.) Wiley, New York, 167–184 (2012). DOI: 10.1002/9783527654505.ch7

[49] Wübbenhorst M., Turnhout J.: Conduction – free dielectric loss $\delta\varepsilon/\delta \ln f$ – A powerful tool for the analysis of strong (ion) conducting dielectric materials. Dielectrics Newsletter: Scientific Newsletters for Dielectric and Impedance Spectroscopy, **14**, 1–3 (2000).

[50] Cao W., Gerhardt R.: Calculation of various relaxation times and conductivity for a single dielectric relaxation process. Solid State Ionics, **42**, 213–221 (1990). DOI: 10.1016/0167-2738(90)90010-O

[51] Sadeghi F., Ajji A.: Study of crystal structure of (polyvinylidene fluoride/clay) nanocomposite films: Effect of process conditions and clay type. Polymer Engineering and Science, **49**, 200–207 (2009). DOI: 10.1002/pen.21248

[52] Macedo P. B., Moynihan C. T., Bose R.: The role of ionic diffusion in polarization in vitreous ionic conductors. Physics and Chemistry Glasses, **13**, 171–179 (1972).

[53] Macdonald J. R.: Comments on the electric modulus formalism model and superior alternatives to it for the analysis of the frequency response of ionic conductors. Journal of Physics and Chemistry of Solids, **70**, 546–554 (2009). DOI: 10.1016/j.jpcs.2008.12.012

[54] Nikonorova N. A., Barmatov E. B., Pebalk D. A., Barmatova M. V., Dominguez-Espinosa G., Diaz-Calleja R., Pissis P.: Electrical properties of nanocomposites based on comb-shaped nematic polymer and silver nanoparticles. Journal of Physical Chemistry C, **111**, 8451–8458 (2007). DOI: 10.1021/jp068688a

eXPRESS Polymer Letters Vol.9, No.12 (2015) 1119–1132
Available online at www.expresspolymlett.com
DOI: 10.3144/expresspolymlett.2015.100

A note on the effect of the fiber curvature on the micromechanical behavior of natural fiber reinforced thermoplastic composites

*M. A. Escalante-Solís, A. Valadez-González, P. J. Herrera-Franco**

Unidad de materiales Centro de Investigación Científica de Yucatán Calle 43 # 130, Col. Chuburná de Hidalgo, C.P. 97200 Mérida, Yucatán, México

Received 29 May 2015; accepted in revised form 5 August 2015

Abstract. To better understand the role of the fiber curvature on the tensile properties of short-natural-fiber reinforced composites, a photoelastic model and a finite element analysis were performed in a well characterized henequen fiber-high density polyethylene composite material. It was hypothesized that the angle of orientation of the inclusion and the principal material orientation with respect to the applied load was very important in the reinforcement mechanics. From the photoelastic and finite element analysis it was found that the stress distribution around the fiber inclusion was different on the concave side from that observed on the convex side and an efficient length of stress transfer was estimated to be approximately equal to one third the average fiber length. This approach was used to predict the short-natural-fiber reinforced composite mechanical properties using probabilistic functions modifications of the rule of mixtures models developed by Fukuda-Chow and the Fukuda-Kawata. Recognizing the inherent flexibility that curves the natural fibers during processing, the consideration of a length of one third of the average length $\bar{l}$ should improve the accuracy of the calculations of the mechanical properties using theoretical models.

Keywords: *reinforcement, natural fibers, fiber critical length, micromechanics, interphase shear strength*

1. Introduction

Cellulosic fibers like flax, hemp, kenaf, henequen, sisal, jute, coconut, coir, kapok, banana and many others have been used as reinforcement agents of different thermosetting and thermoplastic resins. Unlike the traditional engineering fibers, e.g. glass and carbon fibers, these lignocellulosic fibers are able to impart the composite high specific stiffness and strength, they have a desirable fiber aspect ratio and a high degree of flexibility, recyclability and biodegradability, they are non-abrasive to the processing equipment, non-irritating to the skin, no other health hazards, they are readily available from natural sources, and more importantly, they have a low cost per unit volume basis [1, 2].

The problem of fiber-polymeric matrix adhesion has been approached modifying either the fiber surface, or the matrix to ensure the stress transfer, necessary for the effectiveness of the composite material. It follows that the efficiency of load transfer from matrix to fiber in a composite is not only strongly related to the optimum mechanical properties of the constituent components but also to the interfacial parameters, including factors such as: the interfacial shear strength, the interfacial toughness, the matrix shrinkage pressure on the fiber, and the interfacial coefficient of friction [3, 4].

Effective analytical micromechanical models have been developed for synthetic short fiber-reinforced polymers [5]. The most utilized and known theories

*Corresponding author, e-mail: pherrera@cicy.mx

for tensile properties are the rule of mixtures (ROM), the Cox model, the Halpin-Tsai model, and the Bowyer-Bader model [6–8]. The ROMs are very simple models using fiber and matrix sum of volume weighted properties to predict composite properties. ROM can be parallel or series. The Hirsch model is a combination of parallel and series ROM. The Halpin-Tsai model considers matrix-to-fiber properties ratio instead of sum of volume-weighted properties. The Cox model suggests that stress in the fiber is proportional to the difference between fiber strain and the strain that the matrix would have if there were no fibers. The Bowyer–Bader model considers the contribution of fibers below and above critical fiber length. More recently, Nairn proposed a generalized shear-lag analysis model to calculate the tensile elastic modulus of the composite. Nairn extended the optimal shear-lag analysis to a generalized case by enabling the shear stresses to be described by shape functions. He also extended the capabilities of the generalized shear-lag analysis to include an imperfect interface by the addition of an interface parameter D_s [9]. Nairn's model considers the interfacial quality explicitly; however, most models use constants to fit the experimental measurements. Some authors that have used analytical modeling for natural fiber-reinforced (or filled) polymers, incorporated a reinforcement efficiency factor. For example, Simonsen used factors that varied between 0.61 and 0.85, depending on the polymer matrix to model the bending modulus of elasticity of wood fiber–filled thermoplastics made with three different matrices: polypropylene, polyethylene, and polystyrene. A loss factor for fiber orientation has also been used to fit the model to experimental values. Orientation factors for tensile strength found varied from 0.1 to 0.36. The loss factor for stress transfer efficiency was used for the composite modulus of elasticity varied from 0.42 to 0.51 for injection molded jute/polypropylene composites as a function of fiber volume fraction using ROM [10, 11]. Fiber/matrix interfacial shear stress was obtained from single fiber pull–out tests and was incorporated into the tensile strength model. A few other authors have incorporated values for the critical length (L_c) and fiber matrix-adhesion strength (τ) for hemp single fiber/polypropylene composites [12] and Herrera-Franco and Valadez-González [13] used the single fiber fragmentation tests together with pull–out tests on henequen/polyethylene single fiber specimens and found that the critical length and the fiber aspect ratio, varied with fiber/matrix adhesion quality and interfacial shear strength.

Fukuda and Kawata [14] developed a theory for the Young's modulus of short-fiber reinforced composites with variable fiber length and orientation. Later on, Fukuda and Chou [15] adopted the basic probabilistic approach of Fukuda and Kawata [14] to develop a theory for the modulus of short-fiber reinforced composites with variable fiber length and orientation. Summarizing it can be said that the role of the fiber reinforcement is considered in these model using an efficiency factor (or loss factor), together with an orientation factor. The first factor is related to the fiber length, either above or below the fiber critical length L_c, and sometimes estimated from the interfacial shear strength. The second factor is equal to one for unidirectionally oriented fibers and less than one for randomly oriented fibers depending on the angle distribution of the fibers.

Little attention has been paid to the fact that natural fibers are flexible and that depending on their initial length before processing and the processing method used, their final shape will be distorted with shapes other that the stiff, straight fibers upon which all the micromechanical models were developed.

The aim of this paper was the study of the role of the fiber curvature on the prediction of the tensile properties of short-natural-fiber reinforced composites for a well-defined fiber-matrix adhesion system. Emphasis on the flexible behavior of the natural fibers, therefore, fiber length and orientation and its effect on its stress transfer capability and the mechanical properties of the constituents will be discussed. The discussion is built around a well characterized and controlled fiber-matrix system, namely, a high density polyethylene (HDPE) matrix reinforced with henequen fibers (*Agave fourcroydes*).

Although the fibers, as a result of the processing method of the composite, may exhibit a curvature with shapes such as C, D, S, etc., the U-shape was proposed in this paper for the simplicity of the analysis and as the basis to analyze the effect of the other shapes mentioned before. In any case, the approach to handle the fiber curvature will be discussed in the section 7.1.

2. Fiber-matrix adhesion and experimental procedures

The optimization of interfacial bond between a fiber and a polymer matrix is an important aspect with respect to the optimal mechanical performance of fiber reinforced composites in general, and durability in particular. Since the fibers and matrices are chemically different, strong adhesion at their interfaces is needed for an effective transfer of stress and bond distribution throughout an interface. A good compatibility between cellulose fibers and non-polar matrices is achieved from polymeric chains that will favor entanglements and inter-diffusion with the matrix [13, 16]. Several approaches have been explored, such as physical treatments by corona or plasma, and chemical grafting with molecules and macromolecules which display a good compatibility with the matrix and introduce surface hydrophobicity. The chemical modification by coupling agents susceptible to react with the fibers and the matrix constitutes a particularly astute way of controlling the quantity and the nature of the groups present at their surface. Moreover, it creates covalent bridges between the fibers and the matrix which ensure the best mechanical properties for the composite [17]. The physical and mechanical properties of the henequen fiber and the HDPE are listed in Table 1 [13].

The fiber surface properties were modified to enhance the physicochemical interactions at the fiber-matrix interphase. They are first treated with a NaOH aqueous solution alkaline treatment which has two effects on the fiber: (1) it increases the surface roughness that results in a better mechanical interlocking; and (2) it increments the amount of cellulose exposed on the fiber surface, thus increasing the number of possible reaction sites.

In this paper, the following materials were used: as a matrix, high density polyethylene (HDPE) and as reinforcement, henequen fibers (*Agave fourcroydes*) with an average diameter of 180 μm approximately.

In order to enhance the fiber-matrix adhesion two surface pre-treatments were used: first, a silane coupling agent was used and second, a matrix pre-impregnation on the fiber. The henequen fibers were treated with a 2% NaOH aqueous solution for 1 hour at 25°C, washed with distilled water and dried at 60°C for 24 h, after they were surface modified.

The henequen fibers were also treated with vinyl-tris(2-ethoxymethoxy) silane coupling agent and dicumyl peroxide. The peroxide and silane coupling agent were deposited on the surface of the fiber from a methanol/water solution (90:10) adjusted to a pH 3.5 with acetic acid at 25°C. The weight concentration was 1% silane and 0.5% peroxide with respect to the fiber. Then the fibers were dried and cured at 60°C during 24 h.

The fiber-surface silanization opens the way to the rational use of silane coupling agents to functionalize the surface of organic materials. In some cases, optimal conditions can be established thus favoring the substrate condensation reaction and limiting the self-condensation of the silanol groups that produce polysiloxanes. This is particularly interesting, since the grafting efficiency (both in terms of product configuration at the surface and quantity of adsorbed molecules) can be modulated, depending on the envisaged extent of the fiber-surface modification [18, 19].

After the surface modifications, the fibers were pre-impregnated with a solution of HDPE-xylene to ensure a better wetting of the fibers with the polymer. Fiber preimpregnation allows a better fiber wetting which in a normal fiber–polymer mixing procedure would not be possible because of the high polymer viscosity, thus, it enhances the mechanical interlocking between fiber and matrix. The nomenclature used for the different fiber surface treatments and the expected adhesion mechanisms are described in Table 2.

The composite laminates were prepared using a fiber volume fraction of 20% w/w ($V_f = 0.1237$) calculated

Table 1. Physical and mechanical properties of the constituents of composite

Material	σ [MPa]	E [MPa]	Poisson ratio, ν	Equivalent diameter [mm]
Henequen	604	13 200	0.33	0.18
HDPE	28	792	0.30	–

Table 2. Nomenclature used for different fiber surface treatments

Type of bonding	Keyword	Description of treatment
Mechanical bonding	FIB	Fiber without any treatment
	FIBNA	Fiber treated with a NaOH aqueous solution
	FIBNAPRE	Fiber treated with a NaOH aqueous solution and then pre-impregnated with dissolved HDPE
Mechanical plus chemical bonding	FIBNASIL	Fiber treated with a NaOH aqueous solution and then with a silane coupling agent

considering the fiber density equal to 1.7 g/cm^3. The value of the shear modulus of the matrix, G_m, was calculated using the expression $G_m = E_m/(2(1 + \nu_m))$ where E_m and ν_m are the Young's modulus and Poisson's ratio of the matrix, respectively [14]. The fiber length used for the composite fabrication was equal to 15 mm.

3. Photoelastic model and resin calibration

To know the stress distribution around a curved inclusion in an infinite media, when the material was subjected to a tensile load, a photoelastic analysis was performed. It is convenient to mention that this photoelastic as well as a finite element analysis, to be mentioned latter, were performed not to measure the actual stress at the fiber-matrix interface, but rather to identify the distribution of the stress components around the curved fiber (inclusion). The resin selected to make the model was an epoxy, Bisphenol A, DER 331 from DOW Chemical because of its excellent photoelastic properties. The curing agent used was an aliphatic amine, Ancamine 1784 from Air Products and Chemicals, Inc., using 60% w/w ratio with the resin. After mixing and degassing, the resin was poured in silicon mold to fabricate a disk with a diameter D equal to 44.6 mm. To simulate a curved fiber inclusion, a piece of copper wire of 0.32 mm of diameter was used. The composite single inclusion sample was an ASTM standard tensile test dog bone shaped specimen. It was also casted in a silicon mold. First, the resin was poured to fill half the mold cavity and when the resin started to gel, the wire was carefully placed in the cavity and then the mold was filled with the resin and allowed to cure at room temperature for 48 hours.

The principal-stress difference ($\sigma_1 - \sigma_2$) at each point in the model is proportional to the induced birefringence at the point. The constant of proportionality was determined using a well-known method of a disk loaded in diametric compression. The isochromatic pattern is related to the stress system by the stress-optic law (Equation (1)):

$$\sigma_1 - \sigma_2 = \frac{Nf_\sigma}{t} \tag{1}$$

where f_σ is the stress-optical coefficient, a constant that depends upon the model material and the wavelength of light employed, t is the model thickness, and N is the relative retardation of rays forming the pattern. The term N is also known as an isochromatic fringe order. The state of stress at the center of the disk is known [20] and substituting in Equation (1), the stress-optical coefficient fσ is given by Equation (2):

$$f_\sigma = \frac{8P}{\pi DN} \tag{2}$$

where P is the diametral compression force and D is the diameter of the disk.

Then, the maximum shear stress in the plane is obtained relating the fringes to fringe order by Equation (3):

$$\tau_{max} = \frac{\sigma_1 - \sigma_2}{2} = \frac{Nf_\sigma}{2t} \tag{3}$$

4. Finite element analysis

As mentioned previously, a finite element analysis was also performed together with the photoelastic analysis. Figure 1 shows the finite element model and the boundary conditions used for the single curved fiber inclusion. A commercial finite element code was used (NISA Ver. 15.0) using rectangular four-node isoparametric elements. A total of 20 706 nodes and 20 400 elements were used and the material properties were supposed to be homogeneous and isotropic and an elastic plane stress analysis was assumed within the framework of small displacement theory. Perfect adhesion was assumed at the fiber-matrix interphase, that is, only two faces are considered, the fiber and the matrix. The material properties used were: for the matrix, E_m = 1032 MPa, Poisson's ratio ν_m equal to 0.38 and the inclusion, E_{f1} = 11.772 GPa, E_{f2} = 1.1772 GPa Poisson's ratio ν_f equal to 0.35. The shear modulus in both materials was calculated using $G = E/(2(1 + \nu))$. Special care was taken during meshing to avoid (or, at least, to reduce to a minimum) distorted elements, particularly at the ends of the inclusion.

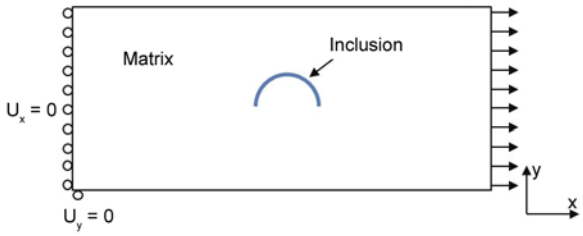

Figure 1. Finite element model and the boundary conditions used to for the single curved fiber inclusion

5. Fiber–matrix adhesion characterization and the interphase

The concept of interphase is the geometrical surface of the classic fiber-matrix contact as well as the region of finite volume extending therefrom, wherein the chemical, physical and mechanical properties vary either continuously or in a stepwise manner between those of the bulk fiber and matrix material. Experimental methods for characterization of the fiber-matrix interface are based on the measurement of the adhesion of a single fiber. The fiber-fragment critical length and the interfacial shear strength can be measured using the Single fiber Fragmentation Test (SFFT). This technique consists of a single fiber embedded in a polymer matrix dog bone shaped specimen tensile specimen. During application of the load, the tensile stress in the fiber increases and fragmentation occurs at points where its tensile strength σ_f is reached. This fragmentation process continues as the applied stress σ_0 is increasing. At some point, the fiber fragments are so short that the stress transferred to the fiber through the interface is not enough to cause any further fiber failure. When this happens, it can be said that the critical fiber fragment length l_c has been reached. To a first approximation, the interfacial shear strength (τ) is calculated from a simple equation obtained from a force balance on a fragment of fiber and, recognizing the random nature of the fiber fragmentation process, the expression is given by Equation (4) [21]:

$$\tau = \frac{\sigma_f}{2\eta}\Gamma\left(1 - \frac{1}{\alpha}\right) \tag{4}$$

where σ_f is the tensile strength of the fiber, α and η are Weibull scale and shape parameters and Γ is the Gamma function.

6. Modelling of micromechanical properties

The rule of mixtures was also modified by Fukuda-Chou [15] to predict the strength of a fiber reinforced composite when both, the fiber length and orientation varies. For a continuous unidirectional fiber developed using the assumption of equal strain in both matrix and fiber, the rule of mixtures is expressed by Equation (5):

$$\sigma_{cu} = \sigma_{fu}V_f + \sigma_m(1 - V_f) \tag{5}$$

where σ_{cu} and σ_{fu} represent the ultimate strength of the composite and fiver respectively, V_f denotes the fiber volume fraction σ_m is the matrix strength upon failure of the composite. In the case of short unidirectional fibers, is expressed by Equation (6):

$$\sigma_{cu} = \sigma_{fu}V_f F(l_c/\bar{l}) + \sigma_m(1 - V_f) \tag{6}$$

where the factor $F(l_c/\bar{l})$ is added to consider the effect of the fiber length l_c and $\bar{l}$ represent the critical length and the average fiber length respectively. If a constant uniform shear stress and a uniform fiber length are assumed, this factor is given by Equation (7):

$$F(l_c/\bar{l})\begin{cases} = 1 - \dfrac{l_c}{2\bar{l}} & (\bar{l} > l_c) \\ = \dfrac{\bar{l}}{2l_c} & (\bar{l} < l_c) \end{cases} \tag{7}$$

If the fiber length is not uniform, Equation (6) must be modified. Considering the manufacturing processes used for composite materials, there is a variation, not only of the fiber length but of the fiber orientation too. In the case of randomly oriented fibers, the rule of mixtures is further modified as shown by Equation (8):

$$\sigma_{cu} = \sigma_{fu}V_f F(l_c/\bar{l})C_0 + \sigma_m(1 - V_f) \tag{8}$$

where C_0 is the factor of fiber orientation. The importance of the factors $F(l_c/\bar{l})$, and C_0, are important for the discussion in this paper. Fukuda and Chou [15] also proposed the expansion of the concept of 'critical zone' to predict the strength of composites reinforced with randomly fibers reinforced with short fibers with variable fiber orientation and length. The critical zone is defined by means of a pair of planes separated by a distance $\beta\bar{l}$, where β is a constant value less than one and $\bar{l}$, is the average length of the fiber crossing a plane normal to the tensile stress applied and aligned with the fiber. The length and orientation of the fiber were considered introducing a probability density function of the fiber length $h(l)$, together with probability density function of fiber orientation $g(\theta)$, and then, the strength of the composite material was also given in the form of a probability density function by Equation (9):

$$\sigma_{cu} = \sigma_{fu} V_f \int_{\theta_0}^{\pi/2} g(\theta)\cos\theta d\theta \int_0^{\theta_0} g(\theta)\cos^3\theta d\theta \cdot \int_{\beta\bar{l}}^{\infty} \left[\int_0^{\theta_0} \left(1 - \frac{\beta\bar{l}}{l\cos\theta}\right) g(\theta) d\theta \right] h(l) dl \cdot$$
$$\cdot \left[\int_{\beta 1}^{l_c} \frac{l}{2l_c} h(l) dl + \int_{l_c}^{\infty} \left(1 - \frac{l_c}{2l}\right) h(l) dl \right] + \sigma_m (1 - V_f) \quad (9)$$

This is a general expression for the strength of a short fiber reinforced composite. In this case, to analyze a particular composite material it is necessary to know the functions $g(\theta)$ and $h(l)$ as well as σ_{fu}, σ_m, V_f and l_c. In the case of a unidirectional and uniform fiber length (case 1), this expression was reduced to Equations (10) and (11):

$$\sigma_{cu} = \sigma_{fu} V_f (1-\beta)\left(1 - \frac{l_c}{2\bar{l}}\right) + \sigma_m (1 - V_f) \quad (\bar{l} > lc) \quad (10)$$

$$\sigma_{cu} = \sigma_{fu} V_f (1-\beta)\frac{l_c}{2\bar{l}} + \sigma_m (1 - V_f) \quad (\bar{l} < lc) \quad (11)$$

In the case of unidirectional distributed fiber length (case 2), $\beta \to 0$, we get Equation (12):

$$\sigma_{cu} = \sigma_{fu} V_f \left[\int_0^{l_c} \frac{l}{2l_c} h(l) dl + \int_{l_c}^{\infty} \left(1 - \frac{l_c}{2l}\right) h(l) dl \right] + + \sigma_m (1 - V_f) \quad (12)$$

and in the case of random orientation, uniform fiber length, and longer than the critical length we get Equation (13):

$$\sigma_{cu} = \sigma_{fu} V_f \left(1 - \frac{l_c}{2l}\right) \int_{\theta_0}^{\pi/2} g(\theta)\cos\theta d\theta \int_0^{\theta_0} g(\theta)\cos^3\theta d\theta \int_0^{\theta_0} \left(1 - \frac{\beta\bar{l}}{\cos\theta}\right) g(\theta) d\theta + \sigma_m (1 - V_f) \quad (13)$$

If C_0 is defined, for a constant value of $g(\theta) = 2/\pi$, as shown by Equation (14):

$$C_0 = \frac{4}{\pi^2}\frac{2+\beta^2}{3}(1-\beta^2)^{1/2} \cdot \cdot \frac{2}{\pi}\left[\cos^{-1}\beta - \frac{1}{2}\beta \log\frac{1+(1-\beta^2)^{1/2}}{1-(1-\beta^2)^{1/2}}\right] \quad (14)$$

and in the limiting case, $\beta \to \infty$, $C_0 \to 0.27$. Figure 2 shows a plot of C_0 as a function of β.

In the case of the elastic modulus of the short fiber reinforced composites, Fukuda and Kawata [14] analyzed the load transfer mechanism from fiber to matrix in a single fiber model using the theory of elasticity, assuming that the interactions between fibers were negligible, and expressed as a relative modulus value K_c with respect to the matrix modulus by Equation (15):

$$K_c = \frac{E_f}{E_m} R_0 C_a V_f + (1 - V_f) \quad (15)$$

where R_0 is given by Equation (16) and C_a by Equation (17):

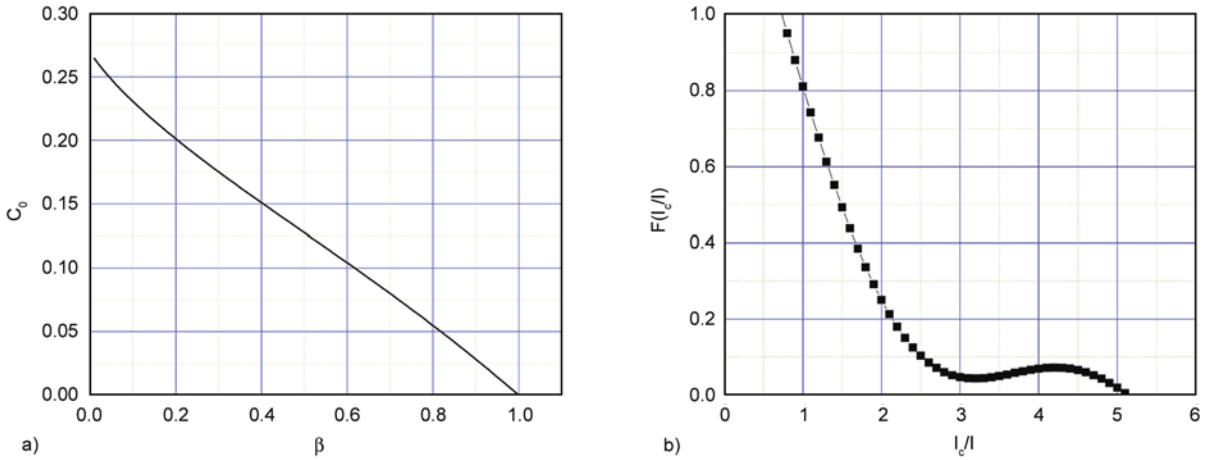

Figure 2. (a) Orientation factor of the fiber C_0 for random fiber orientation; (b) effect of fiber length on composite strength

$$R_0 = \frac{-\frac{2}{W_f}\frac{\pi}{3+2\nu-\nu^2}\int_0^{\infty}\left(l\int_0^1 \bar{\sigma}_1(u)\mathrm{d}u\right)h(l)\mathrm{d}l}{\frac{E_f}{E_m}} \quad (16)$$

$$C_a = \int_0^{\pi/2} g(\theta)\cos\theta \mathrm{d}\theta \int_0^{\theta_0} f(\theta)g(\theta)\cos\theta \mathrm{d}\theta \quad (17)$$

It should be noted that K_c is independent of the fiber length. When the short fibers are unidirectionally aligned, in the x-direction, $g(\theta)$ converts into the Dirac delta value δ which possess a singularity at $\theta = 0$, and C_a is equal to unity. When the fibers are randomly oriented, C_a is less than one and when the fibers are unidirectionally aligned, equal to one. C_a is regarded as the coefficient of reduction of Young's modulus. R_0 shows the degree of Young's modulus caused by the length of the fiber. When $\alpha_0 = \pi/2$, the fiber distribution is random C_a has a value equal to 0.23.

7. Results and discussion

Figure 3 shows photographs of the fibers in the fibers inside the composite materials, for each of the different fiber surface treatments. The curvature of each fiber was represented with the A/L ratio. Here A is the amplitude of the curve and L is the fiber span from end to end. When A tends to zero, the fiber approaches a straight line, that is, the curvature decreases. Typically, fiber fragment lengths are measured using microscopy techniques after dissolving the matrix. However, in this case, these photographs were taken to show that there are fibers whose shape is not straight and any dissolution and handling might change such curved shape. This curvature exhibited by the fibers, is especially noticeable in photographs of FIB, FIBNA and FIBNAPRE composites. The fiber fragments from FIBNASIL do not show a noticeable curvature.

The values of interfacial shear strength, and fiber-fragment critical length and tensile properties as a function of the different fiber surface treatments obtained from the SFFT are shown in Table 3. When the fiber surface topography was modified with the alkaline treatment, (FIBNA), a 10% increase of IFFS was noticed. When the surface-modified fiber was pre-impregnated, a 50% increase was observed. The treatment with the silane coupling agent results in more impressive results. In the case of FIBNASIL (a combination of mechanical and chemical bonding mechanisms) results in an IFFS increase of more than 160%.

The importance of the chemical bonding is notorious as observed from the higher IFFS increments. Similar observations can be made with the fiber-fragment critical lengths, instead of increments, shorter lengths or fiber aspect ratios are observed for stronger IFFS values. One of the advantages of the single fiber fragmentation test is that the experimental parameter which is actually measured in the test is the fiber-fragment critical length [21, 22].

Optimum mechanical properties in composite materials are strongly related to the efficiency of load transfer. The critical length l_c in composites is a parameter which is an indicator of the amount of stress transferred to the fiber: a fiber whose aspect ratio $s = l/d_f$ (where d_f is the fiber diameter) is much greater than the critical aspect ratio $s_c = l_c/d_f$ strengthens the material, while a fiber whose aspect ratio is much smaller than the critical aspect ratio is more likely to weaken the material [23, 24]. Therefore, a good understanding of the factors which influence the critical aspect ratio in order to design optimum continuous or short-fiber composites either is important [25–29].

The effect of the interfacial quality between henequen short, randomly oriented in a matrix of HDPE and its effect on the tensile strength of the composite for various surface treatments is shown in Table 3.

Again, the effect of fiber surface morphology modification results in increments of approximately 11.7%, however, the effect of chemical bonding is

Table 3. Fiber critical length, tensile strength, fiber aspect ratio and interfacial shear strength obtained for the different surface treatments (*Tensile strength increase [%] with fiber surface treatment with respect to FIB)

Fiber surface treatment	Micromechanical results			Macromechanical results	
	Critical length [mm]	Fiber aspect ratio l_c/d_f	IFSS SFFT [MPa]	Tensile strength [MPa]	Young's modulus [MPa]
FIB	12.96	72.00	5.4	20.80	891.00
FIBNA	9.25	51.38	6.0 (11%)*	21.00 (1%)*	945.00
FIBNAPRE	6.00	33.33	9.2 (70%)*	23.25 (12%)*	945.00
FIBNASIL	3.50	19.44	16.0 (196%)*	27.00 (30%)*	873.00

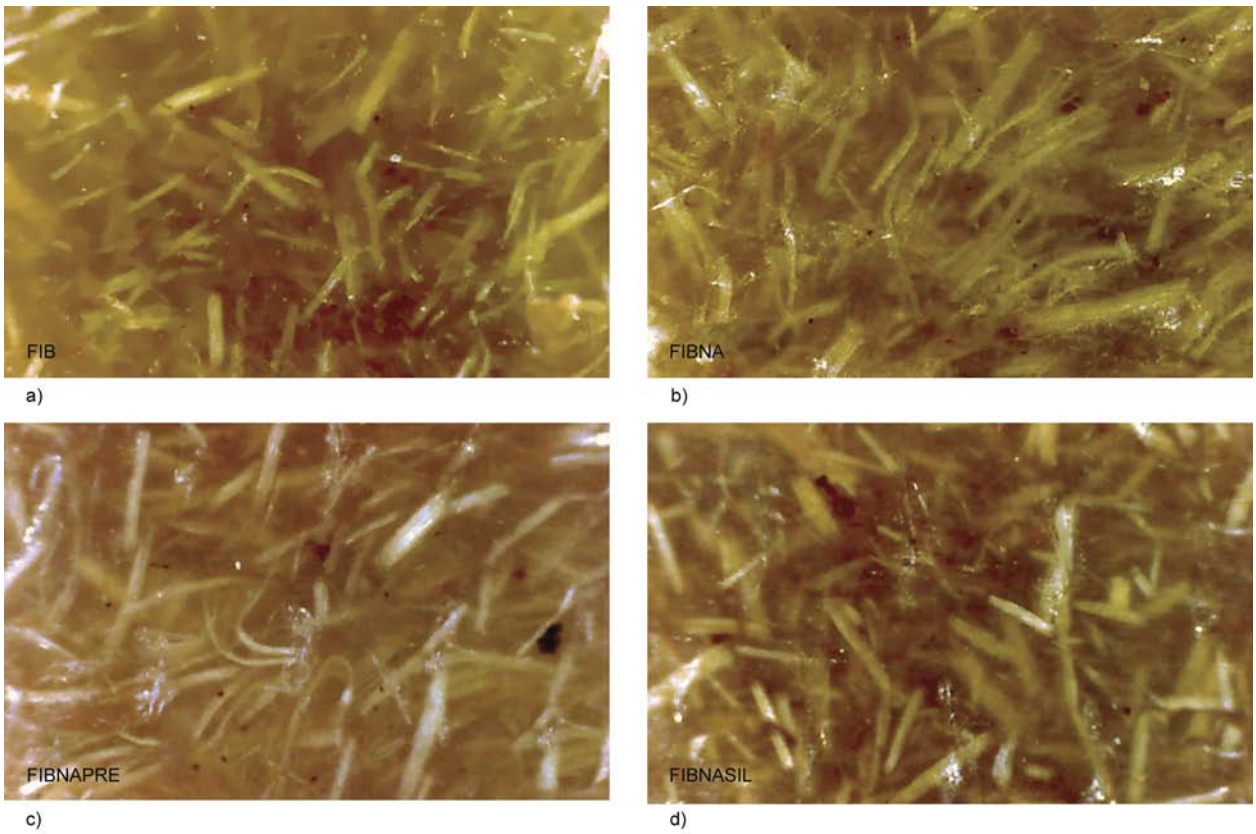

Figure 3. Photographs of fibers inside the composite laminates of FIB, FIBNA, FIBNAPRE and FIBNASIL showing the curved fibers, especially for the first three cases

close to a 30%, that is, three times higher than the mechanical bonding. It should be noticed that the increments of IFSS and tensile strength for each fiber surface treatment with respect to FIB are shown in parenthesis in Table 3. It should also be noticed that the improvements in the IFSS measured obtained with the fiber surface treatments are not reflected in the same increments in the macromechanical properties. The measured values for Young's modulus, on the other hand, were not sensitive to the fiber surface treatments as demonstrated by previous reports [7].

7.1. Analysis of stress transfer in a curved fiber

The optimum mechanical properties in composite materials are strongly related to the load transfer efficiency between fiber and matrix. This is especially true in the case of polymeric matrices which are viscoelastic at all temperatures [22]. Other factors that govern the intrinsic properties include fiber architecture, fiber geometry, fiber orientation, packing arrangement and fiber volume fractions, and fiber-matrix quality, determine many composite properties, particularly mechanical properties. Additionally, the complex state of stress near fiber fragment ends make the modelling of the mechanical behavior of a natural fiber reinforced composite extremely difficult. One parameter that is usually omitted in most of the micromechanical models is the flexibility of the fiber that results in bent or twisted fibers after processing of the composite. A natural fiber will easily bend in the composite as a result of the high shear stresses resulting from the extrusion and/or injection molding process. With this in mind it is reasonable to think that the micromechanical models require an adjustment factor that takes into account the presence of curvature of the natural fiber to be able to more precisely estimate the mechanical properties of the composite. Although there are reports in the literature that consider other factors that contribute to the theoretical, these results do not conform to the experimental values [25–29]. Furthermore, the structure and composition of a natural fiber allows the formation of failure surfaces because of their microfibrillar and hollow nature and to the irregular shape of their cross section. Also, it should be remembered that henequen fiber itself is a composite with cellulose microfibrils embedded in a lignin matrix and that such microfibrils are not oriented perfectly aligned with the fiber axis, and

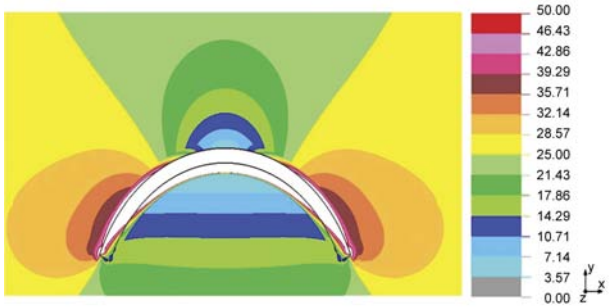

Figure 4. Shows the σ_{xx} stress components distribution around the curved fiber obtained from the finite element analysis

instead, they form a helical pattern along the fiber's length [1].

Figure 4 shows the σ_{xx} distribution and Figure 5 shows the finite element and photoelasticity models, maximum shear stress τ_{max}, around the curved fiber (seen in white color). As it can be appreciated, the state of stress around the curved fiber is very complex. In Figure 4, it can be seen that the tensile stress σ_{xx} in the matrix and at the fiber matrix interface is positive in the direction of the applied load. But the stress distribution on the convex side is different from the stress distribution on the concave side of the fiber. This tensile stress is acting almost perpendicularly to the fiber ends as shown by the two lobes on the convex sides. A more uniform distribution of σ_{xx} is noted in the matrix, on the concave side of the fiber but still trying to separate the fiber from the matrix, especially at the fiber ends.

Figure 5 shows finite elements and isochromatic fringes from a photoelastic model of a curved fiber embedded in a resin matrix, subjected to a tensile

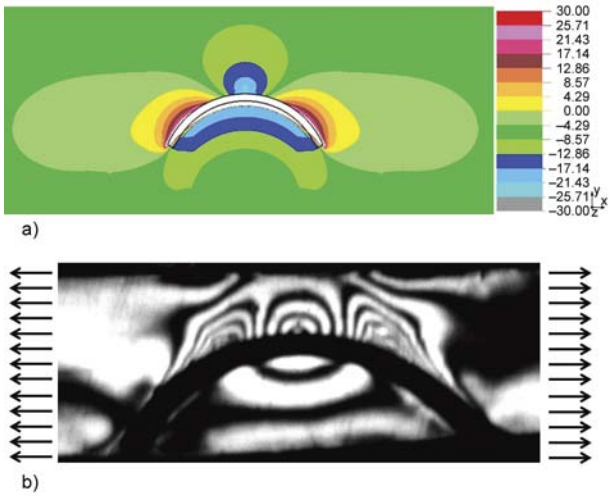

Figure 5. Loci of $(\sigma_1 - \sigma_2)$, that is, τ_{max}, the maximum shear stress from (a) finite element and (b) photoelasticity models, around the curved fiber

load. Isochromatics are the loci of the points along which the difference in the first and second principal stress remains the same [30]. Thus they are the lines which join the points with equal maximum shear stress magnitude. It should be noticed that the number of fringes on the convex side of the fiber is higher than the number on the concave side. Then, it can be said that the shear stress on the convex side of the curved fiber is different from the shear stress on the concave. The graph (Figure 5b) shows a plot of the shear stress τi normalized by the far-field tensile stress σ_0 versus the position along the curved fiber and normalized by the fiber diameter, plotted in a straight line. Along the convex side, three stress discontinuities are observed whereas on the concave side, only one is observed and that their relative magnitude is different but on the concave side is lower. Then, it can be said that, when a fiber is bent the interfacial shear stress induced by the externally applied load will be different along its length depending on its geometry.

Figures 6 to 8 shows plots for the σ_{xx} ,σ_{yy} and τ_{max} stress components along the fiber-matrix interface on the concave and convex sides of the curved fiber. Figure 6 the normal stress in the center line of the curved fiber in the direction of the applied load. The state of stress and the distribution of the different components on the curved fiber should be discussed considering two different parameter of the composite material. The first is the quality of the fiber-matrix interphase and the second is the inherent anisotropy of the natural fiber.

When the level of adhesion between fiber and matrix is low as in the case of the composite made with FIB, the shear stress on both, concave and convex sides will soon produce failure because there is and added stress component contributing to the separation of the fiber from the matrix, that is, σ_{xx} on the concave side especially on the central portion and σ_{yy}, although smaller than σ_{xx}, still acting to separate fiber from matrix.

When the frictional adhesion is increased as in the case of FIBNA and FIBNAPRE, the amount of polymer penetrating the fiber crevices increases and the upper bound of the interphase strength will be dictated by the shear strength of the matrix. In these cases, there should also be some matrix tearing depending on the degree of entanglement with the outer layer of the fiber. This type of failure could be attributed to the normal stress components at the

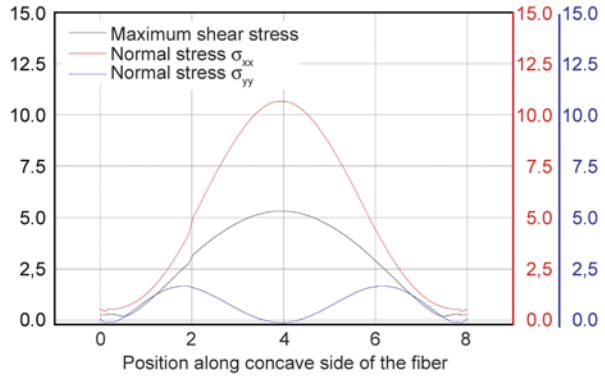

Figure 6. Variation of stress components along the concave side of the curved fiber

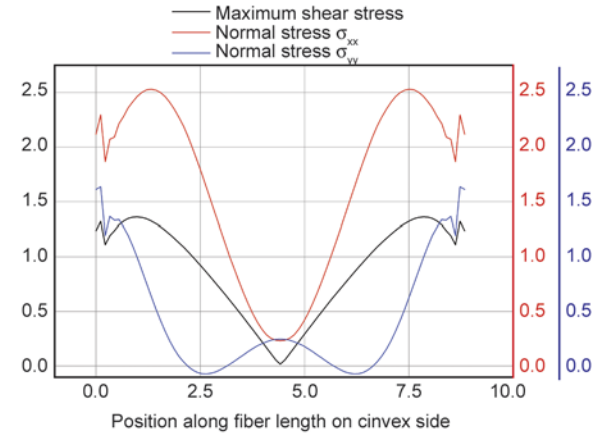

Figure 7. Variation of stress components along the convex side of the curved fiber

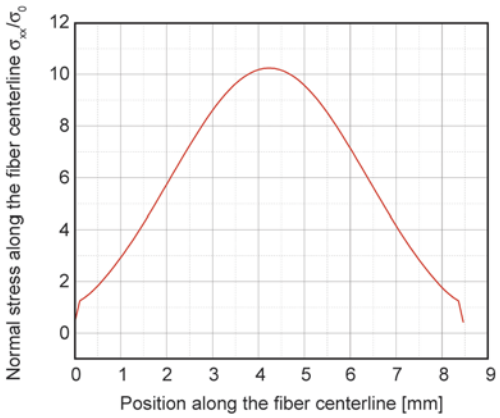

Figure 8. Normal stresses in the center line of the curved fiber in the direction of the applied load

interphase. The formation of covalent bonds in the case of FIBNASIL, contributes to the formation of bridges between fiber and matrix which will better resist the action of both normal and shear stress components.

As seen in Figure 8, the effective length could be considered to be achieved only in the central portion of the curved fiber. In fact, it can be seen in Figures 6–8 that the stresses are higher in approximately one third of the total length of the curve fiber, either at the central portion or at both ends. Therefore, the contribution of the fiber to strength will be limited to only portions where the stress transmission is more efficient. It has been reported for jute fibers, that this type of fibers exhibited significant elastic and thermal expansion anisotropy. The fiber's longitudinal Young's modulus E_{1f} was estimated to range between 5 and 10 times that of its transverse modulus E_{2f} over the temperature range –50 to 50°C [31]. A similar behavior is expected for the henequen fibers, at least from the anisotropic point of view. Because of the curvature and depending on the orientation of the bent fiber with respect to the applied load, the fiber's longitudinal Young's modulus E_{1f} will form an angle with the applied load. This should reduce the contribution of the fiber to both modulus and strength depending on cosine of the angle θ formed by fiber longitudinal axis and the direction of the load. Furthermore, when the value of θ increases, the normal radial component of the applied load also increases in the radial direction of the fiber but its modulus and strength are much lower than the longitudinal value.

These differences in the state of stress along the bent fiber can be explained from a simple force resolution considering the angle between the direction of the applied load and the tangential line on any point along the fiber surface (see Figure 7). One component will be responsible of the interface shear stress, whereas the other component of a normal stress component in a radial direction. It should be noted that the relative magnitude of these stress components will vary from one point to another along the curved fiber. The radial normal stress component should be held responsible for any defibrillation damage to the natural fiber. In the case of FIB, since fiber-matrix adhesion is low, interface debonding is expected and then, no defibrillation damage is observed, but as the adhesion level increases, defibrillation will increase, especially when there is a good fiber wetting. Additionally, the effective length of stress transfer of the bent fiber is not symmetrical nor it is acting on both of its sides. Therefore, this behavior results in a lower stress transfer efficiency as that observed with rigid, stiff fibers which remain straight after processing [32, 33].

7.2. Results from the micromechanical models by Fukuda

According to the finite element and photoelastic analysis, there seems to be three different portions of reinforcing efficiency of the curved fiber. The inherent anisotropy of the fiber, as shown in Figure 9, can be considered as a composite material with two main material directions. Therefore, considering that the fiber is subjected to different loading conditions, it could be discretized into a number of straight segments, that is, it could be considered equivalent to three different straight fibers with their materials directions according to the curvature. Then, with equivalence if the bent fiber is close to the critical length, it is then possible to consider a ratio ($l_c/\bar{l}$) equal to 3.

Then in Figure 2b, it would result in an asymptotic value for $F(l_c/\bar{l})$ of approximately 0.20. The experimental tensile mechanical properties of the short-natural fiber composites and the theoretical ones, estimated with the Fukuda-Chou and the Fukuda-Kawata models are shown in Tables 4 and 5. The composite tensile strength was calculated with the Fukuda-Chou model considering two approaches: i) that the natural fiber behaves as straight one, and ii) recognizing their inherent flexibility that curve it during processing. For the calculations, the value of was estimated to be 7.5 mm, and considering an efficiency in one third of the length, the new $\bar{l}$ decreases to 2.5 mm. The corrected values of $F(l_c/\bar{l})$ of are used to recalculate the value of the tensile strength. As it can be seen in Table 4 and Figure 10, the theoretical results for the composite strength according to the equation developed by Fukuda-Chou shows better agreement with the experimental results using the corrected effective length due the fiber curvature compared with the direct approach (straight fiber). In another hand, it is evident that there is a better agreement with both approaches for the strong fiber-matrix adhesion composite (FIBNASIL) compared with the other composites, and in fact there is a slight overestimation. It should be remembered that there are factors which are not taken into account in the development of the model. Among them, the stress concentration caused by the early separation of the fibers from the matrix that should results in larger stress concentration factors which are not taken into account anywhere in the theoretical development.

Table 5 shows the values for Young's modulus calculated using Fukuda-Kawata model. In this case the estimated value shows good agreement with the experimental results, but the values were slightly lower than the measured values.

The small inconsistencies found between the experimental and theoretical results could be attributed to the inherent variability in cross-section area, physical and mechanical properties of the natural fibers (a therefore of both, their non-circular cross section and the equivalent diameter), resulting in variations of the fiber aspect ratio and in differences between the experimental and theoretical mechanical properties.

The curvature of natural fibers resulting from their flexibility and the severe stresses during processing

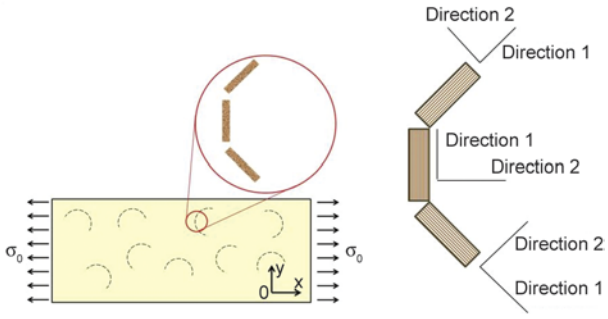

Figure 9. Discretization of a single curved fiber in three straight segments

Table 5. Young's modulus calculated utilizing the Fukuda-Kawata model

	Experimental [MPa]	C_a	R_0	Fukuda-Kawata [MPa]
FIB	891	0.23	0.38	837
FIBNA	945	0.23	0.38	837
FIBNAPRE	945	0.23	0.38	837
FIBNASIL	873	0.23	0.38	837

Table 4. Tensile strength calculated utilizing the Fukuda-Chou model

	Experimental [MPa]	Fukuda-Chou straight fibers			Fukuda-Chou curved fibers		
		C_0	$F(l_c/\bar{l})$	Tensile strength [MPa]	C_0	$F(l_c/\bar{l})$	Tensile strength [MPa]
FIB	20.80	0.20	0.38	29.60	0.05	0.2	25.30
FIBNA	21.00	0.20	0.42	30.67	0.08	0.2	25.70
FIBNAPRE	23.25	0.20	0.55	33.10	0.16	0.2	26.91
FIBNASIL	27.00	0.20	0.70	35.92	0.38	0.2	30.18

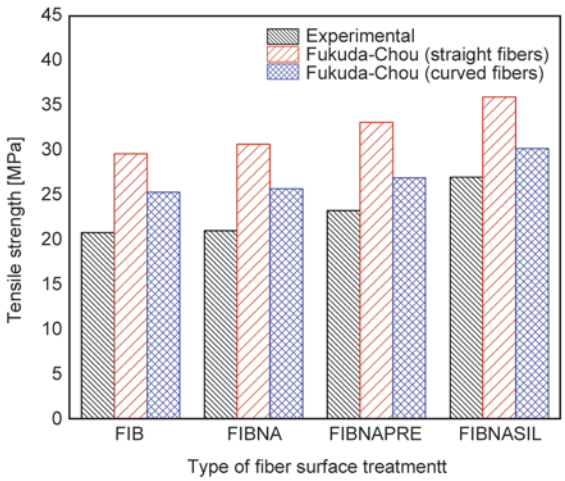

Figure 10. Comparison of the experimental tensile strength with values calculated using the Fukuda-Chou model

is a feature that it is very difficult to control directly but it can be done indirectly by improving the fiber-matrix interfacial adhesion. As it has been observed, when the interfacial adhesion is very strong, the critical fiber length is short and the critical fiber aspect ratio also decreases and the fiber fragments tend to remain straight during the processing of the composite. In this case, the fibers with the FIBNASIL surface treatment, the fiber curvature was very low after processing.

8. Conclusions

From the photoelastic and finite element analysis, it was seen that the state of stress around a curved fiber inclusion is very complex. It was noticeable that the stress distribution was more uniform in the concave side of the fiber and more complex on the convex side of the curved fiber. It was also noticed that on the convex side of the curved fiber inclusion, there are three distinctive regions along the fiber and that the 'effective fiber length' is very short of approximately one third the average length. The models proposed by Fukuda and based on the probability of length and orientation distribution; they seem to be very convenient to calculate the effective mechanical properties of the composite. This fiber length of higher stress transfer was used to correct the value of the fiber efficiency to recalculate the tensile strength of the composite laminate. Much better agreement was obtained after decreasing the fiber efficiency by using an average length value to compensate for the fiber curvature in the strength properties specially, also, the best agreement between the predicted and the experimental values was observed with the fiber-matrix system subjected to surface treatment with both mechanical and chemical bonding being this the best combination to get the most effective mechanical properties of the composite. Then, prediction of the tensile mechanical properties using the micromechanical models proposed by Fukuda-Kawata and coworkers, would be reasonable if the curved fiber is considered equivalent to two or three shorter straight fiber fragments to estimate the reinforcing efficiency in the composite.

Acknowledgements

The authors would like to thank Consejo Nacional de Ciencia y Tecnología for the grant through project U42432-K and Mr. Miguel A. Escalante-Solís is grateful for the doctoral scholarship granted to him.

References

[1] Herrera-Franco P. J., Valadez-Gonzalez A.: Mechanical properties of continuous natural fibre-reinforced polymer composites. Composites Part A: Applied Science and Manufacturing, **35**, 339–345 (2004). DOI: 10.1016/j.compositesa.2003.09.012

[2] Ku H., Wang H., Pattarachaiyakoop N., Trada M.: A review on the tensile properties of natural fiber reinforced polymer composites. Composites Part B: Engineering, **42**, 856–873 (2011). DOI: 10.1016/j.compositesb.2011.01.010

[3] Sawpan M. A., Pickering K. L., Fernyhough A.: Effect of fibre treatments on interfacial shear strength of hemp fibre reinforced polylactide and unsaturated polyester composites. Composites Part A: Applied Science and Manufacturing, **42**, 1189–1196 (2011). DOI: 10.1016/j.compositesa.2011.05.003

[4] Yue C. Y., Cheung W. L.: Interfacial properties of fibre-reinforced composites. Journal of Materials Science, **27**, 3843–3855 (1992). DOI: 10.1007/BF00545467

[5] Anumandla V., Gibson R. F.: A comprehensive closed form micromechanics model for estimating the elastic modulus of nanotube-reinforced composites. Composites Part A: Applied Science and Manufacturing, **37**, 2178–2185 (2006). DOI: 10.1016/j.compositesa.2005.09.016

[6] Kalaprasad G., Joseph K., Thomas S., Pavithran C.: Theoretical modelling of tensile properties of short sisal fibre-reinforced low-density polyethylene composites. Journal of Materials Science, **32**, 4261–4267 (1997). DOI: 10.1023/A:1018651218515

[7] George J., Sreekala M. S., Thomas S.: A review on interface modification and characterization of natural fiber reinforced plastic composites. Polymer Engineering and Science, **41**, 1471–1485 (2001). DOI: 10.1002/pen.10846

[8] Bowyer W. H., Bader M. G.: On the re-inforcement of thermoplastics by imperfectly aligned discontinuous fibres. Journal of Materials Science, **7**, 1315–1321 (1972). DOI: 10.1007/BF00550698

[9] Nairn J. A.: Exact and variational theorems for fracture mechanics of composites with residual stresses, traction-loaded cracks, and imperfect interfaces. International Journal of Fracture, **105**, 243–271 (2000). DOI: 10.1023/A:1007666426275

[10] Simonsen J.: Efficiency of reinforcing materials in filled polymer composites. Forest Products Journal, **47**, 74–81 (1997).

[11] Doan T-T-L., Gao S-L., Mäder E.: Jute/polypropylene composites I. Effect of matrix modification. Composites Science and Technology, **66**, 952–963 (2006). DOI: 10.1016/j.compscitech.2005.08.009

[12] Beckermann G. W., Pickering K. L.: Engineering and evaluation of hemp fibre reinforced polypropylene composites: Fibre treatment and matrix modification. Composites Part A: Applied Science and Manufacturing, **39**, 979–988 (2008). DOI: 10.1016/j.compositesa.2008.03.010

[13] Herrera-Franco P. J., Valadez-Gonzalez A.: A study of the mechanical properties of short natural-fiber reinforced composites. Composites Part B: Engineering, **36**, 597–608 (2005). DOI: 10.1016/j.compositesb.2005.04.001

[14] Fukuda H., Kawata K.: On Young's modulus of short fibre composites. Fibre Science and Technology, **7**, 207–222 (1974). DOI: 10.1016/0015-0568(74)90018-9

[15] Fukuda H., Chou T-W.: A probabilistic theory for the strength of short fibre composites. Journal of Materials Science, **16**, 1088–1096 (1981). DOI: 10.1007/BF00542756

[16] Joffe R., Andersons J., Wallström L.: Strength and adhesion characteristics of elementary flax fibres with different surface treatments. Composites Part A: Applied Science and Manufacturing, **34**, 603–612 (2003). DOI: 10.1016/S1359-835X(03)00099-X

[17] Abdelmouleh M., Boufi S., ben Salah A., Belgacem M. N., Gandini A.: Interaction of silane coupling agents with cellulose. Langmuir, **18**, 3203–3208 (2002). DOI: 10.1021/la011657g

[18] Brochier M-C., Abdelmouleh S., M., Boufi S., Belgacem M. N., Gandini A.: Silane adsorption onto cellulose fibers: Hydrolysis and condensation reactions. Journal of Colloid and Interface Science, **289**, 249–261 (2005). DOI: 10.1016/j.jcis.2005.03.070

[19] Valadez-Gonzalez A., Cervantes-Uc J. M., Olayo R., Herrera-Franco P. J.: Effect of fiber surface treatment on the fiber–matrix bond strength of natural fiber reinforced composites. Composites Part B: Engineering, **30**, 309–320 (1999). DOI: 10.1016/S1359-8368(98)00054-7

[20] Procopio A. T., Zavaliangos A., Cunningham J. C.: Analysis of the diametrical compression test and the applicability to plastically deforming materials. Journal of Materials Science, **38**, 3629–3639 (2003). DOI: 10.1023/A:1025681432260

[21] Herrera-Franco P. J., Drzal L. T.: Comparison of methods for the measurement of fibre/matrix adhesion in composites. Composites, **3**, 2–27 (1991). DOI: 10.1016/0010-4361(92)90282-Y

[22] Monette L., Anderson M. P., Grest G. S.: The meaning of the critical length concept in composites: Study of matrix viscosity and strain rate on the average fiber fragmentation length in short-fiber polymer composites. Polymer Composites, **14**, 101–105 (1993). DOI: 10.1002/pc.750140204

[23] Joseph K., Thomas S., Pavithran C., Brahmakumar M.: Tensile properties of short sisal fiber-reinforced polyethylene composites. Journal of Applied Polymer Science, **47**, 1731–1739 (1993). DOI: 10.1002/app.1993.070471003

[24] Newman R. H., Hebert P., Dickson A. R., Even D., Fernyhough A., Sandquist D.: Micromechanical modelling for wood–fibre reinforced plastics in which the fibres are neither stiff nor rod-like. Composites Part A: Applied Science and Manufacturing, **65**, 57–63 (2014). DOI: 10.1016/j.compositesa.2014.05.012

[25] van Hattum F. W., Bernardo C. A.: A model to predict the strength of short fiber composites. Polymer Composites, **20**, 524–533 (1999). DOI: 10.1002/pc.10376

[26] Venkateshwaran N., ElayaPerumal A.: Modeling and evaluation of tensile properties of randomly oriented banana/epoxy composite. Journal of Reinforced Plastics and Composites, **30**, 1957–1967 (2011). DOI: 10.1177/0731684411430559

[27] Ulrych F., Sova M., Vokrouhlecky J., Turcic B.: Empirical relations of the mechanical properties of polyamide 6 reinforced with short glass fibers. Polymer Composites, **14**, 229–237 (1993). DOI: 10.1002/pc.750140308

[28] Jones R. M.: Mechanics of composite materials. Taylor and Francis, Miami (1998).

[29] Tucker C. L., Liang E.: Stiffness predictions for unidirectional short-fiber composites: Review and evaluation. Composites Science and Technology, **59**, 655–671 (1999). DOI: 10.1016/S0266-3538(98)00120-1

[30] Dally J. W., Riley W. F.: Experimental stress analysis. McGraw-Hill, New York (1991).

[31] Cichocki Jr. F. R., Thomason J. L.: Thermoelastic anisotropy of a natural fiber. Composites Science and Technology, **62**, 669–678 (2002).
DOI: 10.1016/S0266-3538(02)00011-8

[32] Cazaurang-Martinez M. N., Herrera-Franco P. J., Gonzalez-Chi P. I., Aguilar-Vega M.: Physical and mechanical properties of henequen fibers. Journal of Applied Polymer Science, **43**, 749–756 (1991).
DOI: 10.1002/app.1991.070430412

[33] Manikandan K. C., Diwan S. M., Thomas S.: Tensile properties of short sisal fiber reinforced polystyrene composites. Journal of Applied Polymer Science, **60**, 1483–1497 (1996).
DOI: 10.1002/(SICI)1097-4628(19960531)60:9<1483::AID-APP23>3.0.CO;2-1

eXPRESS Polymer Letters Vol.9, No.12 (2015) 1133–1141
Available online at www.expresspolymlett.com
DOI: 10.3144/expresspolymlett.2015.101

Silane crosslinking of poly(lactic acid): The effect of simultaneous hydrolytic degradation

M. Rahmat[1], I. Ghasemi[1], M. Karrabi[2], H. Azizi[1], M. Zandi[3], M. Riahinezhad[4]*

[1]Department of Plastics, Iran Polymer and Petrochemical Institute, P.O. Box: 14965/115 Tehran, Iran
[2]Department of Rubber, Iran Polymer and Petrochemical Institute, P.O. Box: 14965/115 Tehran, Iran
[3]Department of Biomaterial, Iran Polymer and Petrochemical Institute, P.O. Box: 14965/115 Tehran, Iran
[4]Department of Chemical Engineering, Institute for Polymer Research, University of Waterloo, ON N2L 3G1 Waterloo, Canada

Received 10 June 2015; accepted in revised form 8 August 2015

Abstract. In this work, silane crosslinking of poly (lactic acid) (PLA) was studied. PLA was grafted with vinyltrimethoxysilane (VTMO) via melt mixing in an internal mixer, followed by a crosslinking reaction in hot water for different times. The effect of simultaneous hydrolytic degradation in hot water (70°C) during crosslinking was monitored. Silane grafting of PLA was characterized using mixing torque and gel permeation chromatography (GPC) analysis. The results revealed that by increasing the silane (0–7 wt%) and peroxide (0–0.5 wt%) contents, the degree of grafting was increased. A peak corresponding to higher molecular weight in GPC chromatograms appeared in comparison to pure PLA due to the grafting reaction. Gel content, swelling test, GPC and thermal gravimetric analysis (TGA) were performed to monitor gel structure and concurrent hydrolytic degradation. Results confirmed that the occurrence of hydrolytic degradation during crosslinking and gel content of some samples tended to zero over 10 hr of immersion in hot water. The effect of hydrolytic degradation was not significant up to 10 hr and a tight gel structure was obtained. However, at longer crosslinking times, hydrolytic degradation was the dominant mechanism that leads to network defects.

Keywords: *biodegradable polymers, crosslinking, hydrolytic degradation, poly(lactic acid), silane grafting*

1. Introduction

Recently, poly(lactic acid) (PLA) has been extensively considered by researchers as a suitable candidate to replace some synthetic polymers, due to its good mechanical properties, easy processability, low environmental impact and its renewable resources [1–3]. However, its thermal deformation around 60°C, is an important limitation for some applications require higher temperatures e.g. using PLA in food packaging industry, bottles, medical products [4–6].

Crosslinking could be a good strategy to overcome this disadvantage. Radiation and chemical crosslinking are two well-known methods for osslinking and have been reported in the literatures [7–15].

During radiation crosslinking (electron beam and gamma irradiation), macromolecule radicals (in the presence of multifunctional monomers as triarylisocyanurate) are created in the solid state using high energy beams that produce linkages between the polymer chains. During chemical crosslinking, however, radicals are usually formed by a chemical agent. One of the most common crosslinking agents used in polyethylene are silane compounds [16]. There is a large body of reports on different features of silane crosslinking in polyethylene [17–19]. In this method, grafting of silane molecules is accomplished by peroxide radicals, and then linkages are formed in hot water via hydrolysis and condensation reactions.

*Corresponding author, e-mail: I.ghasemi@ippi.ac.ir

This method was applied to create crosslinked PLA by Han *et al*. [11]. In this study, vinyltrimethoxysilane (VTMO) and vinyltriethoxysilane (VTES) were used and the results showed that siloxane linkage were successfully formed and the thermal and mechanical properties were improved.

One of the limitations of this method for PLA is simultaneous hydrolytic degradation during the crosslinking in hot water [20]. The hydrolysis of PLA in aqueous media starts with the water diffusion between polymer chains in the amorphous phase which are less resistant to the penetration of water molecules, followed by hydrolytic splitting of the ester bonds [1, 21]. Four-stage model was proposed for hydrolytic degradation including diffusion of water, hydrolysis progress producing oligomers, migration and diffusion of the oligomers to the [22]. Effect of specimen's size [23], initial molecular weight [24], crystallinity [25, 26], medium temperature [27], and presence of nano particles [28] on hydrolytic degradation of PLA have been reported. According to literature, it can be concluded that the silane crosslinking may be affected by probable hydrolytic degradation.

The influence of crosslinking on degradability of PLA has been reported and the results indicated that enzyme was less effective towards crosslinked PLA than neat PLA. In other words, the deterioration of the biodegradability of PLA is affected by crosslinking due to reduction of enzyme diffusion in PLA [11, 29].

Södergård *et al*. [30] showed peroxide modifying of PLA with tert-butylperoxybenzoatein melt mixing. Their results suggested more rapid decrease of molecular weight during immersion in water, because of higher permeability for both water and oligomers.

In our group, peroxide crosslinking of PLA was studied before [15]. In this study, silane crosslinking and hydrolytic degradation of PLA was studied as two competitive reactions. Optimization for obtaining the suitable gel structure was the main target of this study followed by the balance between two reactions, crosslinking and hydrolytic degradation. Crosslinking reaction was evaluated using gel content and crosslink density while assessment of degradation was done by gel permeation chromatography (GPC) and thermogravimetric analysis (TGA). The silane and peroxide contents and immersion time were the variable parameters to adjust the formation of network via their effects on two aforesaid reactions.

2. Experimental section

2.1. Materials

Poly(lactic acid), PLA, (IngeoBiopolymer 3251D) was purchased from Nature works LLC, with a melt flow index 30 g/10 min (190°C, 2.16 kg) and a density of 1.24 g/cm^3. Vinyltrimethoxysilane, VTMO (YAC-V171, ≥98% purity) was supplied from Lanyachem and Dicumylperoxide, DCP, (99% purity), obtained from Aldrich, Germany. Tetrahydrofuran, THF, and chloroform solvents were used for determination of gel content, degree of swelling and GPC experiments and were purchased from Merck (USA).

2.2. Preparation of silane grafted PLA

Silane grafting of PLA was accomplished via melt mixing in an internal mixer (Brabender, Germany). The temperature of mixing was 190°C and rotor speed was 75 rpm. At first, PLA was dried in an oven at 80°C for 8 hr afterward it was added to mixing chamber and 30 s after complete melting, solution of DCP in VTMO was poured gradually by syringe (during the 30 s). Mixing was continued for 5 minutes and the obtained compound was immediately compressed at 200°C in a hot press (Toyoseiki, Japan). To avoid premature crosslinking, PLA sheets were stored in desiccators after pressing. The sample and code formulations are depicted in Table 1. In these codes, the number after S denotes VTMO concentrations and the number after D corresponds to DCP contents. Crosslinking of silane grafted PLAs were done in hot water at 70°C for 1, 10 and 20 hr. CP, as control sample, represents processed PLA in the same conditions.

Table 1. Sample names and compositions

Sample name	PLA [phr]	VTMO [phr]	DCP [phr]
CP	100	0	0
S3	100	3	0
D3	100	0	0.3
S3D1	100	3	0.1
S3D3	100	3	0.3
S3D5	100	3	0.5
S5D1	100	5	0.1
S5D3	100	5	0.3
S5D5	100	5	0.5
S7D1	100	7	0.1
S7D3	100	7	0.3
S7D5	100	7	0.5

2.3. Methods

The gel content of the crosslinked PLA was determined using the amount of insoluble material in chloroform after 48 hr. About 0.25 g of a crosslinked polymer was cut into small pieces and placed in a pre-weighed stainless steel finemesh. After the test, the samples were washed with chloroform and dried at room temperature. The gel fraction was calculated as shown in Equation (1):

$$Gel\ fraction\ [\,\%\,] = \frac{M_1}{M_0}\cdot 100 \tag{1}$$

where M_0 and M_1 are the initial weight and residual dried gel content of the crosslinked polymer, respectively.

Degree of swelling (*DS*) at equilibrium condition was measured by immersion of the samples in chloroform at room temperature for 48 hr, according to Equation (2):

$$DS = 1 + \frac{\rho_{\text{polymer}}}{\rho_{\text{cloroform}}}\cdot\left(\frac{W_s}{W_p}\right) \tag{2}$$

where W_s is the weight of solvent in the swollen network, W_p is the weight of dry gel component in the crosslinked PLA and $\rho_{\text{chloroform}}$ and ρ_{polymer} are the specific densities of the solvent and the polymer, respectively.

The degree of swelling was used to measure the average molecular weight between crosslinks ($\bar{M}_c$). The swelling ratio decreases with increasing gel content and decreasing $\bar{M}_c$. According to the theory of Flory and Rehner [31], $\bar{M}_c$ is defined by Equation (3):

$$\frac{1}{\bar{M}_c} = \frac{2}{\bar{M}_n} - \frac{\left(\frac{\bar{v}}{V_1}\right)\left[\ln\left(1-\frac{1}{DS}\right)+\frac{1}{DS}+\chi_{12}\left(\frac{1}{DS}\right)^2\right]}{\frac{1}{\sqrt[3]{DS}}-\frac{1}{2DS}} \tag{3}$$

where $\bar{v}$ is the specific volume of the polymer, v_2 is the volume fraction of the polymer in the swollen mass, V_1 is the molar volume of the solvent (80 $cm^3 \cdot mol^{-1}$), χ_{12} is the Flory solvent-polymer interaction parameter (0.1 as reported in the literature [11]), $\bar{M}_n$ is the primary molecular mass, and $\bar{M}_c$ is the average molecular mass between crosslinks.

The amount of crosslink bonds in a unit volume is known as the crosslink density (v).The crosslink density is related to $\bar{M}_c$ through Equation (4):

$$\upsilon = \frac{\rho_p}{\bar{M}_c} \tag{4}$$

where ρ_p is the density of the polymer.

The average molecular weight and molecular weight distribution of samples were determined using Gel Permeation Chromatography, GPC (Agilent 1100 series, USA) at 23°C. Tetrahydrofuran (THF) was used as the carrier. Flow rate and injection volume were set at 1 $mL \cdot min^{-1}$ and 20 µL, respectively. GPC analysis was only conducted for the sol fraction of the polymer. The sol fraction of samples was extracted using chloroform for 48 hr at room temperature, followed by drying at room temperature and dissolving in THF for chromatography test.

Since the microstructure of silane grafted PLA affects the hydrodynamic volume of the polymer, GPC results give us valuable information on the molecular weight of the modified polymer, in order to evaluate the grafting reaction.

The thermal degradation behavior of the crosslinked PLA was studied by Thermogravimetric Analysis, TGA, (STA 1640, UK). The test was carried out in nitrogen gas atmosphere within a range of 25–60°C at a heating rate of 10 C/min.

3. Results and discussion

The mixing torque in internal mixer is affected by grafting reaction and can be used as an indicator for tracking of the reaction. The mixing torque versus time is demonstrated for all the samples in Figure 1. As can be seen in the Figure, the torque increased for the samples containing VTMO/ DCP solution in comparison to pure PLA and PLA containing VTMO

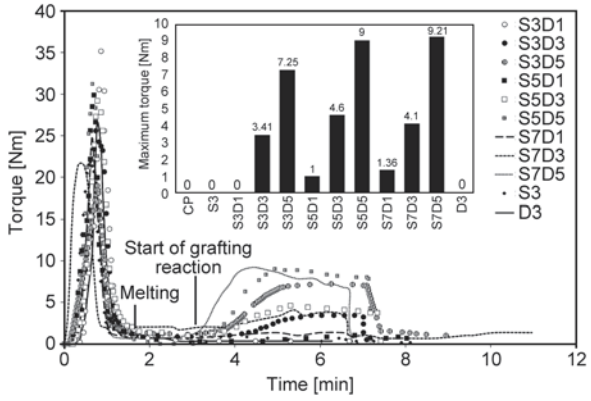

Figure 1. Mixing torque of PLA-silane grafting reaction. The Chart inside the Figure shows maximum torque of the grafting reaction mixing.

and DCP. This behavior may be attributed to the grafting reaction. In other words, grafting reaction caused higher molecular weight and consequently higher viscosity. A gradual reduction of torque during grafting is observed which is related to thermal degradation of PLA in melt mixing process. The sample S7D5 (containing 5 phr DCP and 7 phr VTMO) showed the highest torque which implies to the highest grafting reaction for the sample. On the other hand, there is no considerable increment in torque for some samples including small amount of DCP which indicates to the main and effective role of peroxide in grafting reaction. Similar observation were reported for silane grafting of polyethylene [18] and polypropylene [32].

FTIR spectrum is usually used to confirm the grafting reaction by forming new peaks at 2843 cm^{-1} ($Si–OCH_3$ bond). In our study, this bond was not clearly observed (spectrum is not shown here). Therefore the grafting reaction was monitored by gel content after crosslinking. It is well known that the gel fraction of the samples is formed by the hydrolysis and condensation of grafted silane in hot water.

The gel contents of the samples at different immersion times in hot water are shown in Figure 2. No gel content was obtained for the samples including silane and peroxide individually (S3 and D3), which indicates no grafting and crosslinking reactions occurred in these samples. This is in agreement with the results from Figure 1. It was expected for the sample including silane but for the samples with peroxide there are a contradictory reports. For example, occurrence of crosslinking with peroxide has been reported by Nijenhuis *et al*. [33], while Södergård *et al*. [30] did not find any crosslinking in this case. In addition, in the samples containing DCP/VTMO solution with 0.1% DCP, no gel content was observed even at long immersion time. It seems that a low concentration of DCP cannot generate adequate radicals for grafting reaction and further crosslinking. It is found that having higher DCP contents in the samples improves the gel content.

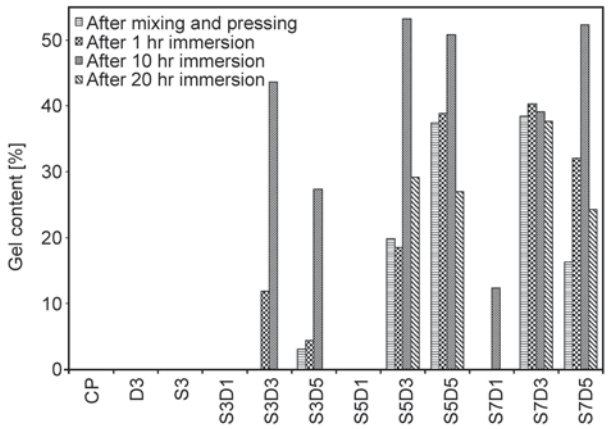

Figure 2. Gel content of samples at different curing condition, 1, 10 and 20 hr after immersion in hot water compared to the sample with no immersion in water

As indicated in Figure 2, the variation of gel content versus immersion time passes through a maximum at 10 hr. The gel content is balanced by crosslinking and hydrolytic degradation. Below 10 hr of immersion, the crosslinking is the predominant mechanism, while after that the chain scission in the presence of water becomes predominant. In other words, at long immersion times, the breakage of polymeric chains caused destruction of network into very small fragments which can exit from the finemesh stained steel in gel content experiments. Maximum gel fraction is found about 53% after 10 hr for S5D3 sample.

Another interesting point in Figure 2 is the existence of gel content in the samples S5D3, S5D5, S7D3, and S7D5 with high silane concentration without immersing in hot water. The high potential of crosslinking due to high degree of grafting in these samples lead to easy crosslinking with atmospheric humidity during mixing and pressing steps.

To get a better insight of silane crosslinking of PLA, the degree of swelling was also determined. It is well known that the degree of swelling is related to the crosslink density where a low degree of swelling indicates a high crosslink density of polymer [14]. The degree of swelling, $\bar{M}_c$ and crosslink density for three selected samples are presented in Table 2. As can be seen from the Table, sample S5D3 showed the lowest degree of swelling and higher crosslink density, because of higher silane content. The degree of swelling is commonly used to determine the average molecular weight between linkages. As expected, with a reduction in $\bar{M}_c$, crosslink density goes up. This trend as a function of the aforesaid parameters was found for the other samples too.

Table 2. Degree of swelling, $\bar{M}_c$ and crosslink density of selected samples immersed in hot water for 10 hr

	DS	$\bar{M}_c$ [g/mol]	υ [$\cdot 10^{-4}$ mol/L]
S3D3	40.17	1873.89	6.62
S3D5	42.80	1953.02	6.35
S5D3	27.11	1445.68	8.58

Figure 3. Dimension reversibility after 48 hr swelling in chloroform at room temperature, S3D3 (a), S3D5 (b), S5D3 (c). Original dimensions of all samples were similar before swelling.

The variation in crosslink density of the samples was also confirmed by visual inspection. Figure 3 illustrates the physical shape of the crosslinked samples after swelling in chloroform and further drying. Because of chemical network formation, after evaporation of solvent, sample should go back to the original dimension in case of defect-free network. The original dimension after drying of swollen samples was obtained for sample S5D3 which implies perfect network structure. In other samples, $\bar{M}_c$ is higher and longer distance between linkages is not able to return the polymeric chains in to their position before swelling. This phenomenon is schematically illustrated in Figure 3.

Schematic illustration of dimension reversibility is shown in Figure 4. As shown in Figure 4, having more silane grafted on polymer chains, makes the formed gel network tighter, in contrast to the low silane grafted PLA which had fewer linkages and consequently looser network. In addition, hydrolytic degradation leads to more defects in the network structure which caused the reduction of reversibility.

To monitor the hydrolytic degradation of the samples during crosslinking in hot water, molecular weight and molecular weight distribution of the samples were measured using GPC. GPC chromatograms of pure PLA, silane grafted samples, and sol fraction of crosslinked samples (at 10, 20 hr) are presented in Figures 5–7.

The GPC curves in Figure 5 shows a meaningful difference between pure PLA and grafted samples which means grafting reaction has changed the molecular structure of PLA. A shoulder appeared at high molecular weight position, which can be attributed to the formation of higher molecular weight chains due to grafting reaction. It is worth noting that the peak of shoulder displays approximately 4 times higher molecular weight in comparison to pure PLA. This shoulder in GPC curve can be considered to the formation of short and long branching structures [34].

As can be seen in Figure 6, a new shoulder appeared at low molecular weight position after 10 hr immersion in hot water. This shoulder can be an indication of the hydrolytic degradation during crosslinking. It can be noticed that the intensity of high molecular weight shoulder has been reduced compared to Figure 5. It is due to more contribution of these grafted chains in crosslinking reaction and formation of network. In other words, the grafted chains with higher molecular weight are involved in the crosslinking reaction and do not appear in the sol fraction.

By increasing the crosslinking time to 20 hr, the molecular weight shoulder completely disappeared and molecular weight distributions were shifted to lower molecular weights. It has been reported by Pistner *et al*. [35], at longer hydrolytic degradation time, bimodal and even multimodal curves are seen as result of selective degradation of the amorphous regions in GPC curve. In our study, only CP sample showed bimodal curves after 20 hr immersion in hot water, while the other samples showed monomodal peak until 20 hr. It seems that the hydrolytic

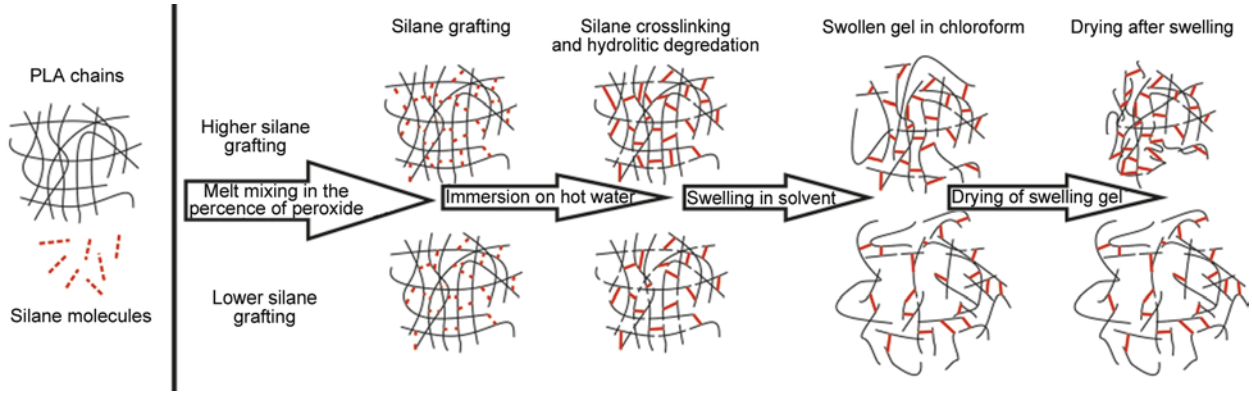

Figure 4. Schematic of dimensional reversibility of different gel network after swelling in solvent. Top way shows tight network with high dimensional reversibility and down way shows lose network that couldn't back to original dimension after swelling.

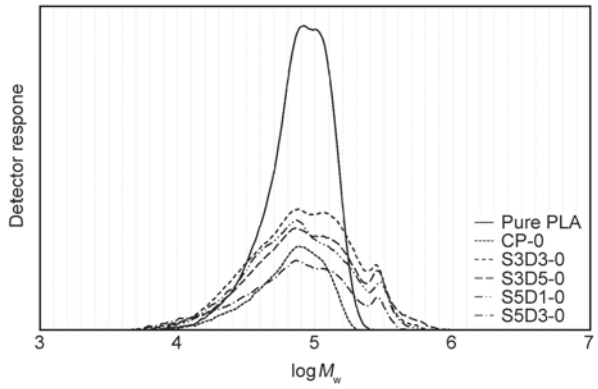

Figure 5. Molecular weight distribution of silane grafted PLAs compared with ungrafted samples (number after sample name shows time [hr] of immersing in hot water)

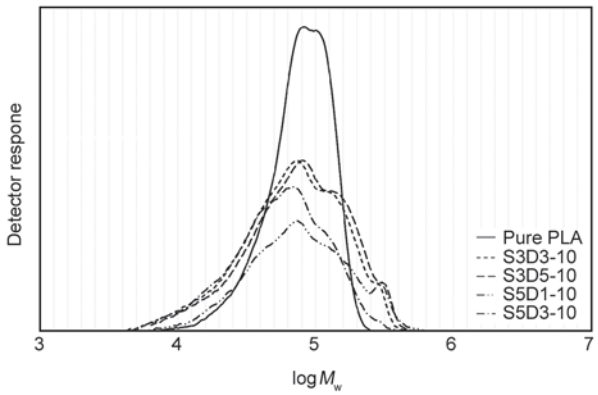

Figure 6. Molecular weight distribution of silane grafted PLAs after immersion in hot compared with ungrafted samples (number after sample name shows time [hr] of immersing in hot water)

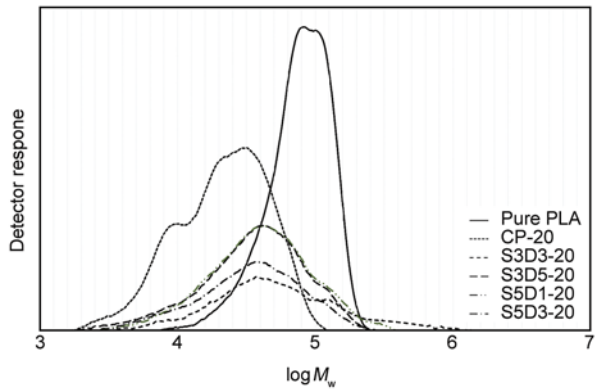

Figure 7. Molecular weight distribution of silane grafted PLAs after immersion in hot compared with ungrafted samples (number after sample name shows time [hr] of immersing in hot water)

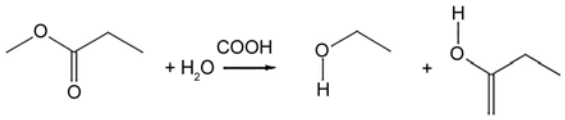

Figure 8. Mechanism of PLA ester bonds hydrolysis

degradation mechanism is affected by silane grafting, through changing molecular structure and crystalline domains.

The proposed mechanism of hydrolytic degradation of PLA is shown in Figure 8 which indicates the final product of hydrolyzation is lactic acid [3]. It is believed that the hydrolytic degradation of PLA chains favorably occurred in the amorphous regions. The result of chain scission is the formation of lactic acid oligomers which can be a catalyst for more hydrolytic degradation, because of the abundance of carboxylic acid end groups in the reaction media. It is known that PLA degradation is an auto-catalytic reaction [24].

In first step of degradation, assuming slight degree of chain scission, the hydrolysis rate of the ester linkages can be modeled by Equation (5):

$$\frac{1}{\bar{M}_{n_t}} = \frac{1}{\bar{M}_{n_0}} - k_1 t \tag{5}$$

where $\bar{M}_{n_t}$ is the molecular weight at time t, $\bar{M}_{n_0}$ is the M_n at $t = 0$ without chain scission, k_1 is the general hydrolytic degradation rate constant and t is the degradation time.

Taking into account the autocatalytic reaction, Equation (5) changes to Equation (6):

$$\ln \frac{\bar{M}_{n_t}}{\bar{M}_{n_0}} = -k_2 t \tag{6}$$

where k_2 is the rate constant of self-catalyzed hydrolytic degradation. In fact, the logarithmic format of molecular weight variation can cover the auto catalyst effect in the kinetic of reaction by more rapid reduction in molecular weight [36].

The variation of number average molecular weight versus time is demonstrated in Figure 9. These experimental data were fitted using Equations (5) and (6) (data are not shown here). High correlation coefficients were not obtained for these fittings. However, the correlation coefficient for Equation (6) was higher and more acceptable. The main reason for deviation from this model is simultaneously crosslinking reactions that led to consuming of high molecular grafted chains.

Temperature is a parameter affecting hydrolytic degradation. According to the literature, at higher temperature the degradation is accomplished with higher speed and usually is fitted better by autocatalytic model. At higher temperature, above T_g, movement of water molecules between polymer chains is

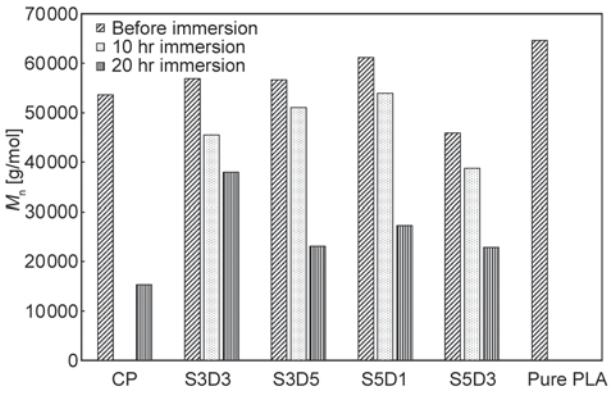

Figure 9. Number-average molecular weight of sol fraction for polymer samples. Samples without immersion in water and after 10 and 20 hr immersion in hot water during crosslinking are illustrated.

facilitated. In our case, crosslinking bonds limit this movement and prevents further degradation. The highest reduction of M_n in CP sample without crosslinking can be a witness for this phenomenon.

The presence of low molecular weight PLA as a production of hydrolytic degradation was checked by TGA test and the obtained results (TGA and DTG thermograms) are shown in Figure 10. Although there are no significant differences among the samples in TGA thermograms, a shoulder at lower temperature beside the main peaks are detectable in DTG curves. This shoulder in range of 300–350°C is related to the thermal degradation of lower molecular weight oligomers as products of hydrolytic degradation during crosslinking. As mentioned in other reports, the main thermal decomposition is occurred in the range of 300–390°C [37]. As can be seen in TGA of treated samples at lower temperature (magnified in Figure 10a), a bit weight loss occurred until 200°C related to lactic acid thermal degradation. This monomer is the main product of PLA chain scission.

According to Figure 10a (and internal table), the onset temperatures for degradation of treated PLA are clearly lower than that of the CP sample. In the untreated sample, 10 and 50% of decomposition occurred at about 328 and 353°C, respectively, and all treated samples showed lower thermal stability and degraded at lower temperatures. In the DTG curves, one can clearly observe the degradation reactions at lower temperatures, as suggested by the shoulder between 300 and 350°C. The place of shoulder is affected by the competition between crosslinking and hydrolytic degradation and DCP concentration. In other words, when the hydrolytic degradation is the dominant mechanism, the shoulder appeared at lower temperature. On the other hand, the higher concentration of DCP which have not reacted in silane grafting caused in chain scission of PLA, and subsequently to formation of higher concentration of low molecular weight chains.

The results (T_{onset}) in embedded table in Figure 10a imply a reduction in thermal stability of the crosslinked samples in comparison to CP sample which is not common. Han *et al.* [11] reported an increase of thermal stability for silane crosslinking of PLA. The main reason for the contradictory results is the difference in crosslinking temperature. Higher temperature of crosslinking in our study (70°C), compared to Han's work (40°C), caused more hydrolytic degradation than crosslinking.

4. Conclusions

This work is motivated by current researches in the development of PLA applications as a biodegradable polymer. Silane crosslinking was considered for the improvement of mechanical properties of PLA. Hydrolytic degradation is inevitable during

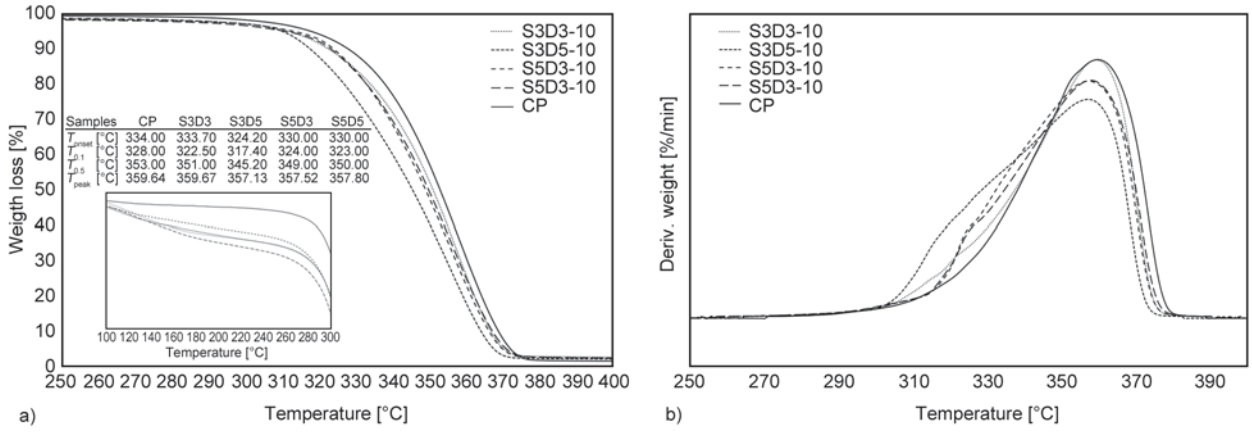

Figure 10. a) TGA and b) DTG diagrams for different PLA samples

crosslinking by immersion in hot water and appears as a competitive reaction in this method. Two reactions were tracked and the following results can be drawn from this study:

- Hydrolytic degradation was monitored using GPC, TGA, gel content and swelling tests and its negative effect on the crosslinking reaction and obtained gel structure was tracked.
- Silane grafting of PLA was directly affected by silane and peroxide concentrations. Lower concentrations of DCP lead to insufficient radical formation on PLA chains, and consequently low degree of grafting on PLA. On the other hand, samples containing higher DCP content in presence of VTMO silane lead to premature gel formation during grafting reaction.
- Both tight and loose gel structures were found using swelling. The formation of loose gel structure (as a defect) may be attributed to high hydrolytic degradation.
- An extra peak was observed in GPC curve for the grafted samples which implies the formation of higher molecular weight chains due to the grafting reaction. This peak diminished at longer time of immersion in hot water as a result of consumption of grafted PLA molecules in crosslinking reaction.
- Hydrolytic degradation process was intensified at longer crosslinking time and its trace was observed by a peak at lower molecular weights in GPC chromatograms. The low molecular weight oligomers after hydrolytic degradation was also observed in DTG as a shoulder in lower temperature.
- The observations were confirmed with TGA test. The low molecular weight oligomers after hydrolytic degradation observed in DTG as shoulder in lower temperature.

References

[1] Cairncross R. A., Becker J. G., Ramaswamy S., O'Connor R.: Moisture sorption, transport, and hydrolytic degradation in polylactide. Applied Biochemistry and Biotechnology, **131**, 774–785 (2006).
DOI: 10.1385/ABAB:131:1:774

[2] Liu M., Yin Y., Fan Z., Zheng X., Shen S., Deng P., Zheng C., Teng H., Zhang W.: The effects of gamma-irradiation on the structure, thermal resistance and mechanical properties of the PLA/EVOH blends. Nuclear Instruments and Methods in Physics Research Section B: Beam Interactions with Materials and Atoms, **274**, 139–144 (2012).
DOI: 10.1016/j.nimb.2011.12.020

[3] Nampoothiri K. M., Nair N. R., John R. P.: An overview of the recent developments in polylactide (PLA) research. Bioresource Technology, **101**, 8493–8501 (2010).
DOI: 10.1016/j.biortech.2010.05.092

[4] Xiao L., Wang B., Yang G., Gauthier M.: Poly(lactic acid)-based biomaterials: Synthesis, modification and applications. in 'Biomedical science, engineering and technology' (ed.: Ghista D. N.) InTech, Rijeka, 247–282 (2012).
DOI: 10.5772/23927

[5] Wang Y., Chiao S. M., Hung T-F., Yang S-Y.: Improvement in toughness and heat resistance of poly(lactic acid)/polycarbonate blend through twin-screw blending: Influence of compatibilizer type. Journal of Applied Polymer Science, **125**, E402–E412 (2012).
DOI: 10.1002/app.36920

[6] Nagasawa N., Kaneda A., Kanazawa S., Yagi T., Mitomo H., Yoshii F., Tamada M.: Application of poly (lactic acid) modified by radiation crosslinking. Nuclear Instruments and Methods in Physics Research Section B: Beam Interactions with Materials and Atoms, **236**, 611–616 (2005).
DOI: 10.1016/j.nimb.2005.04.052

[7] He C., Feng W., Cao L., Fan L.: Crosslinking of poly(L-lactide) nanofibers with triallyl isocyanutrate by gamma-irradiation for tissue engineering application. Journal of Biomedical Materials Research Part A, **99**, 655–665 (2011).
DOI: 10.1002/jbm.a.33235

[8] Jin F., Hyon S-H., Iwata H., Tsutsumi S.: Crosslinking of poly(L-lactide) by γ-irradiation. Macromolecular Rapid Communications, **23**, 909–912 (2002).
DOI: 10.1002/1521-3927(20021001)23:15<909::AID-MARC909>3.0.CO;2-8

[9] Malinowski R., Rytlewski P., Żenkiewicz M.: Effects of electron radiation on properties of PLA. Archives of Materials Science and Engineering, **49**, 25–39 (2011).

[10] Mitomo H., Kaneda A., Quynh T. M., Nagasawa N., Yoshii F.: Improvement of heat stability of poly(L-lactic acid) by radiation-induced crosslinking. Polymer, **46**, 4695–4703 (2005).
DOI: 10.1016/j.polymer.2005.03.088

[11] Han C., Bian J., Liu H., Han L., Wang S., Dong L., Chen S.: An investigation of the effect of silane water-crosslinking on the properties of poly(L-lactide). Polymer International, **59**, 695–703 (2010).
DOI: 10.1002/pi.2760

[12] Takamura M., Nakamura T., Kawaguchi S., Takahashi T., Koyama K.: Molecular characterization and crystallization behavior of peroxide-induced slightly crosslinked poly(L-lactide) during extrusion. Polymer Journal, **42**, 600–608 (2010).
DOI: 10.1038/pj.2010.42

[13] Takamura M., Nakamura T., Takahashi T., Koyama K.: Effect of type of peroxide on cross-linking of poly(L-lactide). Polymer Degradation and Stability, **93**, 1909–1916 (2008).
DOI: 10.1016/j.polymdegradstab.2008.07.001

[14] Yang S-L., Wu Z-H., Yang W., Yang M-B.: Thermal and mechanical properties of chemical crosslinked polylactide (PLA). Polymer Testing, **27**, 957–963 (2008).
DOI: 10.1016/j.polymertesting.2008.08.009

[15] Shayan M., Azizi H., Ghasemi I., Karrabi M.: Effect of modified starch and nanoclay particles on biodegradability and mechanical properties of cross-linked poly lactic acid. Carbohydrate Polymers, **124**, 237–244 (2015).
DOI: 10.1016/j.carbpol.2015.02.001

[16] Morshedian J., Hoseinpour P. M.: Polyethylene crosslinking by two-step silane method: A review. Iranian Polymer Journal, **18**, 103–128 (2009).

[17] Azizi H., Morshedian J., Barikani M.: Silane grafting and moisture crosslinking of polyethylene: The effect of molecular structure. Journal of Vinyl and Additive Technology, **15**, 184–190 (2009).
DOI: 10.1002/vnl.20194

[18] Barzin J., Azizi H., Morshedian J.: Preparation of silane-grafted and moisture cross-linked low density polyethylene: Part I: Factors affecting performance of grafting and cross-linking. Polymer-Plastics Technology and Engineering, **45**, 979–983 (2006).
DOI: 10.1080/03602550600718209

[19] Barzin J., Azizi H., Morshedian J.: Preparation of silane-grafted and moisture crosslinked low density polyethylene. Part II: Electrical, thermal and mechanical properties. Polymer-Plastics Technology and Engineering, **46**, 305–310 (2007).
DOI: 10.1080/03602550601155815

[20] Żenkiewicz M., Malinowski R., Rytlewski P., Richert A., Sikorska W., Krasowska K.: Some composting and biodegradation effects of physically or chemically crosslinked poly(lactic acid). Polymer Testing, **31**, 83–92 (2011).
DOI: 10.1016/j.polymertesting.2011.09.012

[21] Hakkarainen M.: Aliphatic polyesters: Abiotic and biotic degradation and degradation products. Degradable aliphatic polyesters, **157**, 113–138 (2002).
DOI: 10.1007/3-540-45734-8_4

[22] Hurrell S., Cameron R. E.: The effect of initial polymer morphology on the degradation and drug release from polyglycolide. Biomaterials, **23**, 2401–2409 (2002).
DOI: 10.1016/S0142-9612(01)00376-3

[23] Grizzi I., Garreau H., Li S., Vert M.: Hydrolytic degradation of devices based on poly(DL-lactic acid) size-dependence. Biomaterials, **16**, 305–311 (1995).
DOI: 10.1016/0142-9612(95)93258-F

[24] Hyon S. H., Jamshidi K., Ikada Y.: Effects of residual monomer on the degradation of DL-lactide polymer. Polymer International, **46**, 196–202 (1998).
DOI: 10.1002/(SICI)1097-0126(199807)46:3<196::AID-PI914>3.0.CO;2-Y

[25] Tsuji H., Miyauchi S.: Poly(L-lactide): VI Effects of crystallinity on enzymatic hydrolysis of poly(L-lactide) without free amorphous region. Polymer Degradation and Stability, **71**, 415–424 (2001).
DOI: 10.1016/S0141-3910(00)00191-9

[26] Zhou Q., Xanthos M.: Nanoclay and crystallinity effects on the hydrolytic degradation of polylactides. Polymer Degradation and Stability, **93**, 1450–1459 (2008).
DOI: 10.1016/j.polymdegradstab.2008.05.014

[27] Weir N. A., Buchanan F. J., Orr J. F., Farrar D. F., Dickson G. R.: Degradation of poly-L-lactide. Part 2: Increased temperature accelerated degradation. Journal of Engineering in Medicine, **218**, 321–330 (2004).
DOI: 10.1243/0954411041932809

[28] Paul M-A., Delcourt C., Alexandre M., Degée P., Monteverde F., Dubois P.: Polylactide/montmorillonite nanocomposites: Study of the hydrolytic degradation. Polymer Degradation and Stability, **87**, 535–542 (2005).
DOI: 10.1016/j.polymdegradstab.2004.10.011

[29] Mitomo H., Kaneda A., Quynh T.M., Nagasawa N., Yoshii F.: Improvement of heat stability of poly (L-lactic acid) by radiation-induced crosslinking. Polymer, **46**, 4695–4703 (2005).
DOI: 10.1016/j.polymer.2005.03.088

[30] Södergård A., Selin J. F., Näsman J. H.: Hydrolytic degradation of peroxide modified poly(L-lactide). Polymer Degradation and Stability, **51**, 351–359 (1996).
DOI: 10.1016/0141-3910(95)00271-5

[31] Sperling L. H.: Introduction to physical polymer science. Wiley, Hoboken (2005).

[32] Liu N. C., Yao G. P., Huang H.: Influences of grafting formulations and processing conditions on properties of silane grafted moisture crosslinked polypropylenes. Polymer, **41**, 4537–4542 (2000).
DOI: 10.1016/S0032-3861(99)00654-0

[33] Nijenhuis A. J., Grijpma D. W., Pennings A. J.: Crosslinked poly(L-lactide) and poly(ε-caprolactone). Polymer, **37**, 2783–2791 (1996).
DOI: 10.1016/0032-3861(96)87642-7

[34] Liu J., Lou L., Yu W., Liao R., Li R., Zhou C.: Long chain branching polylactide: Structures and properties. Polymer, **51**, 5186–5197 (2010).
DOI: 10.1016/j.polymer.2010.09.002

[35] Pistner H., Bendix D. R., Mühling J., Reuther J. F.: Poly(L-lactide): A long-term degradation study *in vivo*: Part III. Analytical characterization. Biomaterials, **14**, 291–298 (1993).
DOI: 10.1016/0142-9612(93)90121-H

[36] Pitt C. G., Zhong-wei G.: Modification of the rates of chain cleavage of poly(ε-caprolactone) and related polyesters in the solid state. Journal of Controlled Release, **4**, 283–292 (1987).
DOI: 10.1016/0168-3659(87)90020-4

[37] Feng L., Li G., Bian X., Chen Z., Liu Y., Cui Y., Chen X.: Rapid determination of residual monomer in polylactide using thermogravimetric analysis. Polymer Testing, **31**, 660–662 (2012).
DOI: 10.1016/j.polymertesting.2012.03.010